Population Balance Modelling of Soot Formation in Laminar Flames

Anxiong Liu

Department of Mechanical Engineering
Imperial College London

This dissertation is submitted for the degree of
Doctor of Philosophy

January 2020

Declaration of Originality

I hereby declare that except where appropriate reference is made to the work of others, the contents of this dissertation are original and have not been submitted in whole or in part for consideration for any other degree or qualification in this, or any other university. This dissertation is my own work, produced under the supervision of Dr. Rigopoulos and contains nothing which is the outcome of work done in collaboration with others, except as specified in the text and Acknowledgements. This dissertation contains around 45,000 words including appendices, bibliography, footnotes, tables and equations and has 53 figures.

Copyright Declaration

Acknowledgements

I have the privilege of having Dr. Stelios Rigopoulos as my supervisor for all the dedication, guidance, encouragement, advice he has generously given me throughout the arduous but rewarding PhD journey. Dr. Rigopoulos is endowed with rigorous working attitude, prospective views and excellent English writing, which benefits me enormously in my research experience.

I would also like to express my gratitude to Dr. Fabian Sewerin, who has graduated from our group, for his generous help on learning our in-house code and novel numerical methods. His strict and precise attitude is exemplary for me.

Further, I am obliged to thank Dr. Carlos E. Garcia Gonzalez from Imperial College London, Dr. Zhan Gao from Shanghai JiaoTong University, Dr. Bo Tian from University of Cambridge for their endeavours on our collaborative projects of Santoro flames and the combustion with biodiesel fuels. Dozens of discussions and conversations with them impart me new insights on the research.

I cherish every communication with my group members, whether it is a nugget of truth, a piece of encouragement or even a word of humor. And grateful to my family, for being unconditionally support and tolerance.

I gratefully acknowledges financial support of the Chinese Scholarship Council (CSC).

Abstract

In this thesis, a discretised population balance eqaution (PBE) with a comprehensive model of soot formation processes has been coupled with the computational fluid dynamics (CFD) to predict the soot evolution in laminar diffusion flames. Contributions have been made in terms of methodology, modelling and applications.

First of all, a conservative finite volume method is proposed to discretise the PBE with regard to the coagulation process. This method rigorously calculates the double integrals arising from the coagulation terms via a geometric representation, and exactly balances the coagulation source and sink terms to conserve moments. It proves that the proposed method is able to accurately predict the distribution with a small number of sections and conserve the first moment (or any other single moment) in the coagulation process, in an extensive test of various coagulation kernels, initial distributions and 'self-preserving' distributions, by comparison with analytical solutions and direct numerical solutions of the discrete PBE. Moreoever, the method is also flexible to an arbitrary non-uniform grid.

Later on, the proposed method is also coupled with the CFD program to simulate Santoro flame, a laminar ethylene diffusion flame, for the validation on its accuracy, economy and robustness. Furthermore, the simulation results have been compared with simultaneous multiple diagnostics measurements drawn from a single data source, providing guidance on soot kinetic models. Three well-established PAH-based chemical reaction mechanisms, ABF, BBP and KM2, are employed to model the inception of soot precursors and oxidants. The physical model involves the nucleation by PAH dimerisation, surface growth by HACA mechanism and PAH condensation, size-dependent coagulation. Experimental signals are directly modelled, including the line-of-sight attenuation (LOSA) for the integrated soot volume fraction, planar OH laser-induced fluorescence (OH-PLIF) and elastic light scattering (ELS) for the soot distribution. The comparisons between model predictions and experimental measurements reflect the predictive capability for soot formation in laminar diffusion flame in terms of the flame structure, soot appearance and amount of soot production. The background gas phase chemistry clearly affects the soot

modelling and a sensitivity analysis suggests that coordinating the rates of nucleation and surface growth help adjust the soot production on the centreline and sooty wings.

Finally, the same soot model has been extended to two studies of diffusion flames with blends oxygen-containing surrogates: (1) methyl decanoate (MD) with the addition of dibutyl ether (DBE); (2) four practical methyl ester-based real biodiesels and their blends with petroleum diesel. In the first case study, aiming to reproduce an experiment which was to investigate the effects of dibutyl ether (DBE) addition to the biodiesel surrogate (methyl decanoate, MD), a combined and reduced MD-DBE-PAH mechanism from three sub-mechanism sources has been employed in the simulation. Due to the heavy molecular weight of the biodiesel fuel, the terms of the effect of molecular weight, thermophoresis and Dufour effect in the energy equation exhibit a similar magnitude with the original diffusion term, especially in the region of high temperature and a large gradient of the average molecular weight. Predicted temperature profiles are in good comparison with the experiment in terms of position and absolute value. The swallow-tail shape of the soot region and the absolute soot production are correctly predicted by the simulation. In terms of soot suppression, the model predicts 33% reduction of soot as the DBE addition ranges from 0% to 40%, in contrast to around 55% reduction measured in the experiment. In the second study, a semi-detailed kinetic mechanism for the pyrolysis and combustion of a large variety of biodiesels fuels are considered. The model successfully captures the reduction of soot formation by addition of biodiesels, but not necessarily the rate of decrease with blending. The current investigation offers pioneer and encouraging results on modelling soot formation in biodiesel flames, which has been fewly explored.

Table of contents

List of figures

List of tables

Nomenclature

Latin letters

$\bar{W}$, W_k the average molecular weight, the molecular weight of species k

ΔM the change of moment in the coagulation process

$\dot{Q}$ external heat source

$\dot{q}_j$ the energy flux

$\dot{R}_{\mathrm{g}}$ the reaction rate for nucleation

$\dot{R}_{\mathrm{n}}$ the reaction rate for growth

x the spatial vector

Y the array of the concentrations of species

U complementary volume

A the integral area inside an interval in the coagulation process

A_{s} the surface area density of particles

C_{m}, C_{t}, C_{s} Model parameters for the thermophoretic velocity of soot particles

C_{r} the correction constant in the nucleation rate and condensation rate

C_{v} the molar heat capacity at constant volume

C_{ov} overlapping parameter for neighbouring primary particles

$C_{\mathrm{p},k}$ the molar heat capacity of species k at constant pressure

d_{g}, d_{h} diameter of gyration, hydrodynamic diameter of a fractal aggregate

d_{p} diameter of a spherical particle

D_p the diffusion coefficient of a particle

D_{f} fractal dimension

$d_{\mathrm{p,a}}$ the average diameter of primary particles

$d_{k,j}$ the j-component of drift vector for species k in the mixture

$D_{k\mathrm{m}}$, D_k^{T} the diffusion coefficients for species k due to the gradients of species concentration and temperature in the mixture

F_v volume force

f_v soot volume fraction

G a group of intervals

G the growth rate in the PBE

h, h_k, h_k^0 total enthalpy, specific enthalpy of species k, enthalpy of formation of species k

I an integral denoting the source or sink inside an interval

k_{B} Boltzmann constant

k_{g} the Arrhenius type expression for growth

k_{n} the Arrhenius type expression for nucleation

K_j j-component diffusive flux of number density

M_k the k^{th}moment

n the Number density

N_{p} the number of primary particles

N_A Avogadro's number

N_i the number density of soot particles in a particular size range i

P pressure

$S(q)$ the structure factor

$S^{\mathrm{OH-LIF}}$ the LIF signal

S_k the source term in the k^{th}transportequation

S_{ELS} the ELS signal

S_{ij} the tensor of strain rate

t time

$u(v_i)$ the index of the cell upstream of node v_i

U_i the velocity component in i direction

$uu(v_i)$ the index of the cell upstream of node with the index $u(v_i)$

v_0 the volume of a nucleus

$v_{\mathrm{p,a}}$ the average volume of primary particles

$V_{k,j}$ the j-component of the diffusion velocity of species k

w,v,u the volume of a particle

x_i the spatial position in i direction

X_k mole fraction of the k^{th}species

Y_k mass fraction of the k^{th}species

UD unsaturation degree

Greek letters

β the coagulation rate

χ_s the number density of surface sites

$\dot{\omega}_k$ the reaction rate of species k

$\dot{\omega}_{\mathrm{T}}$ heat source from chemical reactions

ϵ the Lennard-Jones potential well depth

γ the collision efficiency in the process of nucleation and condensation of PAH molecules

λ the heat conductivity

μ dynamic viscosity

Ω collision integral

ω_i the weight of the point i in the quadrature rule

Φ the semi-empirical formula proposed for the mixture-averaged viscosity

ϕ_k the scalar in the k^{th}transportequation

$\psi(v_i)$ the flux limiter at the cell face v_i

ρ density (gas phase)

ρ_s the density of soot

σ the Lennard-Jones potential

σ_{s} the scattering cross-section

Θ_k thermal diffusion ratio of species k in the mixture

θ_k binary thermal diffusion ratio

$\xi_a, \xi_b, \xi_c, \xi_d$ parameters in a semi-empirical soot model

ζ_{ij} the tensor of stress

Superscript letters

$*$ reduced values

$^{\text{left}}, ^{\text{middle}}, ^{\text{right}}$ the position of integral shapes

$^{\text{rec}}, ^{\text{rt}}, ^{\text{olt}}, ^{\text{nlt}}$ geometric shapes in the discretisation of the coagulation process

Subscript letters

$_{\text{b}}$ coagulation source

$_{\text{d}}, _{\text{dj}}, _{\text{dk}}$ coagulation sink

$_{i, j, k}$ the index of a species, a component of a spatial vector, the index of an interval

$_{\text{sink}}$ coagulation sink

$_{\text{source}}$ coagulation source

Chapter 1

Introduction

1.1 Background and Motivation

In 2018, hydrocarbon fuels (including fossil fuels and renewable biomass) account for about 81.8% , 76.2%, 85.5% of consumption by all means of primary energy in the UK, in the EU and worldwide, respectively [1]. Herein, a vast majority of the energy in the hydrocarbon fuels is released via thermal energy in the process of combustion. Turbulent combustion is mostly used for industrial applications including internal combustion engines for vehicles and ships, and gas turbines in aeroplanes and power plants.

Emissions of carbon and pollutants are the major problems that combustion is being criticised nowadays. In the last two centuries, significant consumption of fossil fuels deposited for billions of years has released millions of tons of carbon dioxide during the course of industrialisation and urbanisation, resulting in the issue of global warming and climate change, yet controversial. However, combustion is the most developed and in the foreseeable future, will still the most frequently applied process because of its economy (in terms of the fuels and the combustion reactors), stability (.vs. solar energy, wind and geothermal energy) and safety (.vs. nuclear energy). The primary energy structure based on fossil fuels, determining the energy supply means of the combustion process, seems unshakable, if scientists fail to achieve breakthroughs in all procedures of absorbing, storing, transferring and utilising other energy sources. Nowadays, renewable biomass fuels, mainly plant-derived, have been supplemented and marked as net zero or even negative carbon emissions for the combustion process.

On the other hand, emissions of particles and toxic gases including nitrogen and sulfur oxides leads to environmental and health issues. In order to adapt increasingly

stringent emission regulations, purification of fuels and control technique for combustion have been introduced. For example, desulphurisation, deleading of fuels, and the use of catalytic converters after combustion reactors extremely reduce the emissions of toxic gases or matters. Applications of the lean-burning principle, like the Gasoline Direct Inject (GDI) and Homogeneous Charge Compression Injection (HCCI) provide low exhaust hydrocarbon emissions and efficient fuel use. DEFRA (Department for Environment Food & Rural Affairs) reported that from 1970 to 2017 in the UK, the emissions of Sulphur dioxide, Nitrogen dioxide, PM_{10} (the size of particles of 10 μm or less), $PM_{2.5}$ (the size of particles of 2.5 μm or less) have been significantly reduced by 98%, 73%, 75% and 78% [2], respectively, which illustrates that combustion can be a clean solution obeying the environmental-driven requests as it still dominates the energy supply.

This thesis is concentrated on the aspect of soot. Soot is the product of incomplete combustion of hydrocarbon fuels and calls for substantial attention. It is primarily concerned that the soot emission is detrimental to human health and atmospheric visibility. Particulate matters are responsible for aggravating several conditions including respiratory diseases, heart diseases, stoke and lung cancer [3]. In terms of engineering industries, carbon deposition inside the combustors and the accosciative components, including pistons of internal combustion engines and turbine blades of gas turbines, affects the mechanical and thermal efficiency or even operational safety of the machines. Admittedly, soot has some practical benefits, for example, assisting the heat convection in the coal furnaces and facilitating radiative heat transfer as a coating surface in solar cookers [4].

Access to the particle size distribution (PSD) of soot is very important with regard to environmental, health and engineering aspects. Particles classified according to their size have been recongnised among the public. Figure 1.1 summarises impacts of particles of different size on human's respiratory system, wherein PM_{10} and $PM_{2.5}$ are the most hazardous sizes because they can get deep into lungs and some may even penetrate into bloodstreams. In views of environmental effects, fine particles ($PM_{2.5}$) are the main cause of reduced visibility (haze) in cities and wilderness areas. On the engineering aspect, for instance, in the diesel engine, soot depositions will increase the frictional loss and affect its operating performance. Particles of a particular size range may extremely destroy some exactitude parts with precise dimension or in perfectly coordination with other components.

The aim of this thesis is to offer a thorough computational modelling method of soot formation and comparison with experimental measurements in co-flow diffu-

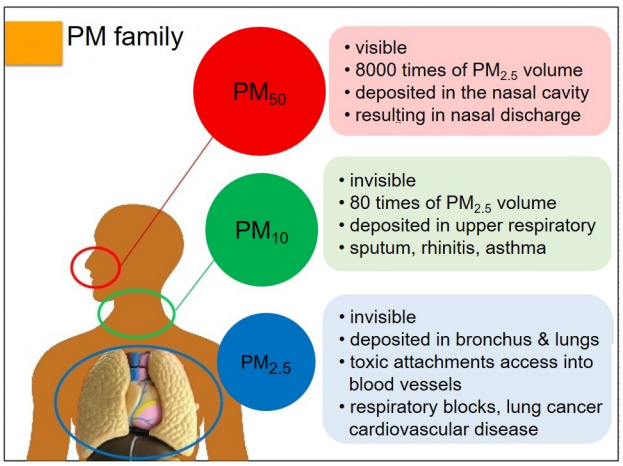

Fig. 1.1 Impacts of particle of different sizes on human respiratory system

sion flames with the fuel ethylene and biomass surrogates. The laminar diffusion flame is a simple combustion phenomenon including complete aerodynamic processes, which is well characterised and relevant to particle applications, like the combustion in diesel engines and gas turbines. The feasible numerical approach, on a fundamental level, helps understand the evolution mechanism of soot formation and predict the particle size distribution (PSD), which, on a practical level, can be used to improve the predictive capability of modelling of soot formation in practical engines and thereby enhance the pollutant reduction strategies, thus the performance of combustion devices.

1.2 Limitations of previous research

The previous investigations on soot formation have achieved significant success in the aspects of methodology, modelling and applications. However, several limitations. First of all, the research community working on soot formation has employed the methods developed by people studying aerosol dynamics [5, 6]. So far, methods of moments (in Section 2.2.1) are mainly utilised for soot formation modelling [7–9], but the methods of discretised PBE and the stochastic process are still rarely applied. Another situation is that researchers fully trust the accuracy of the methods for population balance and concentrate on modelling soot formation and coupling the soot phase with fluid dynamics. As a result, the errors from the numerical methods are rarely discussed. For example, some discretised PBE methods fail to conserve the invariant property, like the total volume in the process of coagulation or to be utilised with any non-uniform grid or adaptive grid. Consequently, the gap between the

simulations and the reality cannot be specified in the respect of numerical methods or modelling.

Second, the investigators have basically followed the physics of soot formation currently understood and modelled as similar processes of nucleation, surface growth and coagulation. Yet, all manners of empirical parameters have been given according to the corresponding gas-phase chemical kinetics, fuels and flame types. As a result, people are devoted to establishing sophisticated soot models but choose not to evaluate the consistency or generalisation of these models.

Third, the simulation of soot formation in combustion and flames with fuels of heavy molecules are rarely investigated because of the computationally unaffordable chemical kinetics and much bigger uncertainties in the chemical components, chemical kinetics and thermophysical properties than with simple-molecule fuels, like ethylene or propane, which intensifies the difficulty for the consistency of soot models. In recent years, biodiesel is regarded as one of the potential alternative fuels, not only to alleviate the energy shortage, but also to control pollutant emissions in an extensive number of applications. In contrast, the numerical studies of soot formation in the combustion and flames with biodiesel fuels lag far behind the measurements.

1.3 Contributions of the thesis

The contributions of this research are summarised as the following:

(1) In order to accurately predict the distribution with a small number of sections as well as conserve the first moment (or any other moment), a novel discretisation method for the coagulation process in the population balance equation is presented, along with the processes of nucleation and growth. Rather than using approximation by the methods of quadrature or interpolation, the double integrals arising from the discretisation of the coagulation terms are rigorously presented by geometric shapes, and the exact balance of coagulation source and sink terms are evaluated to conserve the moment. This proposed method can be flexibly applied to an arbitrary non-uniform grid and also be combined with a CFD code for solving the sooting formation in combustion issues with affordable speed and high robustness.

(2) The discretised population balance equation has been coupled with CFD code, in order to simulate the ethylene laminar diffusion flames, which are endowed with full aerodynamic processes and chemical reactions. One objective here is to explore the evolution of soot formation in the laminar diffusion flame, by combining

a joint experimental and modelling investigation and to offer guidance on the modelling of soot kinetics. The other object is to analyse the effect of different sources of background chemical kinetics on soot modelling and determine the empirical parameters for soot processes via a sensitivity analysis.

(3) Besides the combustion issues with small-molecule fuels, the PBE-CFD method is also advocated to the flames with heavy-molecule fuels: the biodiesel surrogates which suppress soot formation. This is the first trial that soot formation modelling is applied to flames with blends of different oxygen-containing biodiesel fuels, with the long-standing challenges of the complexity of chemical reactions and soot formation pathways in biodiesel fuels. The same set of empirical parameters in the soot modelling for the ethylene Santoro flame will still remain to validate its general applicability.

1.4 Organisation of the thesis

This thesis is outlined as follows:

Chapter 2 enumerates the literature reviews on the current understanding of the physics of soot formation, advanced measurement/diagnostic techniques, and the cutting-edge numerical methods for population balance modelling of aerosol dynamics. The classical models of soot kinetics are reviewed in the end. The equations of fluid dynamics and numerical frameworks are listed for reference.

Chapter 3 focuses on the development of a novel discretisation method for double integrals of the coagulation process in the PBE based on finite volume scheme or sectional method in the mathematical approach. The proposed method proves to predict the accurate distribution and to conserve the first-order moment (volume) or any other single moment, by a number of numerical tests on the cases of pure coagulation, coagulation growth and 'self-preserving' distributions. Comparisons with analytical solutions, numerical standard references and using other commonly-used numerical methods are also provided.

Chapter 4 presents the population balance modelling, coupled with our in-house CFD code to simulate the ethylene laminar diffusion flames with the Santoro burner of applying importance. The first part assesses the accuracy, economy and robustness of the proposed method in a real combustion (inhomogeneous reacting flow) issue. The second part explores the soot evolution mechanisms in the ethylene diffusion flames by a joint numerical and laser diagnostic investigation. The models of soot

processes and kinetics are elaborated in details. Different sets of chemical kinetics are compared to explore their effect on the soot models.

Chapter 5 extends the same method and soot model on the laminar diffusion flames with blends of oxygen-containing surrogates. Special treatments are also investigated, including combining/reducing several sources of chemical kinetics and completing the simplified transport equations of scalars and energy with additional diffusion terms which account for importance in the combustion with heavy-molecule fuels.

Chapter 6 summarises the conclusions of the thesis and suggests potential areas for future research.

The developments in Chapter 3 have been reported in my publication [10]. The main contents (text, figures, tables) are reproduced here with minor modifications and amendments.

As part of my research efforts, Chapter 4 is originated from a collaboration with Dr. Carlos Garcia Gonzalez, Dr. Fabian Sewerin and Dr. Ben Williams. The contents have been submitted as a journal paper to Combustion and Flame for revision. Chapter 5 are two colllaborative studies with Dr. Zhan Gao et al. and Dr. Bo Tian, et al, respectively, which have both been submitted as journal papers to Proceedings of the Combustion Institute for revision.

Chapter 2

Literature Review and Background Theory

In this research, the discretised population balance equation (PBE) has been coupled with the Computation Fluid Dynamic (CFD) program to predict soot formation in laminar diffusion flames. The methodology and theoretical foundations are described in this chapter. Prior to this, the preceding research on the physics of soot formation, experiment and numerical techniques to investigate and simulate soot formation will be reviewed.

2.1 Mechanisms and modelling of soot formation

2.1.1 Current understanding of soot formation

In the general view of particle formation, several processes are involved from the gas phase. First, the particulate nuclei are produced from a condensable species in the gas phase under saturation conditions [11]. Afterwards, these nuclei may undergo growth in the equilibrium condition that the mass addition onto the nuclei is stronger than the evaporation or reactions back to the gas phase. The surface growth of gaining mass is either by surface growth, a molecule joining with the nucleus via chemical reactions, or in the form of coagulation, when two particles stick together and form a large-size particle or a fractal-like structure that resemble a bunch of grapes [12]. People also use 'aggregation' when the original particles are still distinguishable in fractal aggregates. It is noted that the coagulation or aggregation process reduces the number of particle while surface growth has no

impact. The particles may also shrink or collapse via different processes of surface evaporation or reactions, particle breakage or fragmentation [13].

Another term 'agglomerate' is also widely used by nanoparticle technologists to describe assembles of particles. Unfortunately, in the review paper by Nichols et al. [14] , 'aggregate' and 'agglomerate' were frequently interchanged due to conflicting definitions in national and international standard, resulteing in universal confusion on the communication in research papers. According to the definitions of a majority of articles [15–18], an aggregate is an assemble of particles that are loosely attached with others by physical contact at their corners and edges. In contrast, an agglomerate is an assemble of particles that are firmly attached at their faces with chemical binds by processes of fusion, sintering or growth. In this thesis, only the term 'aggregate' is used to describe the fractal-like assembles of particles.

Soot formation in combustion field is basically following the evolution process described above. However, it is more complex than the phenomena of other polydispersed particles. First of all, combustion poses a challenge due to the heterogeneity of high temperature, mass diffusion and turbulence in the field. Moreover, hundreds or even thousands of chemical reactions occur due to the pyrolysis and oxidation of fuels, leading to a range of hydrocarbon precursors, usually polycyclic aromatic hydrocarbon PAHs during the process of nucleation and surface addition on the particles.

Second, particle inception or nucleation involves different gas-phase species. The small-size gas-phase PAHs (like naphthalene $C_{10}H_8$, phenathrene $C_{14}H_{10}$, pyrene $C_{16}H_{10}$) then undergo linear-lumping growth [7] in order to form larger-size PAHs. The molecules acetylene C_2H_2 contributes the most to PAHs' growth [7, 19, 20]. The C_2H_2 are added to the activated sites on the substrate PAHs which have been activated by gaseous hydrogen atoms. This process is summarised as the hydrogen-abstraction-carbon-addition (HACA) mechanism. According to the types of active sites, C_2H_2 can be added to an free-edge, armchair, zigzag, bay or five-member ring of a PAH molecule, as Fig. 2.1 shows. Furthermore, phenyl (C_6H_7) addition cyclisation [21] and methyl (CH_3) [22] addition have also been reported for the PAHs' growth.

In the next step, how the gas-phase PAHs transform to the soot nuclei? Wang [24] proposed three conceptual pathways. As seen in Fig. 2.2, path A is that the flat 2D PAHs grow and curl into fullerene-like structures; path B is the physical coalescence of moderate-size PAHs and path C is a chemical evolution into cross-linked 3D structures. These pathways finally lead to very small spherical particles

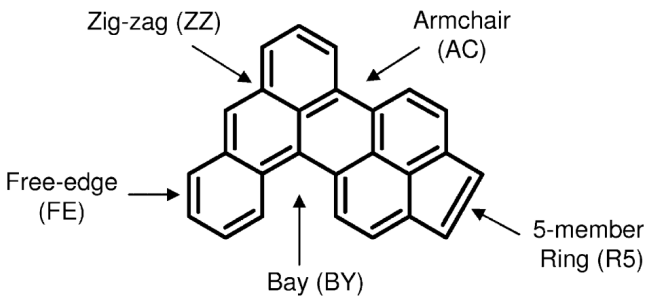

Fig. 2.1 Five principal types of active sites where the acetylene molecules are able to add in an example PAH molecule. The illustration is adapted from [23]

with diameters up to 2 -5 nm [25], observed in many TEM (transmission electron microscopy) measurements [26, 27].

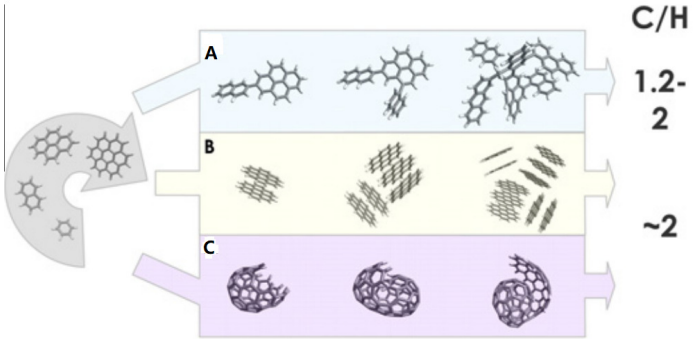

Fig. 2.2 Conceptual pathways for soot nucleation. The illustration is adapted from [24]

Another explanation on the soot nuclei is the surface shell formation (SSF) model by Kholghy et al. [28], which starts with pure PAHs and ends with a primary particle with a granitic shell surrounding a core made up of oriented PAH clusters. At high temperatures, PAH molecules on the surface, randomly oriented, start to align with each other due to chemical equilibrium and turn to 'face-on-surface' configurations, undergoing hydrogenation reactions and forming layers of PAHs. As the soot particle matures, the graphitic shell grows, from outside to inside. Although this theory disagrees to the molecular dynamics investigation on a melting coronene $C_{24}H_{12}$ clusters that becomes increasingly disordered at high temperatures [29], further evidence for the surface shell theory is an observation that nascent particles have a 'liquid-like' appearance 2.3 in the early stage of flames but quickly turns into solid in the later stage [27].

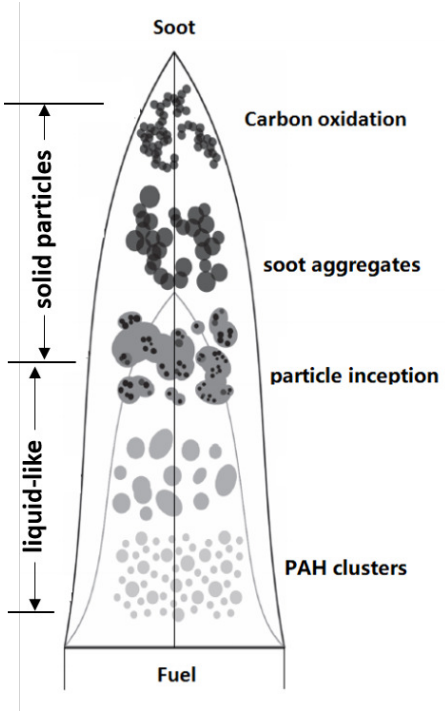

Fig. 2.3 A conceptualisation of soot formation process in a laminar coflow flame. The illustration is adapted from [30]

Last but not the least, soot growth is a sophisticated and continuous progress throughout the process of soot formation. PAH molecules get larger by absorbing hydrocarbon species on the active sites and reacting or colliding with other PAHs, stacking together and forming soot nuclei. For mature soot particles, hydrocarbon species and PAHs also react on the active sites of PAHs on the periphery. Moreover, a variety of particles collide with each other, contributing to fractal-aggregates of different size. However, particle size does not increase consistently in each stage. For instance, particle growth is in relation with the particle size distribution, like hydrocarbon addition and PAH condensation on the active sites of the total surface area, the variation in collision rates with different particle sizes [31] during coagulation process. On the other hand, experiments also observed the phenomenon of soot aging: the activity of surface sites accessible for reactions decays with an increasing particle age [19, 31, 32] and in high temperatures [33, 34].

2.1.2 Experimental techniques on sooting flames

Advanced experimental measurements are mainly responsible for the process on understanding physical and chemical processes of soot formation and offer data

sets for the validation of modelling. Typical experimental techniques are roughly classified into two categories: non-intrusive and intrusive.

Non-intrusive techniques

Non-intrusive techniques, mainly the optical tests by laser diagnostics, are able to capture the soot volume fraction and concentration of gaseous species in the flames. Soot volume fraction is commonly measured using light extinction (line-of-sight attenuation) [27, 35, 36], according to the Beer-Lambert law that a high-intensity laser beam is attenuated as it travels through a flame due to a combination of absorption and scattering by soot particles. The elastic light scattering (ELS), captured a detector (usually a CCD camera) at a fixed a angle or multiple different angles with the incident laser beam, is able to determine the spatial distribution of soot [27, 37] or other particles [38]. In addition, with the technique of laser-induced incadescenece (LII), soot volume fraction can also be measured using the radiative emission (LII signal) from soot particles heated by a high-intensity laser pulse [39–41]. Furthermore, the particle size distribution can be roughly reproduced by anaylsing the LII signals with a certain algorithm at different time intervals after the particles are heated. As an auxiliary measure, laser-induced fluorescence (LIF) is exploited to obtain the presence and abundance of a certain molecule, whose emitted wavelength is different from that of other molecules after they are excited to a higher energy level by the absorption of laser light [42, 43].

Intrusive techniques

Although the intrusive measurements affect flames, they provides more detailed information of the morphology and inner structure of soot particles or even the chemical composition of soot. After extracted from flames, samples of soot particles are imaged with thermophoretic technique by the transmission electron microscopy (TEM). Sheet-like PAH layers [44], including PAH fringe length, inter-layer spacing and even radius of curvature [45], and the surface shell formation (SSF) structure [28] have been observed. Recent advances in helium ion microscopy is able to image incipient soot of a few nanometers without damage [46]. Laser microprobe spectroscopy [47] and photoionisation aerosol mass spectroscopy [48] are able to analyse the chemical composition of soot.

The scanning mobility particle sizer (SMPS) or nano-differential mobility analyser (Nano-DMA) is another commonly used intrusive facility to directly capture particles of different sizes and achieve the PSD over the size range from 3 to hundreds of

nanometer, based on the principle of the mobility of charged particle in an electric field [49–52].

2.1.3 Modelling of soot kinetics

Kennedy [53] classified soot models in three categories in a seminar review: empirical correlations, semi-empirical models and models with detailed chemistry. Herein, empirical correlations, which were dominant at that time, relate soot to overall parameters (usually in engines) but are not suited for coupling with fluid dynamics. Since significant progress has been made in detailed models, Rigopoulos [54] classified the models of soot kinetics in the following way:

Semi-empirical non-precursor models

Temperature and mixture fraction are usually related to the soot formation in the category. They are still implemented in CFD codes or commercial software of general purposes, but largely outdated for research purposes now.

Tesner et al. [55] links soot formation with temperature by postulating a chain reaction model for soot. The two-equation model for number density of 'radical nuclei' and soot particles was resolved. As the first model studying turbulent sooting flames [56, 57], it could not reflect the true mechanisms for soot formation.

Another model endowed with historical importance is proposed by Moss et al. [58], by relating the soot formation rates to mixture fraction, and describe soot in terms of number density n and volume fraction f_v. The equations are

$$\frac{d}{dt}\left(\frac{n}{N_\mathrm{A}}\right) = \xi_a - \xi_b \left(\frac{n}{N_A}\right)^2 \tag{2.1}$$

$$\rho_\mathrm{s}\frac{df_\mathrm{v}}{dt} = \xi_c n + \xi_d \tag{2.2}$$

where ρ_s is the soot density and N_A is Avogadro's number. The parametric modelling includes nucleation (ξ_a, ξ_d), surface growth $(\xi_c n)$ and coagulation $(\xi_b (n/N_A)^2)$. This model makes an important step in terms of modelling the physical processes in soot formation, although the concept of correlation between these processes with mixture fraction is not completely realistic. In addition, Kennedy et al. [59] also related soot volume fraction to mixture fraction. Despite just a one-equation model, a minimum number of variables are kept for soot formation. It is also noticeable to lead the earliest application of a transported probability density function (pdf) method to a turbulent sooting flame.

On the other hand, essentially, the semi-empirical chemical models and detailed chemical models are based on the consensus that the combustion community has reached on fundamental physics of soot. In a first stage, macro-molecular PAHs contribute to soot precursors and nascent soot particles [28] such that particle nucleation is linked to relevant PAH species [23, 60–62]. Second, acetylene (C_2H_2) contributes to the surface growth of soot particles as it is augmenting the hydrocarbon content of soot. Acetylene-based models [6, 8, 63, 64], including the Hydrogen-Abstraction-Acetylene-Addition (HACA) [23, 60–62, 65, 66], are extensively applied in the soot formation modelling. Third, the hydroxyl radical (OH) and molecular oxygen (O_2) are the species which are the most effective in oxidising soot particles.

Semi-empirical chemical models

The semi-empirical precursor models relate soot to chemical species such as C_2H_2 wtih an empirical kinetics. Relatively detailed chemistry is required in order to couple the semi-empirical chemical model with the reacting flows. For example, nucleation is described via a global reaction involving C_2H_2 [67] and sometimes also C_6H_6 [64] .

$$C_2H_2 \rightarrow 2C(s) + H_2, \quad R_n = k_n(T)[C_2H_2] \tag{2.3}$$

$$C_6H_6 \rightarrow 6C(s) + 3H_2, \quad R_n = k_n(T)[C_6H_6] \tag{2.4}$$

where C(s) denotes the soot, k_n is a function of an Arrhenius type expression. As an extension, Lindstedt [68] assumed the nucleation rate to be eight times the formation rate of $C_{10}H_7$ and $C_{14}H_{10}$.

For the surface growth, a number of studies have postulated that surface growth is proportional to surface area S, as well as on the concentration of acetylene [8, 64],

$$R_g = k_g(T)S[C_2H_2] \tag{2.5}$$

The main oxidising species of soot are considered to be O_2 and OH, and the semi-empirical models are proposed by Nagle and Strickland-Constable [69], Lee et al. [70] and Neoh et al. [71].

Detailed chemical models

These models include PAH chemistry and detailed aerosol dynamics. Detailed gas-phase chemistry is required and therefore the overall approach becomes more expensive. Detailed soot models have mainly be employed on ideal reactors and

1-D laminar flows, but also been applied to turbulent flows in an increasing number of studies.

PAHs are hydrocarbons with two or more aromatic rings and play an important tole to bridge gas-phase chemistry and soot nucleation. Although the transition from PAHs to soot is not clearly understood, but the models have been imposed. In the early stage, PAH growth was compiled by a lumped-prototype model: the HACA mechanism [7, 19, 72], based on an analogy to the growth of benzene by acetylene addition.

$$\begin{aligned} &A_i + H \rightleftharpoons A_i \cdot + H_2 \\ &A_i \cdot + C_2H_2 \rightleftharpoons A_iC_2H_2 \cdot \\ &A_iC_2H_2 \cdot + C_2H_2 \rightleftharpoons A_{i+1} + H \end{aligned} \tag{2.6}$$

where A_i is a PAH molecule with i aromatic rings. The growth of PAHs terminates at some point such as pyrene ($C_{16}H_{10}$ with four rings) and further growth is described as dimerisation process between PAH molecules. However, as in recent times, gas-phase chemical mechanisms have included more detailed PAH kinetics. Therefore, the lumped-prototype model has been replaced by directly introducing PAH molecule and the soot nuclei are modelled as dimerisation of PAH molecules [60–62, 73].

However, the HACA mechanism has still vibrantly been applied in modelling surface growth of soot, which was firstly introduced by Appel et al. [60]. The elementary reactions are an analogy with the HACA for PAH growth (Eq. 2.6), summarised by the following steps:

$$\begin{aligned} &C(s) - H + H \rightleftharpoons C(s) \cdot + H2 \\ &C(s) \cdot + H \rightarrow C(s) - H \\ &C(s) \cdot + C_2H_2 \rightarrow C(s) - H + H \end{aligned} \tag{2.7}$$

Further surface reaction steps including OH and O_2 are also added to the HACA mechanism for the oxidising process.

$$\begin{aligned} &C(s) \cdot + O_2 \rightarrow 2CO + \text{products} \\ &C(s) \cdot + OH \rightarrow CO + \text{products} \end{aligned} \tag{2.8}$$

The general form of C_2H_2 addition rate for a soot particle with the surface area S is,

$$R_{\text{HACA}} = k_g \alpha \chi_s N_i \tag{2.9}$$

where k_g is the rate coefficient, χ_s is the number density of surface sites obtained by a steady-state approximation on the participating gas-phase species, N_i is the number density of soot particles in a particular size range i and α is an active ratio for the surface sites.

However, despite this general agreement, differences remain in the detailed chemical models regarding the transition from gas to particles and the model constants. Appel et al. [60], for example, modelled nucleation as the collision of two A_4 (pyrene $C_{16}H_{10}$) molecules, while Blanquart and Pitsch [61] expressed it as the self collision of PAH molecules from A_2 ($C_{10}H_8$) to A_4 and Wang et al. [62] considered both the self and heterogeneous dimerisation of PAHs from A_4 to A_7 (coronene, $C_{24}H_{12}$). As a second example, we mention the fraction of active sites α in the HACA mechanism [19] which is often taken as constant for a particular flame configuration [19, 66]. Since experimental observations on particle surface ageing suggest a decrease fraction of active sites, α has also been represented as a function of particle size [60], local flame temperature [74, 75] or particle residence time, particularly in Lagrangian, trajectory-based methods for solving the PBE. The differences in modelling α may, possibly, be a consequence of using different reaction mechanisms or of analysing different flames [19].

More detailed transformations have introduced the concept of acetylene addition and hydrogen addition on the various active sites of a PAH molecule, shown in Fig. 2.1. For example, Yapp et al. [76] presented a total of 22 elementary reactions serving as jump processes in the Monte Carlo aromatic site model. Although these elementary reactions are further approximating to the soot physics, their reaction rates are still estimated via steady-state assumptions and, unfortunately, this model has to be calibrated with the parameter α as well. Therefore, efforts to successfully simulate sooting flames thus rely on establishing a reasonable and moderately detailed physical model.

2.2 Population balance modelling and its numerical methods

The Population Balance Equation (PBE) is of central importance to the dynamics of polydispersed aerosol systems. It describes the evolution of the distribution of particles in terms of one or more properties, for instance, the most important of which is usually a measure of particle size or volume, as independent coordinates.

General reviews of the PBE can be found in [77–80], while [81] focuses on its coupling with reacting flows.

The PBE can be formulated in a discrete or a continuous form. The discrete form was developed firstly by [82] and is a system of ODEs describing the temporal evolution of the number of particles of every possible size. The range of particle sizes is usually enormous - e.g. for particles ranging from 1 nm - 1 μm in diameter, 10^9 units must be accounted for - and therefore its numerical solution is too expensive for practical problems. The problem is aggravated when the PBE must be coupled with fluid dynamics and the distribution is spatially dependent. Furthermore, surface processes such as growth and oxidation involve the addition or removal of units as small as a single atom, which must therefore be the smallest unit in a discrete PBE featuring such processes. These considerations lead to the formulation of a continuous PBE.

The continuous PBE is a single integro-partial differential equation whose derivation has been discussed in a number of references [77–81]. The PBE formulation employed in this paper is the continuous PBE in terms of particle volume, v, a description suitable for problems involving coagulation because the volume is conserved in a coagulation event and the kernel can be assumed as a simpler form. We define the number density, $n(v,t)$, as the number of particles per unit of particle volume (and possibly per unit volume of physical space, if considered as a concentration in a spatially dependent PBE) at an instance time t. The PBE formulation for a problem involving nucleation, surface processes (such as growth and oxidation) and coagulation is:

$$\begin{aligned}\frac{\partial n}{\partial t} + \frac{\partial (Gn)}{\partial v} =& B\delta(v - v_0) \\ &+ \frac{1}{2}\int_0^v \beta(v-w,w)n(v-w)n(w)dw - \int_0^\infty \beta(v,w)n(v)n(w)dw\end{aligned} \tag{2.10}$$

where B is the nucleation rate, G is the volumetric rate of change due to surface processes and $\beta(v,w)$ is the coagulation kernel, i.e. the function giving the rate of coagulation between particles of volumes v and w, and the dependence of n on v and t is omitted where appropriate. Coagulation is expressed via the last two terms, which represent a source and a sink, and take the form of integrals due to the need for accounting for all possible particle pairs. Together with initial conditions for the number density, the PBE constitutes an initial value problem.

While we focus on the univariate PBE based on soot particle volume, more detailed multivariate population balance models for soot have been advanced in the course of the last decade. Blanquart and Pitsch [61] and Kholghy et al. [28], for instance, described a soot particle in terms of its volume, surface area and the hydrogen content on the surface or the hydrogen/carbon ratio.

2.2.1 Classification of the numerical methods for solving the PBE

The solution of the PBE poses severe challenges, arising from its integro-differential and non-linear nature. Analytical and similarity solutions of the PBE can be obtained only for a few special cases, usually involving only one or two of the processes in the PBE and without coupling with kinetics. They are useful for bench-marking numerical methods, and reviews of them can be found in [77–80]. Several challenges, however, are encountered in developing an efficient and accurate discretisation method for the PBE. First of all, the domain spans several orders of magnitude, with different processes occurring at different scales: nucleation, for example, is a localised source appearing at the one end of the domain, while coagulation spreads the distribution towards larger sizes. Secondly, it is not straightforward to obtain a discretisation of the coagulation terms that conserves the first moment of the distribution in an arbitrary non-uniform grid. The first moment is proportional to the total particle mass, hence an error in its conservation implies an error in the mass balance. Several methods aim to accomplish conservation at the expense of accuracy in the prediction of the distribution. Finally, the growth term is a first-order derivative and can give rise to sharp fronts. Work so far has resulted in a number of solutions to these problems, but it is difficult to obtain a method that strikes a balance between these objectives, a problem that stems from the fact that processes of a very different nature and mathematical behaviour (nucleation, growth and coagulation) must be accommodated.

Moment-based methods

Methods belonging to this family aim to compute the transport equation of its moments rather than the distribution itself. The k-th moment is defined as

$$M_k = \int_0^\infty v^k n(v) dv \tag{2.11}$$

where the zeroth moment is physically the total number of particle while the first moment represents the total particle volume. For the numerical solution of the

PBE, different moment-based methods have been developed in the past. The main advantage of moment methods is the reduction in the number of variables. Hulburt and Katz [5] pioneered the method of moments which is based on a reduction of the particle property distribution to a few low order moments. Since their first conception, moment methods have developed into the most popular approaches for describing particulate phases in spatially inhomogeneous flows. From an engineering perspective, low order moments such as the total particle number density or volume fraction [7] are of importance because they can frequently be directly accessed by experimental measurement techniques. Now, the two-equation model (with respect of zeroth moment and first moment) is still popularly employed in research [8, 83].

On the minus side, besides the lack of prediction of the distribution for cases where it is of interest, moment methods generally require an assumption on the shape of the particle property distribution such that the rates of particle surface growth, coagulation and breakage which appear in the moment transport equations can be expressed in a closed form. For example, the surface area, a moment of fractional order, needs to be calculated to model surface growth processes. Various approximate methods have been proposed to provide closure in the moment-based method, involving the underlying ideas: (1) One approach is based on series expansion of the number density, first proposed in [5, 84], but has found very limited applications; (2) A second approach is to presume the shape of the distribution. This approach is used extensively in aerosols (see e.g. [85, 86]) but not often in soot, where the combination of surface processes, coagulation and aggregation as well as the effect of spatial variation of precursors gives rise to considerable variability and often bimodal features to the distribution, so the assumption of a presumed shape is not adequate. (3) A third class of methods are to obtain the fractional moments by interpolation like the method of moments with interpolative closure (MOMIC), this is achieved by polynomial interpolation of integer order moments [6, 87]. And (4) finally, the fourth family is based on approximating the moment integral with quadrature whose coefficients are evolving in time: this family of methods originate in the Quadrature Method of Moments (QMOM). Here, integrals of the particle property distribution are approximated using a quadrature rule and the weights and abscissas are linked to low order moments [88, 89]. For example, the integrated moment is approximated in the following way:

$$\int_0^\infty v^k n(v) dv = \sum_{i=1}^{n} w_i v_i^k \tag{2.12}$$

Proceeding a two-stage process, updating the moments and inverting a matrix, the quadrature coefficients are obtained. This idea is taken further in the direct quadrature method of moments (DQMOM), where evolution equations for the weight and abscissas are solved instead of moment equations. Alternative formulations, like for example the hybrid method of moments (HMOM), employ a combination of these concepts of MOMIC and DQMOM. However, one issue with the closure scheme in the moment methods is that they cannot be ensured in some of the closure schemes or in the spatial transport of the moments [90, 91].

At a low computational cost, moment methods allow for the prediction of ensemble averaged quantities of the particles and are, thus, particularly amenable to be incorporated into more complicated turbulent combustion models, even for geometrically intricate applications such as diesel engines and gas turbines [9, 92]. However, owing to the non-uniqueness in reconstructing a distribution from a finite number of moments, the method of moments is not suitable for the direct resolution of the particle property distribution.

Stochastic methods

In order to circumvent assumptions on the shape of the particle size distribution, researchers have applied stochastic methods, sectional approaches and direct discretisation schemes to the PBE. Stochastic or Monte Carlo-type methods are based on a statistically equivalent reformulation of the PBE in terms of Lagrangian trajectories of soot particles [93, 94]. This representation permits a much more detailed description of particle inception and interaction processes, including, for example, the polymerisation of polycyclic aromatic hydrocarbons (PAH) [20] and changes in morphology and internal structure of nanoparticles [95, 96]. Monte Carlo methods further circumvent the "curse of dimensionality" as particles are described by more than a single particle property, by constructing an ensemble of particles and subjecting them to random events for each process in the PBE at every time step, consistent with the rate of that process (see e.g. [97]).

The main drawback is that they are computationally very expensive, because large numbers of particles are needed to obtain convergence, and hence have been used employed for kinetic investigations in ideal or partially-stirred reactors and 1-D laminar flames. From this perspective, the moment and discretisation methods are suitable for multidimensional spatially dependent problems involving laminar or turbulent flow. Moreover, owing to the tremendous computational expense, the particle size is often limited to the PAH scale. In addition, a severe challenge in such

physically detailed description is related to the identification of many constitutive parameters, only a minority of which can be calibrated by measurements, while the remaining ones have to be linked to measurements of integral quantities.

Sectional methods and discretisation methods

Discretisation methods aim to predict the distribution by discretising the domain of the independent variable, and do not suffer from closure issues or assumptions on the shape of the particle size distribution. In recent years, researchers have also investigated directly discretising the PBE in particle property space. Gelbard and Seinfeld [98] and Rigopoulos and Jones [99], for example, applied a collocation-based finite element method, while Qamar et al. [100] investigated the accuracy of different high resolution finite volume schemes. In processes that are dominated by particle nucleation and growth, the number of grid points in particle property space can be significantly reduced by combining a direct discretisation scheme with grid adaptivity [101, 102]. This is particularly advantageous in spatially inhomogeneous reactors, where the resolution requirements in particle property space may vary not only in time, but also across the flow domain [103]. In many past investigations, about 30 grid points were invoked to represent the particle property distribution [104, 105], although much more stringent resolution requirements were also reported, especially in the absence of coagulation and aggregation [106, 107]. A more thorough classification of the discretisation methods will be discussed in Section 3.1.

2.2.2 The spatially inhomogeneous population balance equation

In a continuous approach, soot is commonly described in terms of the number of particles per unit of volume in physical space. The PSD is important for modelling soot formation for two main reasons. Firstly, the rates of surface processes such as growth and oxidation depend on the surface area and hence on the particle size distribution, and the aggregation rate is also size-dependent. Therefore, knowledge of the distribution is crucial, even in cases where only the integral properties (such as soot volume fraction) are required to be predicted. Secondly, new and more stringent regulations on particulate emissions limit the number of smaller particles being emitted and not just the total mass. Prediction of the particle size distribution can thus aid in improving the design of equipment that meets these aims.

Here, we specifically consider particle volume v as the single defining property; the number density $n(v, \mathbf{x}, t)\,dv$ then corresponds to the number of particles with volume in $[v, v + dv]$ at the location $\mathbf{x}$ and time t per unit of physical space, referred

as the particle size distribution. Formally, the population balance equation (PBE) is a statement on the continuity of number density in $(v, \mathbf{x})$, representing source and sink processes for the creation and removal of number density, given by

$$\begin{aligned}\frac{\partial n(v,\mathbf{x},t)}{\partial t} + \frac{\partial [U_j n(v,\mathbf{x},t)]}{\partial x_j} + \frac{\partial [G(v,t) n(v,\mathbf{x},t)]}{\partial v} = \frac{\partial}{\partial x_i}\left(D_p \frac{\partial n(v,\mathbf{x},t)}{\partial x_i}\right) \\ + \dot{B}(\mathbf{Y})\delta(v - v_0) + \frac{1}{2}\int_0^v \beta(v-w,w) n(v-w,\mathbf{x},t) n(w,\mathbf{x},t)\, dw \\ - \int_0^\infty \beta(v,w) n(v,\mathbf{x},t) n(w,\mathbf{x},t)\, dw\end{aligned} \tag{2.13}$$

The spatial inhomogeneous population balance equation is resolved with two fractional steps, the spatial convection-diffusion terms and the volumetric convection-source terms, respectively,

$$\frac{\partial n}{\partial t} + \frac{\partial (U_j n)}{\partial x_j} = \frac{\partial}{\partial x_i}\left(\rho D_p \frac{\partial n(v,\mathbf{x},t)}{\partial x_i}\right) \tag{2.14}$$

$$\begin{aligned}\frac{\partial n}{\partial t} + \frac{\partial (G n)}{\partial v} =& \dot{B}(\mathbf{Y})\delta(v - v_0) + \frac{1}{2}\int_0^v \beta(v-w,w) n(v-w,\mathbf{x},t) n(w,\mathbf{x},t)\, dw \\ & - \int_0^\infty \beta(v,w) n(v,\mathbf{x},t) n(w,\mathbf{x},t)\, dw\end{aligned} \tag{2.15}$$

The spatial convection-diffusion terms are discretised as the conservations of equations with the finite volume scheme in the space domain. The surface growth and oxidation is described by a term involving a first derivative with respect to particle volume. The nucleation term is described by a delta function where the nucleation rate $\dot{B}(\mathbf{Y})$ is non-zero only over the interval including the nuclei volume v_0.

The finite volume discretisation is used in v space for the volumetric convection-source fractional step. By integrating Eq. 2.15, we get

$$\frac{\partial n_i}{\partial t} + \frac{1}{\Delta v_i}\left[n \cdot G(v)\right]_{v_{i-1}}^{v_i} = \int_{v_{i-1}}^{v_i} \left(\dot{B}(\mathbf{Y})\delta(v - v_0)\right) + C_\mathrm{d} \tag{2.16}$$

where C_d denotes the discretised coagulation term,

$$C_\mathrm{d} = \frac{1}{2\Delta v_i}\int_{v_{i-1}}^{v_i}\left[\int_0^v \beta(v-w,w) n(v-w) n(w) dw - \int_0^\infty \beta(v,w) n(v) n(w) dw\right] dv \tag{2.17}$$

In Chapter 3, a conservative discretisation method for the PBE with respect to the coagualtion process will be proposed, to be combined with the discretisation for the nucleation and growth processes.

For the growth term, a total variation diminishing (TVD) scheme is employed [108]:

$$[nG(v)]_{v_i} = G(v_i)\left[n_{u(v_i)} + \frac{\psi_i}{2}\left(n_{u(v_i)} - n_{uu(v_i)}\right)\right] \tag{2.18}$$

where $u(v_i)$ and $uu(v_i)$ are the indices of the two cells upstream of node v_i, and ψ_i indicates the value of the flux limiter at cell face v_i [100], defined as

$$\psi(r_i) = \max\left(0, \min\left(2r, \min\left(\frac{1}{3} + \frac{2r_i}{3}, 2\right)\right)\right) \tag{2.19}$$

The argument r_i of this function is the upwind ratio of two consecutive number density gradients:

$$\begin{cases} r_i^+ = \dfrac{n_{i+1} - n_i}{n_i - n_{i-1}}, & G(v_i) > 0. \\ r_i^- = \dfrac{n_i - n_{i+1}}{n_{i+1} - n_{i+2}}, & G(v_i) < 0 \end{cases} \tag{2.20}$$

2.3 The fluid dynamics for laminar diffusion flames and its numerical framework

Our in-house CFD code, named BOFFIN, is a low-Mach number formulation for density-varying flows. It can be directly used for laminar reactive or non-reactive flows in the two or three dimensional domain in either Cartesin or cylindrical coordinates. It has also been enhanced for Reynolds-averaged Navier–Stokes equations (RANS) and Large Eddy Simulation (LES) by adding respective models as well as Direct Numerical Simulation (DNS) for turbulent flows. This program is written in Fortran 77/95, with MPI (Message Passing Interface) subroutines for multiprocessor/multicore system architecture. This code is formally discretised with second order in space and, in low-Mach laminar flows, the artificial diffusion can be controlled. Written in finite-volume scheme, velocity components and other variables are stored in staggered grids, making it a very important feature to conserve the flow rate and scalars.

2.3.1 Conservation equations

A generic multicomponent, anisochoric flow is governed by the conservations law of mass, momentum (Navier-Stokes equation, expressing a general conservation principle of Newton's Second Law in fluid dynamics) and energy. For breity, these equations are resolved in Cartesian frame, as

The continuity equation:

$$\frac{\partial \rho}{\partial t} + \frac{\partial \rho U_j}{\partial x_j} = 0 \tag{2.21}$$

The conservation of momentum:

$$\frac{\partial \rho U_j}{\partial t} + \frac{\partial \rho U_j U_i}{\partial x_j} = -\frac{\partial P}{\partial x_i} + \frac{\partial \zeta_{ij}}{\partial x_j} + F_{\mathrm{v}} \tag{2.22}$$

where F_{v} represents volume forces (such as gravity). The stress tensor, ζ_{ij}, is proportional to strain rate S_{ij} for a Newtonian fluid based on the Stokes hypothesis

$$\zeta_{ij} = 2\mu \left(S_{ij} - \frac{1}{3} S_{kk} \delta_{ij} \right) \tag{2.23}$$

The strain rate is by definition,

$$S_{ij} = 2 \left(\frac{\partial U_i}{\partial x_j} + \frac{\partial U_j}{\partial x_i} \right) \tag{2.24}$$

The transport equations: The general form of the transport equation of a scalar, ϕ_k is presented by

$$\frac{\partial \rho \phi_k}{\partial t} + \frac{\partial \rho U_j \phi_k}{\partial x_j} = \frac{\partial}{\partial x_j} \left[\Gamma_k \frac{\partial \phi_k}{\partial x_j} \right] + S_k \tag{2.25}$$

where Γ_k is a diffusion coefficient and S_k is a source term. This equation can be particularised for reactive scalars:

The mass conservation equation for species

$$\frac{\partial \rho Y_k}{\partial t} + \frac{\partial}{\partial x_j} \left[\rho \left(U_j + V_{k,j} \right) Y_k \right] = \dot{\omega}_k \qquad \text{for} \quad k = 1, \cdots, N \tag{2.26}$$

where $V_{k,i}$ is the i-component of the diffusion velocity of species k and $\dot{\omega}_k$ is the reaction rate of species k. By definition in the mixture-average formulations, the diffusion velocity is related to the species gradients by a Fickian formula, as

$$V_{k,j} = -\frac{1}{X_k} D_{k\mathrm{m}} d_{k,j} - \frac{D_k^{\mathrm{T}}}{\rho Y_k} \frac{\partial(\ln T)}{\partial x_i} \tag{2.27}$$

where X_k, Y_k are the mole fraction and mass fraction of species k in the mixture, respectively. $D_{k\mathrm{m}}$ and D_k^{T} are the diffusion coefficients for species k due to the gradients of species concentration and temperature in the mixture. The vector $d_{k,j}$ incorporates the effects of various state variable gradients and is given by [109]

$$d_{k,j} = \frac{\partial X_k}{\partial x_j} + (X_k - Y_k) \frac{\partial(\ln P)}{\partial x_j} \tag{2.28}$$

where the second term with respect to pressure gradient is neglected for the laminar diffusion flames in the open air.

Therefore, the mass transport equation for species k is transformed to

$$\begin{aligned} \frac{\partial \rho Y_k}{\partial t} + \frac{\partial}{\partial x_j}\left(\rho U_j Y_k\right) &= \frac{\partial}{\partial x_i}\left(\rho D_k^{\mathrm{m}} \frac{W_k}{\bar{W}} \frac{\partial X_k}{\partial x_i}\right) + \frac{\partial}{\partial x_i}\left(D_k^{\mathrm{T}} \frac{\partial(\ln T)}{\partial x_i}\right) + \dot{\omega}_k \\ &= \underbrace{\frac{\partial}{\partial x_j}\left[\rho D_k^{\mathrm{m}} \frac{\partial Y_k}{\partial x_j}\right]}_{\textbf{O}\text{riginal diffusion}} + \underbrace{\frac{\partial}{\partial x_j}\left[\rho D_k^{\mathrm{m}} Y_k \frac{\partial(\ln \bar{W})}{\partial x_j}\right]}_{\textbf{M}\text{olecularWeight}} + \underbrace{\frac{\partial}{\partial x_i}\left(D_k^{\mathrm{T}} \frac{\partial(\ln T)}{\partial x_i}\right)}_{\textbf{T}\text{hermophoresis}} + \dot{\omega}_k \end{aligned} \tag{2.29}$$

The energy equation with respect to total enthalpy

The energy equation is resolved in terms of total enthalpy to obtain the temperature which determines the chemical reaction rates,

$$\frac{\partial \rho h}{\partial t} + \frac{\partial}{\partial x_j}\left(\rho U_j h\right) = \dot{\omega}_{\mathrm{T}} + \dot{Q} - \frac{\partial \dot{q}_j}{\partial x_j} \tag{2.30}$$

where the terms $\dot{\omega}_{\mathrm{T}}$, $\dot{Q}$ and $-\frac{\partial q}{\partial t}$ are the heat source from chemical reactions, external heat source and energy flux inside the fluid, respectively. In the laminar diffusion flame which is of low speed and low Mach number, the terms of work by the volume force, energy transport by the viscous stress and work by the pressure variations are all neglected.

The energy flux contains the contribution resulting from the inter-diffusion of various substances and thermal conductive flux and the Dufour effect which is due to a mass concentration gradient occurring as an accompanying effect of irreversible processes.

$$\dot{q}_j = \sum_{k=1}^{K} \rho Y_k V_{k,j} h_k - \lambda \frac{\partial T}{\partial x_j} - \sum_{k=1}^{K} \frac{RT}{W_k X_k} D_k^{\mathrm{T}} d_{k,j} \tag{2.31}$$

$$\frac{\partial \rho h}{\partial t} + \frac{\partial}{\partial x_j}\left(\rho U_j h\right) = \underbrace{\frac{\partial}{\partial x_j}\left(\rho D \frac{\partial h}{\partial x_j}\right) - \sum_k \frac{\partial}{\partial x_j}\left[\rho (D - D_k) h_k \frac{\partial Y_k}{\partial x_j}\right]}_{\textbf{O}\text{riginal} \quad \text{differential} \quad \text{diffusion}}$$
$$\underbrace{+\frac{\partial}{\partial x_j}\left[\rho Y_k D_k h_k \frac{\partial (\ln W_k)}{\partial x_j}\right]}_{\textbf{M}\text{olecular} \quad \text{Weight}}$$
$$\underbrace{+\frac{\partial}{\partial x_j}\left[\rho Y_k D_k^{\mathrm{T}} h_k \frac{\partial (\ln T)}{\partial x_j}\right]}_{\textbf{T}\text{hermophoresis}}$$
$$\underbrace{+\frac{\partial}{\partial x_j}\left(\sum_k \frac{RT}{W_k X_k} D_k^{\mathrm{T}} \frac{\partial X_k}{\partial x_j}\right)}_{\textbf{D}\text{ufour} \quad \text{effect}} \tag{2.32}$$

where h_k is the specific enthalpy of species k. In order to account for the reduction in mixture enthalpy $\dot{Q}$, we include a radiation model based on the assumption of optical thinness [110]. This model has been used to account for radiation of water vapor, CO_2, CH_4, CO and N_2. The modeling constants for the curve fits of the Planck absorption coefficients are published on International Workshop on Measurements and Computations of Turbulent Nonpremixed Flames.

2.3.2 Thermodynamic and transport parameters

Enthalpy and the specific heat coefficients

In the case of an ideal mixture of gases, the mixture enthalpy is represented by

$$h = \sum_k Y_k h_k \tag{2.33}$$

where the specific enthalpy of a species h_k comprising enthalpy of formation h_k^0 and the sensible enthalpy, depends only on the temperature in an open atmosphere for an ideal gas

$$h_k = h_k^0 + \int_{T_0}^{T} C_{\mathrm{p},k}(T)\mathrm{d}T \tag{2.34}$$

where the specific heat capacities $C_{\mathrm{p},k}$ are obtained from the JANAF polynomials,

$$C_{\mathrm{p},k}(T) = a_0 + \sum_{n=1}^{6} a_n T^n \tag{2.35}$$

The temperature $T = f(h, Y_k)$ is resolved by an iterative method.

Viscosity

The viscosity of a single component is given by the standard kinetic theory expression

$$\mu_k = \frac{5}{16} \frac{\sqrt{\pi W_k k_B T}}{\pi \sigma_k^2 \Omega^{(2,2)*}} \tag{2.36}$$

where σ is the Lennard-Jones potential, k_B is the Boltzmann constant. $\Omega^{(2,2)*}$ is the (2,2) collision integral, which depends on the reduced temperature

$$T_k^* = \frac{k_B T}{\epsilon_k^*} \tag{2.37}$$

and the reduced dipole moment, given by

$$\epsilon_k^* = \frac{1}{2} \frac{\mu_k^2}{\epsilon_k \sigma_k^3} \tag{2.38}$$

In the above expression, ϵ_k is the Lennard-Jones potential well depth and μ_k is the dipole moment. The collision integral value is determined by a quadratic interpolation of the tables based on Stockmayer potentials given by Monchick and Mason [111].

In case of the mixture-averaged viscosity, the semi-empirical formula proposed by Wilke [112],

$$\mu^m = \sum_k \frac{X_k \mu_k}{\sum_j X_j \Phi_{jk}} \tag{2.39}$$

where Φ_{jk} is given by the equation

$$\Phi_{kj} = \frac{1}{\sqrt{8}} \left(1 + \frac{W_k}{W_j}\right)^{-\frac{1}{2}} \left(1 + \left(\frac{\mu_k}{\mu_j}\right)^{\frac{1}{2}} \left(\frac{W_j}{W_k}\right)^{\frac{1}{4}}\right)^2 \tag{2.40}$$

Diffusion coefficient

The binary diffusion coefficient D_{jk} is given in terms of pressure and temperature as,

$$D_{kj} = \frac{3}{16} \sqrt{\frac{2k_B^3 T^3}{\pi W_{jk}}} \frac{1}{\sigma_{jk}^2} \Omega^{(1,1)*} \tag{2.41}$$

where m_{jk} is the reduced molecular weight for the (j,k) species pair

$$W_{jk} = \frac{W_j W_k}{W_j + W_k} \tag{2.42}$$

and σ_{jk} is the reduced collision diameter. $\Omega^{(1,1)*}$ is the (1,1) collision integral, which depends on the reduced temperature, T_{jk}^* which in turn depend on the species

dipole moments μ_k and palarisabilities α_k. In computing the reduced quantities, we consider two cases, depending on whether the collision partners are polar or non-polar. We follow the the routines in the Theory Manual of Chemkin Software [113].

In practice, the equivalent diffusion coefficient of species k in the multi-component mixture is

$$D_k^{\mathrm{m}} = \frac{\sum_{j \neq k} W_j}{\bar{W} \sum_{j \neq k} X_j / D_{jk}} \tag{2.43}$$

Thermal conductivity

The thermal conductivity for pure species are computed only for the purpose of evaluating the mixture-averaged thermal conductivity. Here the individual species conductivity is assumed composed of translational, rotational, and vibrational contributions as given by Peters and Warnatz [114].

$$\lambda_k = \frac{\eta_k}{W_k} \left(f_{\mathrm{trans}} C_{\nu,\mathrm{trans}} + f_{\mathrm{rot}} C_{\nu,\mathrm{rot}} + f_{\mathrm{vib}} C_{\nu,\mathrm{vib}} \right) \tag{2.44}$$

where

$$f_{\mathrm{trans}} = \frac{5}{2} \left(1 - \frac{2 C_{\nu,\mathrm{rot}} A}{\pi C_{\nu,\mathrm{trans}} B} \right) \tag{2.45a}$$

$$f_{\mathrm{rot}} = \frac{\rho D_{kk}}{\eta_k} \left(1 + \frac{2 C_{\nu,\mathrm{rot}}}{\pi C_{\nu,\mathrm{trans}}} \right) \tag{2.45b}$$

$$f_{\mathrm{vib}} = \frac{\rho D_{kk}}{\eta_k} \tag{2.45c}$$

and,

$$A = \frac{5}{2} - \frac{\rho D_{kk}}{\eta_k} \tag{2.45d}$$

$$B = Z_{\mathrm{rot}} + \frac{2}{\pi} \frac{5}{3} C_{\nu,\mathrm{trans}} \tag{2.45e}$$

The self-diffusion coefficient comes from Equ. 2.42. The density ρ comes from the equation of state for an ideal gas. The rotational relaxation collision number is a parameter that we assume is available at 298K. A temperature dependence is given in an expression by [115].

$$Z_{\mathrm{rot}}(T) = Z_{\mathrm{rot}}(298) \frac{F(298)}{F(T)} \tag{2.46a}$$

where,

$$F(T) = 1 + \frac{\pi^{3/2}}{2}\left(\frac{\epsilon}{Tk_{\mathrm{B}}}\right)^{\frac{1}{2}} + \left(\frac{\pi^2}{4} + 2\right)\frac{\epsilon}{Tk_{\mathrm{B}}} + \frac{\pi^{3/2}}{2}\left(\frac{\epsilon}{Tk_{\mathrm{B}}}^{\frac{3}{2}}\right) \tag{2.46b}$$

The molar heat capacity C_{v} is different depending on whether the molecule is linear or non-linear or a single atom.

$$\frac{C_{\mathrm{v,trans}}}{R} = \frac{3}{2} \tag{2.47a}$$

$$\frac{C_{\mathrm{v,rot}}}{R} = \begin{cases} 1, & \text{for a linear molecule} \\ \frac{3}{2}, & \text{for a non-linear molecule} \\ 0, & \text{for a monatomic molecule} \end{cases} \tag{2.47b}$$

$$C_{\mathrm{v,vib}} = \begin{cases} C_{\mathrm{v}} - \frac{5}{2}R, & \text{for a linear molecule} \\ C_{\mathrm{v}-3R,} & \text{for a non-linear molecule} \\ 0, & \text{for a monatomic molecule} \end{cases} \tag{2.47c}$$

An averaging combination formula based on mole fractions of species, is given by Mathur et al. [116], for the mixture-averaged thermal conductivity

$$\lambda = \frac{1}{2}\left(\sum_k X_k \lambda_k + \frac{1}{\sum_k X_k/\lambda_k}\right) \tag{2.48}$$

Thermal Diffusion Coefficients

The thermal diffusion coefficients are evaluated in this part with regard to multi-component properties, an inexpensive way to estimate the thermal diffusion of light species into mixture. A thermal diffusion ratio Θ_k is defined according to the thermal diffusion velocity $\mathbf{U_k^T}$, which is given related to the relative temperature gradient in the spatial coordinate and the mixture diffusion coefficient 2.43

$$U_{k,i}^{\mathrm{T}} = -\frac{D_k^{\mathrm{m}}\Theta_k}{X_k}\frac{\partial T}{T\partial x_i} \tag{2.49}$$

where the thermal diffusion ratio Θ_k is given by

$$\Theta_k = \sum_{j\neq k}\theta_{kj} \tag{2.50}$$

and

$$\theta_{kj} = \frac{15}{2} \frac{\left(A^*_{kj} + 5\right)\left(6C^*_{kj} - 5\right)}{A^*_{kj}\left(16A^*_{kj} - 12B^*_{kj} + 55\right)} \frac{W_k - W_j}{W_k + W_j} X_k X_j \tag{2.51}$$

Three ratios of collision integrals are defined by

$$A^*_{ij} = \frac{1}{2} \frac{\Omega^*_{(2,2)}}{\Omega^*_{(1,1)}} \tag{2.52}$$

$$B^*_{ij} = \frac{1}{3} \frac{5\Omega^*_{(1,2)} - \Omega^*_{(1,3)}}{\Omega^*_{(1,1)}} \tag{2.53}$$

$$C^*_{ij} = \frac{1}{3} \frac{\Omega^*_{(1,2)}}{\Omega^*_{(1,1)}} \tag{2.54}$$

The fitted polynomials A^*_{ij}, B^*_{ij} and C^*_{ij} are given in tables of [111].

The pure species fitting procedure

The properties of pure species are fitted with respect to temperature dependence instead of evaluating the complex expressions for the properties. For the properties of the viscosity, thermal conductivity and binary diffusion, logarithms versus the logarithm of temperature are polynomially fitted with temperature ranging from 200 K to 2750 K.

$$\ln \mu_k = \sum_{n=1}^{N} a_{n,k} (\ln T)^{n-1} \tag{2.55a}$$

$$\ln \lambda_k = \sum_{n=1}^{N} b_{n,k} (\ln T)^{n-1} \tag{2.55b}$$

$$\ln D_{k,j} = \sum_{n=1}^{N} g_{n,kj} (\ln T)^{n-1} \tag{2.55c}$$

The polynominal fit is of third to fifth order (N=4-6) and the fitting errors are within one percent. As the binary thermal diffusion ratios θ_{jk} depend weakly on temperature. Thus a third-order polynominal in temperature, rather than logarithm of temperature, is fitted as

$$\theta_{kj} = \sum_{n=1}^{N} h_{n,k} (T)^{n-1} \tag{2.56}$$

2.3.3 The simplified version for the transport equations

When the local average molecular weight is not varying a lot throughout the reacting flow field, diffusion terms in the transport equations of species and energy can be expressed with mass fraction, rather than mole fraction. Therefore, the convection term and diffusion term in regard to the same scalar can be coexisting in the implementation with an implicit scheme, instead of an additional source term with an explicit scheme, thus improving the computational stability. Meanwhile, the thermal diffusion coefficient $D_k^{\mathrm{T}} \propto \Omega_k$ is also dependent on the difference of species molecular weight according to Eq. 2.51 so that thermophoretic term is also neglected when the local average molecular weight remains an unvarying value. The simplified scalar transport equation is

$$\frac{\partial \rho Y_k}{\partial t} + \frac{\partial}{\partial x_j}\left(\rho u_j Y_k\right) = \frac{\partial}{\partial x_i}\left(\rho D_k^{\mathrm{m}} \frac{\partial Y_k}{\partial x_i}\right) + \dot{\omega}_k \tag{2.57}$$

As well, the effect of molecular weight, thermophoresis and Dufour effect are neglected in the energy equation,

$$\frac{\partial \rho h}{\partial t} + \frac{\partial}{\partial x_j}\left(\rho u_j h\right) = \frac{\partial}{\partial x_j}\left(\rho D \frac{\partial h}{\partial x_j}\right) - \sum_k \frac{\partial}{\partial x_j}\left[\rho (D - D_k) h_k \frac{\partial Y_k}{\partial x_j}\right] \tag{2.58}$$

In the simulation of ethylene diffusion flames (see Chapter 4), the local average molecular weight does not vary much. Therefore, the simplified transport equations 2.57 and 2.58 will be employed in solving the reactive fluid dynamics. While in Chapter 5, in the simulation of diffusion flames with biodiesel fuels, the local average molecular weight varies a lot and equations 2.29 and 2.32 are employed.

Fig.2.4 shows the flow chart of the coupled CFD-PBE program in our in-house code BOFFIN, where Navier-Stokes equation, the mixture fraction equation, the transport equations of species and energy, and the population balance equation are calculated, respectively.

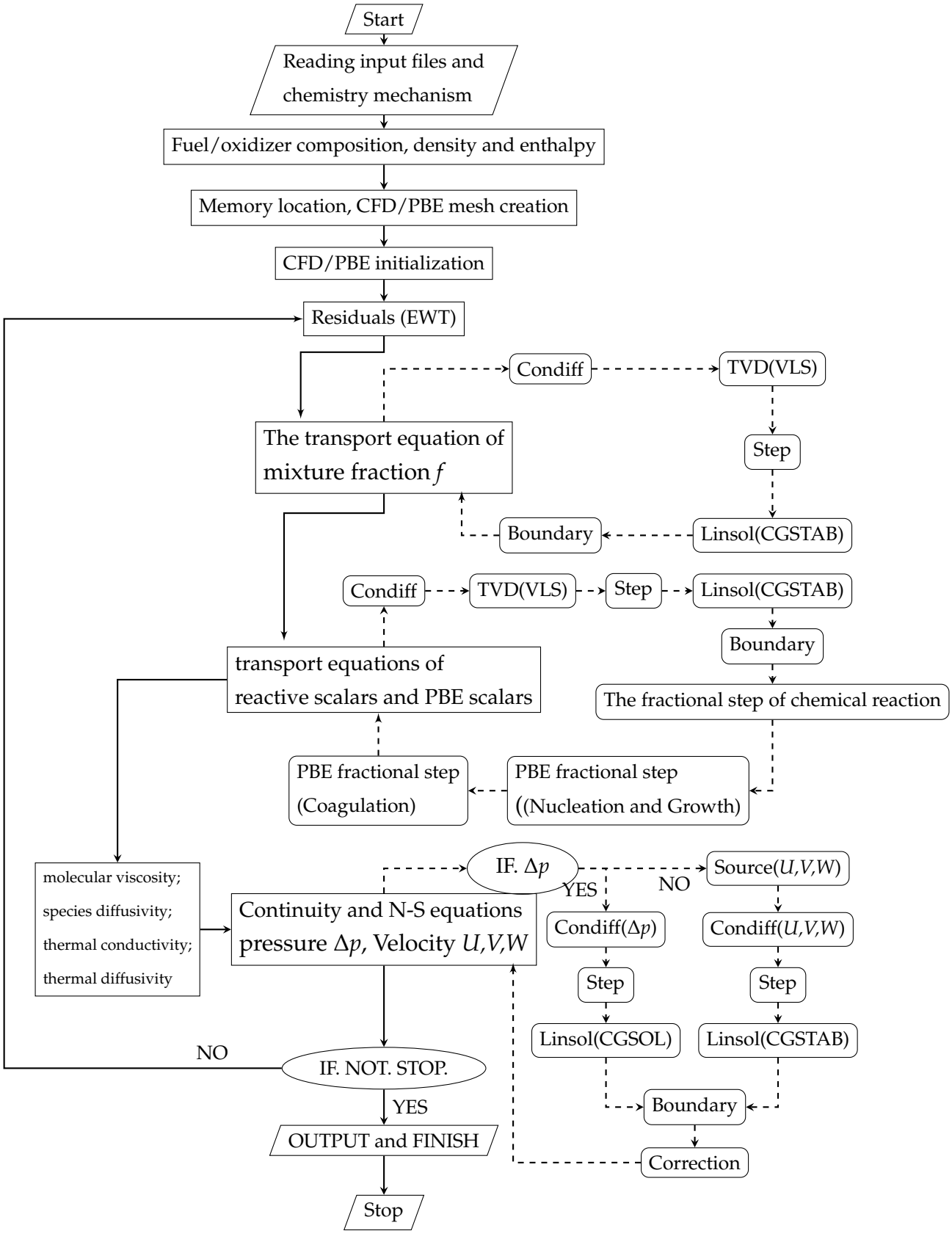

Fig. 2.4 Flow chart for the BOFFIN CFD-PBE code

Chapter 3

A conservative numerical method for the coagulation process in the PBE

The objective of this chapter is to present a novel finite volume method for the discretisation of the population balance equation with coagulation, growth and nucleation that combines: a) accurate prediction of the distribution with a small number of sections, b) conservation of the first moment (or any other single moment) in a coagulation process, c) applicability to an arbitrary non-uniform grid, and d) speed and robustness that make it suitable for combining with a CFD code for solving problems such as soot formation in flames. The conservation of the first moment is of particular importance, because it is an invariant during a coagulation process and represents conservation of mass. The two main concepts of the method are: the detailed evaluation of the double integrals arising from the finite volume discretisation of the coagulation terms via a geometric representation, and the exact balance of coagulation source and sink terms to ensure moment conservation. Extensive testing is performed by comparison with analytical solutions and direct numerical solutions of the discrete PBE for both theoretical and physically important coagulation kernels. Finally, the method is applied to the simulation of a laminar co-flow diffusion sooting flame, in order to assess its potential for coupling with CFD, chemical kinetics, transport and radiation models. The results show that accurate solutions can be obtained with a small number of sections, and that the PBE solution requires less than one fourth of the time of the complete simulation, only half of which is spent on the discretisation (the remaining being for the evaluation of the temperature dependence of the coagulation kernel).

This chapter is organised as follows. An overview of existing discretisation methods for the PBE is presented first, with their inherent defects, in order to put the

new method in context. Subsequently, the equations for the proposed approach are derived, initially for the coagulation PBE and then for nucleation and growth. The method is then tested against analytical solutions or solutions of the discrete PBE for coagulation and coagulation-growth problems. Finally, the application to the laminar flame is presented, which involves coupling with fluid dynamics, chemical kinetics, transport phenomena and radiation.

3.1 Overview of discretisation methods for the PBE

A large number of approaches have been proposed for the discretisation of the PBE. In this paper we will focus on the numerical treatment of coagulation, although the method developed is for combined nucleation, growth and coagulation problems and the discretisation of nucleation and growth will also be briefly discussed. While the derivation of the various methods is based on a range of concepts, the methods can be classified into two general categories:

- Pointwise approximation methods. These methods proceed by postulating a discrete PBE where the number density is concentrated at specific points. This amounts to approximating the number density as a sum of delta functions [80]. The coefficients of this discrete PBE are then derived so as to ensure conservation of one or more moments of the distribution [117]. Therefore, these methods conserve the moments for the accuracy in the prediction of distributions. Unlike moment methods, however, they do not suffer from the closure problem. They can be viewed as bridging the gap between moment and discretisation methods.

- Finite element/volume methods. These methods take the PBE as the starting point, divide the domain of the independent variable into a number of intervals and approximate the number density over each interval via a function (often a constant one). A weighted integral of the equation is then formed, and the residual over each element is minimised according to a certain rule. The finite element method provides the most general mathematical framework for deriving such methods, and the finite volume method can be obtained as a special case. Several methods that belong to this category have not, however, been presented as derived via a finite element procedure. These methods aim at an accurate computation of the number density, but moment conservation

is in general not guaranteed, unless the method is derived in a special way to ensure conservation of a particular moment.

In pointwise approximation methods the distribution is approximated as a set of delta functions, and therefore there is no need to carry out integrations of the kernel and number densities; rather, the coagulation integral terms are approximated as products of the representative particle sizes. For example, the approximation of the source term integral for a bin centred on v_i and of length δv_i can be written as:

$$\int_{v_i-\frac{\delta v_i}{2}}^{v_i+\frac{\delta v_i}{2}} \int_0^v \beta(v-w,w)n(v-w)n(w)dwdv \approx \sum_{\substack{j \\ v_k+v_j=v_i}} \beta_{k,j} n_k n_j \tag{3.1}$$

where the factors $\beta_{k,j}$ include the kernel and any other correction factors required by the approximation scheme. An inherent problem in this approach is that the sum of volumes $v_k + v_j$ will almost never be equal to the representative volume of any other interval unless a uniform grid is employed, so the resultant particle must be allocated to one of the two adjacent points and thus gain or lose volume. To counter this effect, correction factors (incorporated in $\beta_{k,j}$) are introduced so as to conserve one or two moments of the distribution. Methods in this category thus place priority on moment conservation, possibly at the expense of accuracy in the prediction of the distribution.

A number of these methods are based on a grid constructed via a geometric progression, in which several simplifications are possible, particularly for coagulation-only problems. In a grid where $v_i = 2v_{i-1}$, for example, only particles from the previous point can contribute to the coagulation source term, a fact that greatly reduces the number of computations to be carried out. The geometric grid was first proposed by Bleck [118] and further developed by Marchal et al. [119] and Hounslow et al. [120]. The last of these methods conserves both number density and particle volume, but is still limited to a particular geometric grid. The most general and flexible method in this class is that of Kumar and Ramkrishna [121], [122], which solves algebraic equations to compute correction factors that conserve any two moments of the distribution and is not tied to a particular choice of grid.

The source of error in the distribution in pointwise approximation methods is demonstrated graphically in Fig. 3.1, referring to the Kumar and Ramkrishna method [121]. The particles are considered to be concentrated at the discrete points v_j^c, v_k^c, v_{i-1}^c, v_i^c, v_{i+1}^c (which are called *pivots* in the Kumar and Ramkrishna method). As the sum $v_j^c + v_k^c$ does not correspond to any pivot, the particles are allocated to

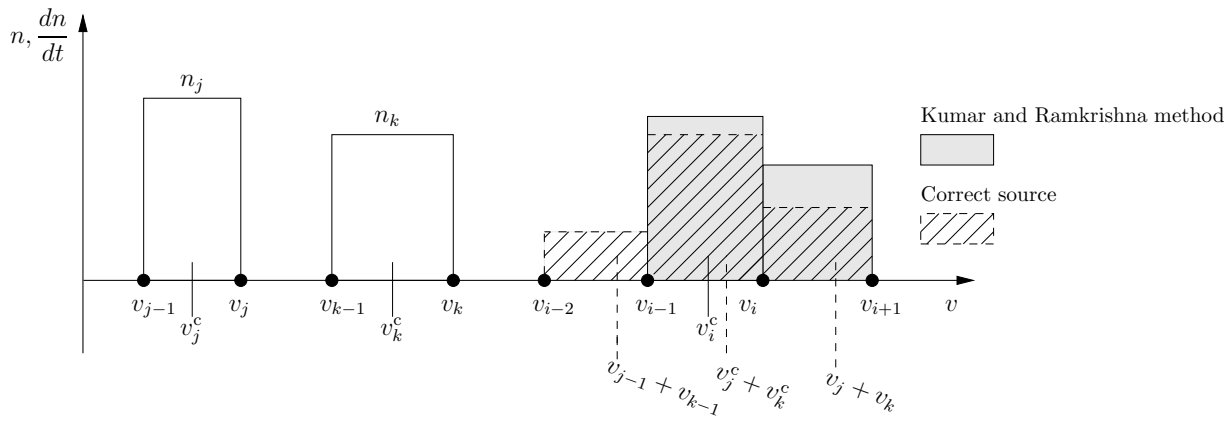

Fig. 3.1 Error of coagulation source in Kumar and Ramkrishna method

two adjacent pivots, such as on v_i^c and v_{i+1}^c because $v_i^c < v_j^c + v_k^c < v_{i+1}^c$ as Fig. 3.1 shows. In this way, the total first moment and change of the zeroth moment are conserved based on interpolation rule. However, from the perspective of the finite volume scheme, the particles are equally distributed in the discretised cells j, k. In fact, if $v_{\min} = v_{j-1} + v_{k-1}$ falls in cell $i-1$, the source of coagulation between the two cells j and k should be partially owed to cell $i-1$. Therefore, in Fig. 3.1, this allocation (grey blocks) by the Kumar and Ramkrishna method introduces an error in the actual source distribution (shadows) , as the correct solution differs in the two cells containing the resulting particles and even spreads to other cells.

Recently, a family of methods has been developed that share features of both moment and discretisation methods and can also be related to the methods discussed above. The Two-Size Moment (TSM) method was developed in the context of sprays [123] and particles [91], while the Multi-Moment Sectional Method (MMSM) [124] was developed in the context of soot. In these methods, the particle size domain is divided to sections and two or more moments are computed in each section, and the distribution is then reconstructed from the moments. Unlike moment methods, where only a few moments are computed, methods in this class require several sections and two or more moments per section, although they offer flexibility with respect to the number of both sections and moments.

A related approach originates in the work of Pope and Howard [125] and is also related to the 'method of classes' developed by Marchal et al. [119] in crystallisation. In this method, the particle size distribution is also discretised into sections, which are then treated as chemical species and added to the reaction mechanism, while the growth and coagulation processes are represented as chemical reactions between

particles in a section and species. One advantage of this approach is that it can be implemented in packages such as CHEMKIN in the same way as a chemical mechanism. This approach was further developed and applied to laminar premixed flames by Richter et al. [126]. However, treating the bins as species means that the particle size distribution must be solved together with the chemical kinetics mechanism, which is often very stiff. By contrast, the solution of the PBE as a separate equation allows the PBE discretisation to be carried out in a separate step via operator splitting.

In the second class of approaches, the distribution is first approximated by trial functions that can be polynomials or constant functions. Gelbard and Seinfeld [127] employed initially cubic splines, but abandoned that approach in favour of constant functions in their subsequent work on the coagulation equation [128] and on multi-component coagulation and growth [98]. While initially developed for aerosols, the method described in [128] was later applied to the modelling of soot formation in laminar premixed and non-premixed flames [129, 130]. Other finite element studies employed collocation and Galerkin methods [131, 132] or collocation with linear trial functions [99], but were not applied to soot. Netzell et al. [133] developed a sectional method for soot modelling that, while not derived via a finite element method, employs a linear variation for the distribution within each bin. This approach was used in a number of soot modelling studies, including [134] for laminar counterflow diffusion flames, [135] for laminar premixed flames, [73] for turbulent non-premixed flames and [136] for RANS simulation of Diesel engines. Finally. the finite volume method has been also used by re-formulating the PBE into a hyperbolic PDE [137, 138], although this approach has not been applied to soot.

The method developed in this work is a finite volume method that can be applied to a PBE combining coagulation, nucleation and growth. The main innovation of the method is in the treatment of the coagulation integral terms, for which a scheme is proposed that a) conserves the first moment (or any other chosen one), and b) is accurate and robust even when a small number of nodes is employed. It is also shown how the proposed scheme can be combined with a TVD scheme for discretisation of the growth term, and how the overall formulation can be coupled with CFD.

3.2 Description of the method

3.2.1 An analysis of the finite volume method applied to coagulation

In the following, we will employ the continuous PBE for a coagulation process as the starting point for the discussion of coagulation schemes, with the $(0,\infty)$ domain will truncated to $(v_0, v_{\max})$, where v_0 is the minimum particle size in the coagulation process:

$$\frac{\partial n(v)}{\partial t} = \frac{1}{2}\int_{v_0}^{v} \beta(v-w,w)n(v-w)n(w)dw - \int_{v_0}^{v_{max}} \beta(v,w)n(v)n(w)dw \tag{3.2}$$

with the initial condition $n(v,t) = n_0(v)$ at $t = 0$.

To proceed with the discretisation, we define a grid in the volume space $(v_0, ..., v_n)$ and denote the intervals as $\Delta v_i = v_i - v_{i-1}$. Since the particle volume typically covers a very wide range in most problems - e.g. for aerosols it can range from 1 nm - 1 μm in diameter, hence nine orders of magnitude in volume - a non-uniform grid must be employed, typically expanding towards increasing volume. While many of the methods developed are tied to a geometric grid, the present method is developed for an arbitrary grid and could also be combined with an adaptive grid, such as the method developed in [102].

To employ the finite volume method, the number density over each interval must first be approximated with a simple function. The zeroth order approximation (constant number density) is employed here, because it will facilitate the analysis and control of the conservation properties of the scheme. It must be noted that this approximation is akin to a histogram, which is the form in which distributions are obtained experimentally. The number density is thus assigned a constant value n_i over each interval Δv_i. Subsequently, Eq. 3.2 is integrated over the interval Δv_i to obtain:

$$\begin{aligned}\frac{dn_i}{dt} = &\frac{1}{\Delta v_i}\int_{v_{i-1}}^{v_i}\left(\int_{v_0}^{\frac{v}{2}} \beta(v-w,w)n(v-w)n(w)dw\right)dv \\ &-\frac{1}{\Delta v_i}\int_{v_{i-1}}^{v_i}\left(\int_{v_0}^{v_{\max}} \beta(v,w)n(w)dw\right)n(v)dv\end{aligned} \tag{3.3}$$

The PBE has now been converted into a system of integro-differential equations describing the temporal evolution of the discretised number density. If the integral

terms can be approximated, it will be possible to integrate the resulting equations with respect to time and obtain $n_i(t)$.

At this point, we are faced with the approximation of two integrations: one over the finite volume interval Δv_i and one over the domain that yields the pair combinations. One approach would be to employ a quadrature rule for the first integration. However, this approach cannot guarantee the conservation of any moment. The error incurred is easiest demonstrated by considering the a two-point quadrature according to the trapezoid rule, although reduced via a more elaborate quadrature rule:

$$\begin{aligned}\left.\frac{dn_i}{dt}\right|_{\text{source}} =& \frac{1}{\Delta v_i}\int_{v_{i-1}}^{v_i}\left(\int_{v_0}^{\frac{v}{2}}\beta(v-w,w)n(v-w)n(w)dw\right)dv \\ \approx& \frac{1}{2}\left(\int_{v_0}^{\frac{v_{i-1}}{2}}\beta(v_{i-1}-w,w)n(v_{i-1}-w)n(w)dw\right. \\ &\left.+\int_{v_0}^{\frac{v_i}{2}}\beta(v_i-w,w)n(v_i-w)n(w)dw\right) \\ =& \frac{1}{2}\left(\left.\frac{dn(v_{i-1})}{dt}\right|_{\text{source}}+\left.\frac{dn(v_i)}{dt}\right|_{\text{source}}\right)\end{aligned} \tag{3.4}$$

However, any quadrature rule replacing the double integrals affects the accuracy of the distribution, due to the fact that at least one integral is evaluated pointwise. The error is illustrated graphically in Fig. 3.2. We consider this specific example: the coagulation process between intervals j, $j+1$ and intervals k, $k+1$, respectively. The length ratio for these four intervals is 3:1:2:1 and number density ratio is 2:3:1:3. The coagulation sinks are determined at each location and donated by four different shaded blocks according to the intervals of daughter particles. The size of shades is dependent on length of intervals and the number densities. We assume all coagulation sources fall inside interval i , where the source term in the interval i is plotted on the positive vertical $\left(\frac{dn}{dt}\right)$ axis, while the corresponding sink terms are plotted on the negative side. Therefore, the discrepancy can be obviously found between the accurate step-distributed source and the approximation by the two-point quadrature,

3.2.2 A conservative finite volume approach for coagulation

In finite volume schemes for fluid dynamics, conservation is ensured because the fluxes from one cell are entering into a neighbouring cell. While conservation alone

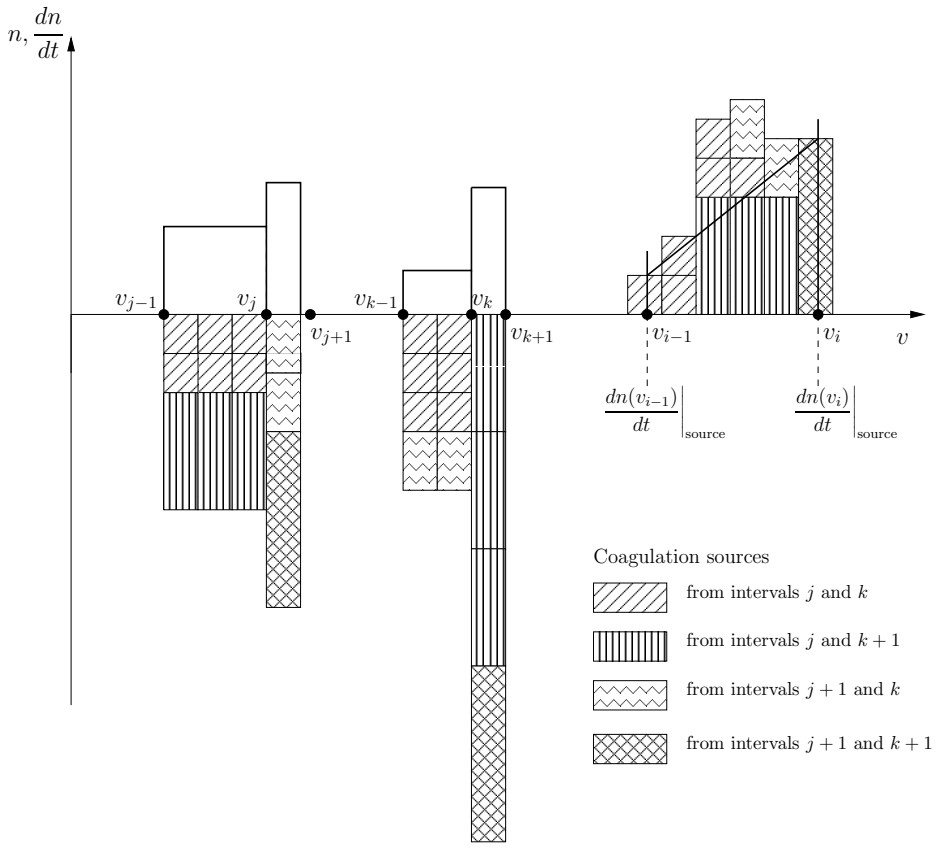

Fig. 3.2 Error in two-point quadrature of the coagulation term

does not guarantee accuracy, it is a highly desired property for a numerical method intended for solution of the fluid dynamics equations and has contributed to the widespread use of finite volume methods in that field. In the PBE, conservation of the first moment of a distribution with respect to volume is important because it is an invariant in a coagulation problem and it represents conservation of mass. However, the application of the finite volume method alone does not guarantee conservation, as has been shown above, because the fluxes into an interval arise from everywhere in the domain, and not just from the adjacent cells.

In order to derive a conservative numerical scheme, in general, it must be ensured that the sources and sinks balance each other. In the case of the PBE, application of this principle means that the particles removed from one interval due to coagulation are being added to another interval, i.e. the shaded areas in Fig. 3.2 correspond to each other. In the following, we will be guided by this principle in order to derive a conservative finite volume discretisation for the coagulation terms in the PBE. The main concept is that only the sink terms will be calculated and subsequently mapped to source terms. This balance principle is also present in other methods, such as the

pointwise approximation methods, but in these methods errors are incurred in the distribution because the particles can only be allocated at grid points (Fig. 3.1). In the proposed method, the various shapes resulting from the variation of the source term within an interval will be considered and a geometric approach to their evaluation will be derived.

We will now proceed to derive a finite volume scheme that is conservative with respect to the first moment. We first multiply Eq. 3.2 by v and integrate over an interval, leading to the following finite volume equation for the balance of the particle volume in interval i. It must be noted that one may multiply by v^m instead and conserve an arbitrary moment of order m; indeed, results for conservation of both the zeroth and first moment will be shown in Sec. 3.3. The equation for the first moment is:

$$\begin{aligned}\frac{d}{dt}\int_{v_{i-1}}^{v_i} vn(v)dv &= \int_{v_{i-1}}^{v_i} v\frac{dn(v)}{dt}dv \\ &= \frac{1}{\Delta v_i}\int_{v_{i-1}}^{v_i}\left(\int_{v_0}^{\frac{v}{2}}\beta(v-w,w)n(v-w)n(w)dw\right)vdv \\ &\quad - \frac{1}{\Delta v_i}\int_{v_{i-1}}^{v_i}\left(\int_{v_0}^{v_{\max}}\beta(v,w)n(w)dw\right)n(v)vdv \end{aligned} \tag{3.5}$$

3.2.3 The main steps of the method

The main steps of the method can now be summarised as follows.

- **Determination of complementary points.** For each interval i denoting the range $[v_{i-1},v_i]$, and for each interval $j(i)$ denoting the range $[w_{j-1}(i),w_j(i)]$ where $w_{j-1} < \frac{v(i)}{2}$ (note that both v and w will be used to represent volume), we locate four points, which will hence be called the *complementary points*, and which correspond to the volumes of particles that would coagulate with particles at the boundaries of j to form particles at the boundaries of i, as follows:

$$\mathrm{U}_{i-1,j} = v_{i-1} - w_j \tag{3.6a}$$
$$\mathrm{U}_{i-1,j-1} = v_{i-1} - w_{j-1} \tag{3.6b}$$
$$\mathrm{U}_{i,j} = v_i - w_j \tag{3.6c}$$
$$\mathrm{U}_{i,j-1} = v_i - w_{j-1} \tag{3.6d}$$

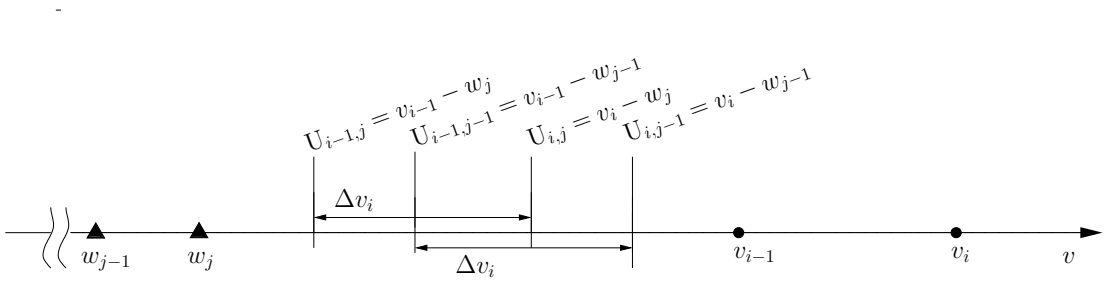

Fig. 3.3 The auxiliary grid of complementary points

The auxiliary grid of complementary points is evaluated at the beginning of the simulation and stored, so no CPU time is spent on this step during the simulation.

- **Evaluation of source and sink terms.** At each time step, the double integrals representing the source of particles in $[v_{i-1}, v_i]$ due to coagulation of particles in $[w_{j-1}, w_j]$ and in the complementary interval and the corresponding sink terms of the parent particles are evaluated geometrically, according to a procedure that will be described in detail in Secs. 3.2.4, 3.2.4. Only the sink terms of the parent particles are calculated, and the source term of the daughter particles are incremented accordingly. This way, the source and sink terms balance and conservation of the first moment is ensured.

- **Temporal integration.** Once all source and sink terms have been collected, a set of ODEs for the number density in each interval is assembled and integrated over a time interval δt to produce the discretised distribution at $t + \delta t$.

3.2.4 Derivation of the discretised equations for coagulation

Before we begin with the derivation of the discretised equations, a partitioning of the intervals is formed separating the intervals up to $\frac{v}{2}$ is formed as follows:

$$\begin{aligned} G_1(i) &= \left\{ [v_1, v_2], \cdots, \left[v_{k-1}(i), \frac{v_{i-1}}{2} \right] \right\} \\ G_2(i) &= \left\{ \left[\frac{v_{i-1}}{2}, v_k(i) \right], ..., \left[v_l(i), \frac{v_i}{2} \right] \right\} \end{aligned} \tag{3.7}$$

where is the maximum nodal volume smaller than $\frac{v_{i-1}}{2}$, v_k is the minimum one greater than $\frac{v_{i-1}}{2}$ and v_l is the maximum one smaller than $\frac{v_i}{2}$. The set $G_1(i)$ thus

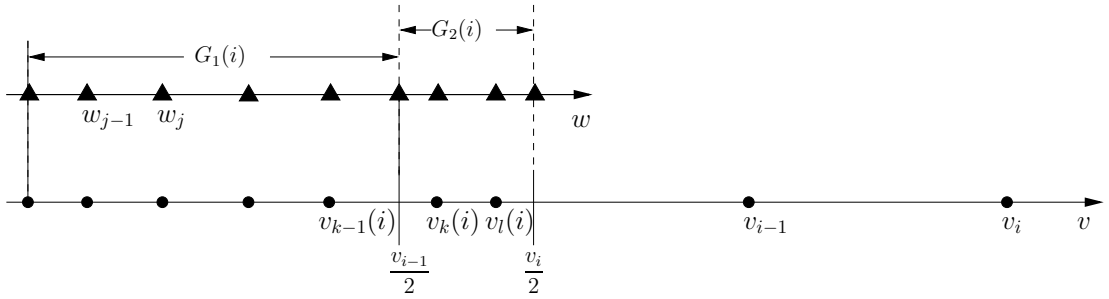

Fig. 3.4 The two groups of intervals $G_1(i)$ and $G_2(i)$

contains all the intervals within $\left[v_0, \frac{v_{i-1}}{2}\right]$, while the set $G_2(i)$ contains all the intervals within $\left[\frac{v_{i-1}}{2}, \frac{v_i}{2}\right]$ (Fig. 3.4). Note that the last interval of $G_1(i)$ and the first and last intervals of $G_2(i)$ are actually fractions of intervals, as they are bounded by the values $\frac{v_{i-1}}{2}$, $\frac{v_i}{2}$ which are not, in general, nodal values. The reason for this classification is because, as we will see, a different treatment is required for the intervals in $G_2(i)$. This feature results from formulating the source term as an integral from 0 to $\frac{v}{2}$, and while it increases the complexity of the discretisation scheme, it reduces the computational time by half.

We will now proceed to show the detailed derivation of the discretised equations. For brevity, we define:

$$C(v,w) = \beta(v,w)n(v)n(w) \tag{3.8}$$

The source term will now be split into two parts, one resulting from coagulation in the intervals in $G_1(i)$ and one from those in $G_2(i)$:

$$\left(\frac{d}{dt}\int_{v_{i-1}}^{v_i} vn(v)dv\right)\Bigg|_{\text{source}} = \int_{v_{i-1}}^{v_i}\left(\int_{v_0}^{\frac{v_{i-1}}{2}} C(v-w,w)dw\right)vdv + \int_{v_{i-1}}^{v_i}\left(\int_{\frac{v_{i-1}}{2}}^{\frac{v}{2}} C(v-w,w)dw\right)vdv \tag{3.9}$$

The inner integrals in Eq. 3.9 can be written as summations over the intervals spanning the ranges $G_1(i)$ and $G_2(i)$:

$$\int_{v_{i-1}}^{v_i}\left(\sum_{G_1(i)}\int_{w_{j-1}}^{w_j} C(v-w,w)dw\right)vdv = \sum_{G_1(i)}\int_{v_{i-1}}^{v_i}\left(\int_{w_{j-1}}^{w_j} C(v-w,w)dw\right)vdv \tag{3.10a}$$

$$= \sum_{j\in G_1(i)} I_{\text{b1}}(i,j)$$

$$\int_{v_{i-1}}^{v_i}\left(\int_{\frac{v_{i-1}}{2}}^{v} C(v-w,w)dw\right)vdv = \int_{\frac{v_{i-1}}{2}}^{\frac{v_i}{2}}\left(\int_{2w}^{v_i} vC(v-w,w)dv\right)dw$$
$$= \sum_{j\in G_2(i)}\int_{w_{j-1}}^{w_j}\left(\int_{2w}^{v_i} vC(v-w,w)dv\right)dw = \sum_{j\in G_2(i)} I_{\mathrm{b}2}(i,j) \quad (3.10b)$$

Therefore the integrals $I_{\mathrm{b}1}(i,j)$ and $I_{\mathrm{b}2}(i,j)$ denote the source, or birth, of particles in interval i belonging to $G_1(i)$ or $G_2(i)$ respectively, arising from coagulation of particles in interval $j(i)$. The calculation of these integrals will be treated in the following two subsections.

Evaluation of source and sink terms for all intervals in $G_1(i)$

In the following, we consider the case $\Delta v_i > \Delta w_j$, so that $\mathrm{U}_{i-1,j-1} < \mathrm{U}_{i,j}$, which corresponds to an expanding grid that would normally be employed in a coagulation problem (although the method can be applied to an arbitrary grid). By introducing a change of variable $u = v - w$, the double integral $I_{\mathrm{b}1}(i,j)$ becomes:

$$\begin{aligned} I_{\mathrm{b}1}(i,j) &= \int_{v_{i-1}-w}^{v_i-w}\left(\int_{w_{j-1}}^{w_j}(u+w)C(u,w)dw\right)du \\ &= \int_{w_{j-1}}^{w_j}\left(\int_{v_{i-1}-w}^{\mathrm{U}_{i-1,j-1}}(u+w)C(u,w)du\right)dw \\ &\quad + \int_{w_{j-1}}^{w_j}\left(\int_{\mathrm{U}_{i-1,j-1}}^{\mathrm{U}_{i,j}}(u+w)C(u,w)du\right)dw \\ &\quad + \int_{w_{j-1}}^{w_j}\left(\int_{\mathrm{U}_{i,j}}^{v_i-w}(u+w)C(u,w)du\right)dw \\ &= \Delta M_{\mathrm{b}}^{\mathrm{left}}(i,j) + \Delta M_{\mathrm{b}}^{\mathrm{middle}}(i,j) + \Delta M_{\mathrm{b}}^{\mathrm{right}}(i,j) \end{aligned} \quad (3.11)$$

where the notation ('left', 'middle' and 'right') corresponds to the shapes in Fig. 3.5.

The source of particles in $[i-1,i]$ results in sink or particles in $[j-1,j]$ and in the whole range of intervals spanned by the complementary points. Therefore there are two contributions to the sink term, which will be denoted $I_{\mathrm{dj}1}$ for the contribution to the sink of particles in $[j-1,j]$ and $I_{\mathrm{dk}1}$ for that in the complementary intervals. These are calculated as follows:

$$\begin{aligned} I_{\mathrm{b}1}(i,j) &= \int_{v_{i-1}-w}^{v_i-w}\left(\int_{w_{j-1}}^{w_j} wC(u,w)du\right)dw + \int_{v_{i-1}-w}^{v_i-w}\left(dw\int_{w_{j-1}}^{w_j} uC(u,w)du\right)dw \\ &= I_{\mathrm{dj}1}(i,j) + I_{\mathrm{dk}1}(i,j) \end{aligned} \quad (3.12)$$

$$= \sum_{\text{loc}} \Delta M^{\text{loc}}_{\text{dj}}(i,j) + \sum_{\text{loc}} \Delta M^{\text{loc}}_{\text{dk}}(i,j) \qquad \text{loc} = (\text{left}, \text{middle}, \text{right})$$

The method now proceeds via a geometric interpretation of the coagulation terms, as shown in Fig. 3.5. The block spanned by the complementary points can be divided into three components: the left part $[\mathrm{U}_{i-1,j}, \mathrm{U}_{i-1,j-1}]$, the middle part $[\mathrm{U}_{i-1,j-1}, \mathrm{U}_{i,j}]$ and the right part $[\mathrm{U}_{i,j}, \mathrm{U}_{i,j-1}]$. In the middle part, each particle can select its coagulation partner from all particles inside the interval j $[w_{j-1}, w_j]$. This is not the case with the other parts, however: e.g. a boundary point, in order for its parent particle to fall into the target cell i $[v_{i-1}, v_i]$, the largest particle size $\mathrm{U}_{i,j-1}$ can only coagulate with the smallest particle w_{j-1} of interval j. The coagulation events thus correspond to three different shaded areas: the 'normal' left triangle 'nlt' (to distinguish from the overlapping triangles, to be defined later), the rectangle 'rec' and the right triangle 'rt'. These terms constitute the integrals $I_{\text{b1}}(i,j)$ and $I_{\text{dj1}}(i,j)$.

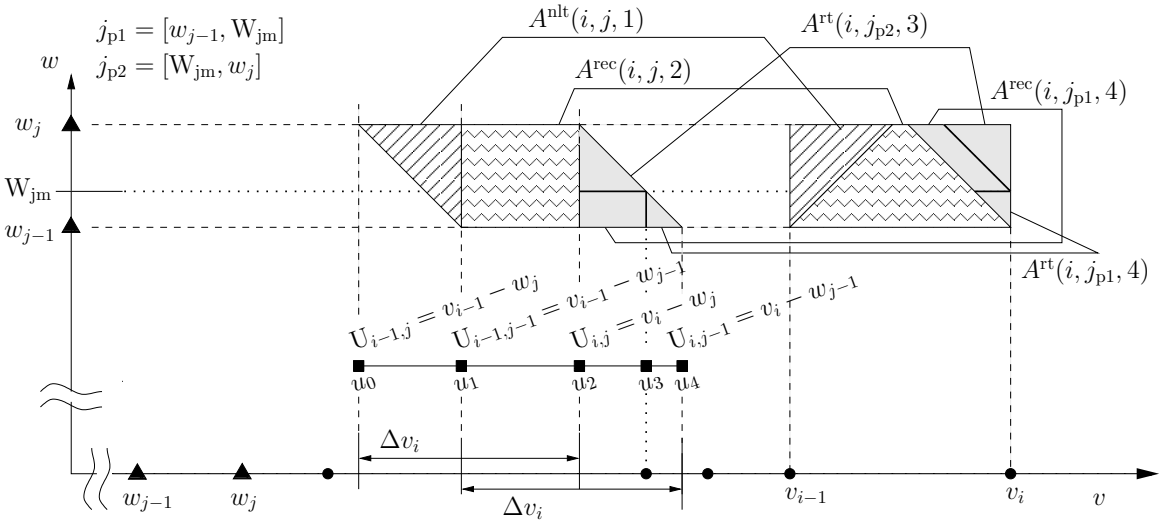

Fig. 3.5 Locations of complementary volumes and number changes for the coagulation of intervals in $G_1(i)$.

To evaluate the integral $I_{\text{dk1}}(i,j)$, we employ the auxiliary grid $[u_{k-1}, u_k]$, $k = 1,2,\cdots,k_{\max}(i,j)$ within the complementary interval. Fig. 3.5 shows a case with $k_{\max}(i,j) = 4$. If the complementary interval spans over more intervals, it will be broken into more shapes that will be evaluated in the same way.

We now formulate the contribution of the coagulation source and sink within the geometric shapes, taking advantage of the fact that the number densities n^u_j and n^w_k are constant for each coagulation pair, $[w_{j-1}, w_j]$ and $[u_{k-1}, u_k]$. For example, let us show in detail how the source and sink terms are evaluated for the case shown in

Fig. 3.5. We first evaluate $I_{\mathrm{dj1}}(i,j)$. The left and middle contributions are calculated as:

$$\begin{aligned}\Delta M_{\mathrm{dj}}^{\mathrm{left}}(i,j) &= \int_{w_{j-1}}^{w_j}\left(\int_{v_{i-1}-w}^{\mathrm{U}_{i-1,j-1}} C(u,w)du\right)wdw \\ &= n_j^w n_1^u \int_{w_{j-1}}^{w_j}\left(\int_{v_{i-1}-w}^{u_1}\beta(u,w)du\right)wdw \end{aligned} \tag{3.13a}$$

$$\begin{aligned}\Delta M_{\mathrm{dj}}^{\mathrm{middle}}(i,j) &= \int_{w_{j-1}}^{w_j}\left(\int_{\mathrm{U}_{i-1,j-1}}^{\mathrm{U}_{i,j}} C(u,w)du\right)wdw \\ &= n_j^w n_1^u \int_{w_{j-1}}^{w_j}\left(\int_{u_1}^{u_2}\beta(u,w)du\right)wdw \end{aligned} \tag{3.13b}$$

At this point, it only remains to evaluate the integrals of the kernel. For maximal accuracy these should be evaluated by multi-point numerical quadrature, but a simpler way is to evaluate them at the centre of weight in each geometrical shape, and our tests show that the accuracy obtained is already very good (Sec. 3.3). This choice is also anticipating the application of the method to spatially-dependent problems such as soot formation: while implementing a multi-point quadrature scheme is straightforward and could be tabulated when the method is applied to the homogeneous PBE, it would incur extra computational cost when coupled with flow in a flame because the temperature dependence of the kernels requires them to be evaluated at every time step. The expressions are as follows:

$$\begin{aligned}\Delta M_{\mathrm{dj}}^{\mathrm{left}}(i,j) &= n_j^w n_1^u \beta^{\mathrm{nlt}} \int_{w_{j-1}}^{w_j}\left(\int_{v_{i-1}-w}^{u_1} du\right)wdw \\ &= n_j^w n_1^u \beta^{\mathrm{nlt}}(i,j,1)\cdot\omega_{\mathrm{dj}}^{\mathrm{nlt}}(i,j,1)\cdot A^{\mathrm{nlt}}(i,j,1) \\ &= \Delta M_{\mathrm{dj}}^{\mathrm{nlt}}(i,j,1) \end{aligned} \tag{3.14a}$$

$$\begin{aligned}\Delta M_{\mathrm{dj}}^{\mathrm{middle}}(i,j) &= n_j^w n_2^u \beta^{\mathrm{rec}} \int_{w_{j-1}}^{w_j}\left(\int_{u_1}^{u_2} du\right)wdw \\ &= n_j^w n_2^u \beta^{\mathrm{rec}}(i,j,2)\cdot\omega_{\mathrm{dj}}^{\mathrm{rec}}(i,j,1)\cdot A^{\mathrm{rec}}(i,j,2) \\ &= \Delta M_{\mathrm{dj}}^{\mathrm{rec}}(i,j,2) \end{aligned} \tag{3.14b}$$

The parameters in Eq. 3.14, namely the evaluated kernel β^{shape}, the weight of centers $\omega_{\text{dj}}^{\text{shape}}$, the integral area A^{shape} and the volume change in corresponding integral area $M_{\text{dj}}^{\text{shape}}$, where shape $=$ nlt(olt),rec,rt, are all functions of interval i, interval $k(i,j)$ and subinterval $j_{\text{p}}(i,j,k)$. These terms are pre-computed and tabulated, and their expressions for all discretised terms are given in Table 3.1. In the same way, we can also obtain the volume change due to the coagulation process between the interval j and the right part of its complementary block. Note that since, in this case, the right part covers different intervals k, a volume point $\text{W}_{\text{jm}} = v_i - u_3$ can be found in Fig. 3.5 and this double integral is composed of several shapes:

$$\begin{aligned}\Delta M_{\text{dj}}^{\text{right}}(i,j) =& n_j^w n_3^u \beta^{\text{rt}}(i,j_{\text{p2}},3)\cdot\omega_{\text{dj}}^{\text{rt}}(i,j_{\text{p2}},3)\cdot A^{\text{rt}}(i,j_{\text{p2}},3)\\ &+ n_j^w n_3^u \beta^{\text{rec}}(i,j_{\text{p1}},3)\cdot\omega_{\text{dj}}^{\text{rec}}(i,j_{\text{p1}},3)\cdot A^{\text{rec}}(i,j_{\text{p1}},3)\\ &+ n_j^w n_4^u \beta^{\text{rt}}(i,j_{\text{p1}},4)\cdot\omega_{\text{dj}}^{\text{rt}}(i,j_{\text{p1}},4)\cdot A^{\text{rt}}(i,j_{\text{p1}},4)\\ &= \Delta M_{\text{dj}}^{\text{rt}}(i,j_{\text{p2}},3)+\Delta M_{\text{dj}}^{\text{rec}}(i,j_{\text{p1}},3)+\Delta M_{\text{dj}}^{\text{rt}}(i,j_{\text{p1}},4)\end{aligned} \tag{3.14c}$$

where j_{p1} and j_{p2} are subintervals of interval j, representing $[w_{j-1},\text{W}_{\text{jm}}]$ and $[\text{W}_{\text{jm}},\text{w}_{\text{j}}]$, respectively. The integral $I_{\text{dj1}}(i,j)$ is finally composed of:

$$\begin{aligned}I_{\text{dj1}}(i,j) =& \Delta M_{\text{dj}}^{\text{nlt}}(i,j,1)+\Delta M_{\text{dj}}^{\text{rec}}(i,j,2)+\Delta M_{\text{dj}}^{\text{rt}}(i,j_{\text{p2}},3)\\ &+\Delta M_{\text{dj}}^{\text{rec}}(i,j_{\text{p1}},3)+\Delta M_{\text{dj}}^{\text{rt}}(i,j_{\text{p1}},4)\end{aligned} \tag{3.15a}$$

Similarly, for $I_{\text{dk1}}(i,j)$:

$$\begin{aligned}I_{\text{dk1}}(i,j) =& \Delta M_{\text{dk}}^{\text{nlt}}(i,j,1)+\Delta M_{\text{dk}}^{\text{rec}}(i,j,2)+\Delta M_{\text{dk}}^{\text{rt}}(i,j_{\text{p2}},3)\\ &+\Delta M_{\text{dk}}^{\text{rec}}(i,j_{\text{p1}},3)+\Delta M_{\text{dk}}^{\text{rt}}(i,j_{\text{p1}},4)\end{aligned} \tag{3.15b}$$

while the source term is equal to the sum of the two sink terms.

Evaluation of source and sink terms for all intervals in $G_2(i)$

We now consider the intervals $j=[w_{j-1},w_j]$ inside group $G_2(i)$, where $j\in\left[\frac{v_{i-1}}{2},\frac{v_i}{2}\right]$. The same strategy is employed to solve the double integrals $I_{b2}(i,j)$. Let $u=v-w>$

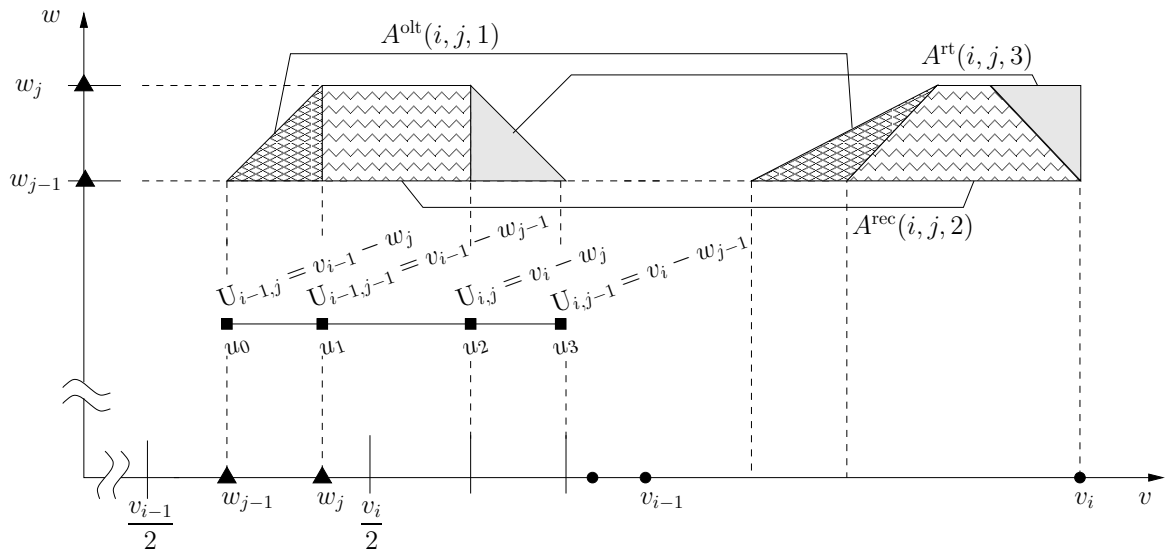

Fig. 3.6 Locations of complementary volumes and number changes for the coagulation of intervals in $G_2(i)$

w:

$$
\begin{aligned}
I_{\mathrm{b2}}(i,j) &= \int_{w_{j-1}}^{w_j} \left(\int_{2w}^{v_i} vC(v-w,w)dv \right) dw \\
&= \int_{w}^{v_i - w} \left(\int_{w_{j-1}}^{w_j} (w+u)C(u,w)dw \right) du \\
&= \int_{w_{j-1}}^{w_j} \left[\int_{w}^{\mathrm{U}_{i-1,j-1}} (w+u)du + \int_{\mathrm{U}_{i-1,j-1}}^{\mathrm{U}_{i,j}} (w+u)du + \int_{\mathrm{U}_{i,j}}^{v_i - w} (w+u)du \right] C(u,w)dw \\
&= \sum_{\mathrm{loc}} \Delta M_{\mathrm{b}}^{\mathrm{loc}}(i,j) \qquad\qquad (\mathrm{loc} = \mathrm{left}, \mathrm{middle}, \mathrm{right}) \\
&= \sum_{\mathrm{loc}} \Delta M_{\mathrm{dj}}^{\mathrm{loc}}(i,j) + \sum_{\mathrm{loc}} \Delta M_{\mathrm{dk}}^{\mathrm{loc}}(i,j)
\end{aligned}
\tag{3.16}
$$

As Fig. 3.6 shows, the left wing $[\mathrm{U}_{i-1,j}, \mathrm{U}_{i-1,j-1}]$ completely belongs to interval j and the daughter particle size $w \in [w_{j-1}, w_j]$ can coagulate with any larger complementary daughter particle inside $[w, w_j]$. Therefore, we name the integral shape for the left part 'overlapping left triangle' (olt) and all pertinent parameters are displayed in Table 3.1.

$$
\Delta M_{\mathrm{dj}}^{\mathrm{left}} = \Delta M_{\mathrm{dj}}^{\mathrm{olt}}(i,j,1) = n_j^w n_1^u C^{\mathrm{olt}}(i,j,1) \omega_{\mathrm{dj}}^{\mathrm{olt}}(i,j,1) A^{\mathrm{olt}}(i,j,1) \tag{3.17}
$$

3.2.5 Final assembly of terms

Once the source term for all intervals has been calculated, the sink term will also have been assembled. The discretisation has thus resulted in the following set of ODEs:

$$\begin{aligned}\frac{dn_i}{dt} &= \frac{1}{\Delta v_i \bar{v}_i}\frac{d}{dt}\int_{v_{i-1}}^{v_i} n(v)v dv \\ &= \frac{1}{\Delta v_i \bar{v}_i}\left[\left(\frac{d}{dt}\int_{v_{i-1}}^{v_i} n(v)v dv\right)\Bigg|_{\text{source}} - \left(\frac{d}{dt}\int_{v_{i-1}}^{v_i} n(v)v dv\right)\Bigg|_{\text{sink}}\right]\end{aligned} \tag{3.18}$$

where $\bar{v}_i$ is the centre of interval i, and

$$\left(\frac{d}{dt}\int_{v_{i-1}}^{v_i} n(v)v dv\right)\Bigg|_{\text{source}} = \sum_{j\in G_1(i)+G_2(i)}\sum_{\text{loc}}\left[\Delta M_{\text{b}}^{\text{loc}}(i,j)\right] \qquad (\text{loc} = \text{left}, \text{middle}, \text{right}) \tag{3.19}$$

and

$$\left(\frac{d}{dt}\int_{v_{i-1}}^{v_i} n(v)v dv\right)\Bigg|_{\text{sink}} = \sum_{p=i}^{i_{\max}}\left[\sum_{j\in[v_{i-1},v_i]}\sum_{\text{loc}}\Delta M_{\text{dj}}^{\text{loc}}(p,j) + \sum_{k\in[v_{i-1},v_i]}\sum_{\text{shape}}\Delta M_{\text{dk}}^{\text{shape}}(p,j_{\text{p}},k)\right] \tag{3.20}$$
$$(\text{loc} = \text{left}, \text{middle}, \text{right}, \quad \text{shape} = \text{nlt}(\text{olt}), \text{rec}, \text{rt})$$

It must be noted that the determination of the auxiliary grid, geometric factors and volumetric dependence of the kernel are all carried out only once, at the beginning of the simulation, and stored for subsequent use. The operations to be carried out at each time step therefore include only computing products of number densities and updating the kernels for dependence on ambient conditions such as temperature, if needed. This pre-computation greatly enhances the computational efficiency of the method.

3.3 Testing and validation of the method

3.3.1 Coagulation kernels

In this section, the method will be tested with a number of canonical problems for the PBE. These include problems with coagulation alone involving various coagulation

Table 3.1 Parameters of four basic geometric shapes in double integral method

Shape		$\Delta M_m(i,j_\mathrm{p},k)$	A	$\Delta N(i,j_\mathrm{p},k)$	$\Delta M(i,j_\mathrm{p},k)$	Weight centres ω	C
Right triangles ('rt')	j	$\Delta M^{\mathrm{rt}}_{m,\mathrm{dj}} = C^{\mathrm{rt}}\left[\frac{{w_{\mathrm{jr}}}^{m+2} - {w_{\mathrm{jl}}}^{m+2}}{(m+1)(m+2)} - \frac{h\cdot {w_{\mathrm{jl}}}^{m+1}}{m+1}\right]$	$A^{\mathrm{rt}} = \frac{1}{2}h^2$	$\left\|\Delta N^{\mathrm{rt}}_{\mathrm{dj}}\right\|$	$\Delta M^{\mathrm{rt}}_{\mathrm{dj}} = \omega^{\mathrm{rt}}_{\mathrm{dj}}\Delta N^{\mathrm{rt}}_{\mathrm{dj}}$	$\omega^{\mathrm{rt}}_{\mathrm{dj}} = w_{\mathrm{jl}} + \frac{1}{3}h$	$C^{\mathrm{rt}} = n_j^w n_k^u \beta\left(\omega^{\mathrm{rt}}_{\mathrm{dj}}, \omega^{\mathrm{rt}}_{\mathrm{dk}}\right)$
	k	$\Delta M^{\mathrm{rt}}_{m,\mathrm{dk}} = \frac{h_j\cdot C^{\mathrm{rt}}}{m+1}({u_k}^{m+1} - {u_{k-1}}^{m+1})$		$\left\|\Delta N^{\mathrm{rt}}_{\mathrm{dk}}\right\| = A^{\mathrm{rt}}C^{\mathrm{rt}}$	$\Delta M^{\mathrm{rt}}_{\mathrm{dk}} = \omega^{\mathrm{rt}}_{\mathrm{dk}}\Delta N^{\mathrm{rt}}_{\mathrm{dk}}$	$\omega^{\mathrm{rt}}_{\mathrm{dk}} = u_k - \frac{2}{3}h$	
	i	$\Delta M^{\mathrm{rt}}_{m,\mathrm{b}} = C^{\mathrm{rt}}\left[\frac{(v_{\mathrm{jl}}+v_{\mathrm{kl}})^{m+2} - (v_{\mathrm{jl}}+v_{\mathrm{kr}})^{m+2}}{(m+1)(m+2)} + \frac{h\cdot(v_{\mathrm{jl}}+v_{\mathrm{kr}})^{m+1}}{m+1}\right]$		$\Delta N^{\mathrm{rt}}_{\mathrm{b}}$	$\Delta M^{\mathrm{rt}}_{\mathrm{b}} = \omega^{\mathrm{rt}}_{\mathrm{b}}\Delta N^{\mathrm{rt}}_{\mathrm{b}}$	$\omega^{\mathrm{rt}}_{\mathrm{b}} = \omega^{\mathrm{rt}}_{\mathrm{dj}} + \omega^{\mathrm{rt}}_{\mathrm{dk}}$	
Rectangles ('rec')	j	$\Delta M^{\mathrm{rec}}_{m,\mathrm{dj}} = \frac{h_k\cdot C^{\mathrm{rec}}}{m+1}({w_{\mathrm{jr}}}^{m+1} - {w_{\mathrm{jl}}}^{m+1})$	$A^{\mathrm{rec}} = h\cdot h_k$	$\left\|\Delta N^{\mathrm{rec}}_{\mathrm{dj}}\right\|$	$\Delta M^{\mathrm{rec}}_{\mathrm{dj}} = \omega^{\mathrm{rec}}_{\mathrm{dj}}\Delta N^{\mathrm{rec}}_{\mathrm{dj}}$	$\omega^{\mathrm{rec}}_{\mathrm{dj}} = w_{\mathrm{jl}} + \frac{1}{2}h$	$C^{\mathrm{rec}} = n_j^w n_k^u \beta(\omega^{\mathrm{rec}}_{\mathrm{dj}}, \omega^{\mathrm{rec}}_{\mathrm{dk}})$
	k	$\Delta M^{\mathrm{rec}}_{m,\mathrm{dk}} = \frac{h\cdot C^{\mathrm{rec}}}{m+1}({u_k}^{m+1} - {u_{k-1}}^{m+1})$		$\left\|\Delta N^{\mathrm{rec}}_{\mathrm{dk}}\right\| = A^{\mathrm{rec}}C^{\mathrm{rec}}$	$\Delta M^{\mathrm{rec}}_{\mathrm{dk}} = \omega^{\mathrm{rec}}_{\mathrm{dk}}\Delta N^{\mathrm{rec}}_{\mathrm{dk}}$	$\omega^{\mathrm{rec}}_{\mathrm{dk}} = u_k - \frac{1}{2}h_k$	
	i	$\Delta M^{\mathrm{rec}}_{m,\mathrm{b}} = \frac{C^{\mathrm{rec}}}{(m+1)(m+2)}\left[(w_{\mathrm{jr}}+u_k)^{m+1} - (w_{\mathrm{jr}}+u_{k-1})^{m+1} - (w_{\mathrm{jl}}+u_k)^{m+1} + (w_{\mathrm{jl}}+u_{k-1})^{m+1}\right]$		$\Delta N^{\mathrm{rec}}_{\mathrm{b}}$	$\Delta M^{\mathrm{rec}}_{\mathrm{b}} = \omega^{\mathrm{rec}}_{\mathrm{b}}\Delta N^{\mathrm{rec}}_{\mathrm{b}}$	$\omega^{\mathrm{rec}}_{\mathrm{b}} = \omega^{\mathrm{rec}}_{\mathrm{dj}} + \omega^{\mathrm{rec}}_{\mathrm{dk}}$	
Normal left triangles ('nlt')	j	$\Delta M^{\mathrm{nlt}}_{m,\mathrm{dj}} = C^{\mathrm{nlt}}\left[\frac{{u_{\mathrm{jl}}}^{m+2} - u_{\mathrm{jl}}{u_{\mathrm{jr}}}^{m+1}}{(m+1)(m+2)} + \frac{h\cdot {u_{\mathrm{jr}}}^{m+1}}{m+2}\right]$	$A^{\mathrm{nlt}} = \frac{1}{2}h^2$	$\left\|\Delta N^{\mathrm{nlt}}_{\mathrm{dj}}\right\|$	$\Delta M^{\mathrm{nlt}}_{\mathrm{dj}} = \omega^{\mathrm{nlt}}_{\mathrm{dj}}\Delta N^{\mathrm{nlt}}_{\mathrm{dj}}$	$\omega^{\mathrm{nlt}}_{\mathrm{dj}} = w_{\mathrm{jr}} - \frac{1}{3}h$	$C^{\mathrm{nlt}} = n_j^w n_k^u \cdot \beta(\omega^{\mathrm{nlt}}_{\mathrm{dj}}, \omega^{\mathrm{nlt}}_{\mathrm{dk}})$
	k	$\Delta M^{\mathrm{nlt}}_{m,\mathrm{dk}} = C^{\mathrm{nlt}}\left[\frac{h\cdot {u_k}^{m+1}}{m+1} - \frac{{u_k}^{m+2} - {u_{k-1}}^{m+2}}{(m+1)(m+2)}\right]$		$\left\|\Delta N^{\mathrm{nlt}}_{\mathrm{dk}}\right\| = A^{\mathrm{nlt}}C^{\mathrm{nlt}}$	$\Delta M^{\mathrm{nlt}}_{\mathrm{dk}} = \omega^{\mathrm{nlt}}_{\mathrm{dk}}\Delta N^{\mathrm{nlt}}_{\mathrm{dk}}$	$\omega^{\mathrm{nlt}}_{\mathrm{dk}} = u_k - \frac{1}{3}h$	
	i	$\Delta M^{\mathrm{nlt}}_{m,\mathrm{b}} = C^{\mathrm{nlt}}\left[\frac{(w_{\mathrm{jr}}+u_k)^{m+2} - (w_{\mathrm{jl}}+u_k)^{m+2}}{(m+1)(m+2)} + \frac{h\cdot(w_{\mathrm{jl}}+u_k)^{m+1}}{m+2}\right]$		$\Delta N^{\mathrm{nlt}}_{\mathrm{b}}$	$\Delta M^{\mathrm{nlt}}_{\mathrm{b}} = \omega^{\mathrm{nlt}}_{\mathrm{b}}\Delta N^{\mathrm{nlt}}_{\mathrm{b}}$	$\omega^{\mathrm{nlt}}_{\mathrm{b}} = \omega^{\mathrm{nlt}}_{\mathrm{dj}} + \omega^{\mathrm{nlt}}_{\mathrm{dk}}$	
Overlapping left triangles ('olt')	j	$\Delta M^{\mathrm{olt}}_{\mathrm{dj}} = C^{\mathrm{olt}}\left[\frac{{w_{\mathrm{jr}}}^{m+2} - {w_{\mathrm{jl}}}^{m+2}}{(m+1)(m+2)} - \frac{h{w_{\mathrm{jl}}}^{m+1}}{m+1}\right]$	$A^{\mathrm{olt}} = \frac{1}{2}h^2$	$\left\|\Delta N^{\mathrm{olt}}_{\mathrm{dj}}\right\|$	$\Delta M^{\mathrm{olt}}_{\mathrm{dj}} = \omega^{\mathrm{olt}}_{\mathrm{dj}}\Delta N^{\mathrm{olt}}_{\mathrm{dk}}$	$\omega^{\mathrm{olt}}_{\mathrm{dj}} = w_{\mathrm{jl}} + \frac{1}{3}h$	$C^{\mathrm{olt}} = (n_j^w)^2 \cdot \beta\left(\omega^{\mathrm{olt}}_{\mathrm{dj}}, \omega^{\mathrm{olt}}_{\mathrm{dk}}\right)$
	k	$\Delta M^{\mathrm{olt}}_{\mathrm{dk}} = C^{\mathrm{olt}}\left[\frac{h{u_k}^{m+1}}{m+1} - \frac{{u_k}^{m+2} - {u_{k-1}}^{m+2}}{(m+1)(m+2)}\right]$		$\left\|\Delta N^{\mathrm{olt}}_{\mathrm{dk}}\right\| = A^{\mathrm{olt}}C^{\mathrm{olt}}$	$\Delta M^{\mathrm{olt}}_{\mathrm{dk}} = \omega^{\mathrm{olt}}_{\mathrm{dk}}\Delta N^{\mathrm{olt}}_{\mathrm{dk}}$	$\omega^{\mathrm{olt}}_{\mathrm{dk}} = u_k - \frac{1}{3}h$	
	i	$\Delta M^{\mathrm{olt}}_{m,\mathrm{b}} = \frac{C^{\mathrm{olt}}}{(m+1)(m+2)}\left[(2w_{\mathrm{jr}})^{m+2} - 2(w_{\mathrm{jl}}+w_{\mathrm{jr}})^{m+2} + (2w_{\mathrm{jl}})^{m+2}\right]$		$\Delta N^{\mathrm{olt}}_{\mathrm{b}}$	$\Delta M^{\mathrm{olt}}_{\mathrm{b}} = \omega^{\mathrm{olt}}_{\mathrm{b}}\Delta N^{\mathrm{olt}}_{\mathrm{b}}$	$\omega^{\mathrm{olt}}_{\mathrm{b}} = \omega^{\mathrm{olt}}_{\mathrm{dj}} + \omega^{\mathrm{olt}}_{\mathrm{dk}}$	

Notes: $j_\mathrm{p} = [w_{\mathrm{jl}}, w_{\mathrm{jr}}] \in j = [w_{j-1}, w_j]$ $\quad h = w_{\mathrm{jr}} - w_{\mathrm{jl}}$; $k = [u_{k-1} - u_k]$ $\quad h_k = u_k - u_{k-1}$

kernels and initial distributions, as well as a problem of combined coagulation and growth.

The first class of kernels to be tested includes kernels of theoretical importance, due to the fact that they permit analytical solutions of the continuous PBE for coagulation (Eq. 3.2). These are:

- The constant kernel:
$$\beta(v,w) = \beta_0 \tag{3.21}$$
- The sum kernel:
$$\beta(v,w) = \beta_0(v+w) \tag{3.22}$$
- The product kernel:
$$\beta(v,w) = \beta_0 vw \tag{3.23}$$

The second class includes physically important kernels. As there is no analytical solution for those comparison will be made with direct numerical solutions of the discrete PBE, as will be described in Sec. 3.3.2. These kernels include:

- The Brownian motion kernel, which governs coagulation of small aerosols:
$$\beta(v,w) = \beta_0 \left(\frac{1}{v^{\frac{1}{3}}} + \frac{1}{w^{\frac{1}{3}}} \right) \left(v^{\frac{1}{3}} + w^{\frac{1}{3}} \right) \tag{3.24}$$
- The kernel due to collisions of particles in the free molecule regime:
$$\beta(v,w) = \beta(v,w) = \beta_0 \left(\frac{1}{v} + \frac{1}{w} \right)^{\frac{1}{2}} \left(v^{\frac{1}{3}} + w^{\frac{1}{3}} \right)^2 \tag{3.25}$$
- The shear kernel, important for coagulation due to laminar shear or turbulent coagulation:
$$\beta(v,w) = \beta_0 \left(v^{\frac{1}{3}} + w^{\frac{1}{3}} \right)^3 \tag{3.26}$$

Note that, for the physical kernels, the factor β_0 is a function of ambient conditions and hydrodynamic parameters, such as temperature, shear and energy dissipation rate. In the present section, this factor will be set equal to unity, as the focus on testing the method with respect to the volumetric dependence of the kernels. In Sec. 4.1, where the method will be applied to the simulation of a laminar flame, the full form of the kernels will be employed.

3.3.2 Direct numerical solution of the discrete PBE

Analytical solutions are available only for a few cases, mainly for the theoretical kernels. To extend the range of test cases to the physically important kernels, comparisons will be made also with direct numerical solutions of the discrete PBE for coagulation, also known as the Smoluchowski equation [82]:

$$\frac{dN_i}{dt} = \frac{1}{2}\sum_{j=1}^{i-1}\beta_{j,i-j}N_jN_{i-j} - N_i\sum_{j=1}^{\infty}\beta_{ij}N_j \tag{3.27}$$

where N_i is the number density and β_{ij} is the coagulation kernel. The discrete PBE is a closed set of ODEs and can be solved numerically with no approximations other than the error involved in the temporal integration. However, one has to solve for all possible particle sizes, resulting in an extremely large set of ODEs, which makes the solution not useful for purposes other than as benchmark for numerical methods. In our test cases, 5000 to 10000 discrete sizes were used, while the temporal integration was carried out with the same method as for the conservative finite volume method (Runge-Kutta 4th order).

For the monodisperse distribution, however, the correspondence between the discrete and continuous PBE is not exact for the first few sizes (0.1-1 in the test cases). A monodisperse distribution in the discrete formulation would correspond to a delta function in the continuous one, but this is not possible to implement; instead one has to distribute the particles over an interval and ensure that the number of particles is consistent. This results in a discrepancy of the two solutions at the initial range, which is of no relevance for the accuracy of the numerical method; a meaningful comparison can be made after size 1.

3.3.3 Initial distributions and parameters

Two types of the initial distribution will be tested. The first is an exponential initial distribution:

$$n(v,0) = \frac{N_0}{v_0}\mathrm{e}^{-\frac{v}{v_0}} \tag{3.28}$$

where N_0 is the total number of particles and v_0 is the mean volume in the initial distribution. For simplicity, we set $N_0 = 1$, $v_0 = 1$ on our test cases. there The second

Initial distribution	Kernel $\beta(w,v)$	Size range	Grid number		Time step (s)
			Proposed method	Discrete method	
Exponential $n(v,0) = \frac{N_0}{v_0} e^{v/v_0}$	constant	0.1-1000	30	analytical solution	0.01
	sum				
	product				
	free-molecular motion			5000	
	Brownian motion				
	shear				
Monodisperse $n(v,0) = \begin{cases} 1, v \in (0.1,0.5) \\ 0, \text{otherwise} \end{cases}$	constant	0.1-400	30	10000	0.01
	sum				
	product				
	free-molecular motion				
	Brownian motion				
	shear				

Table 3.2 Parameters for the coagulation test cases

is a monodisperse distribution:

$$n(v,0) = \begin{cases} 1, v \in (0.1,0.5) \\ 0, \text{otherwise} \end{cases}$$

The factor β_0 is set to unity for all kernels. The grid employed is exponential in all cases. The remaining parameters are shown in Table 3.2.

3.3.4 Convergence study

A convergence test has been conducted to determine the minimum number of grid points required for the test cases, employing the sum and free molecule regime kernels and an exponential initial distribution with grids including 30, 40 and 60 nodes (Fig. 3.7). Converged results can be accomplished with 30 nodes, and therefore this grid was employed in the subsequent tests.

3.3.5 Exponential initial distribution

Analytical solutions of the coagulation equation have been derived for the constant, sum and product kernels with the exponential initial distribution [139, 140]. Results are shown in Fig. 3.8 for several time steps. For all cases, the proposed method exhibits excellent accuracy. The method can also be adapted to conserve a moment of an arbitrary order, and results are also shown for the conservation of the zeroth and second moment. Best results are obtained with the conservation of the first

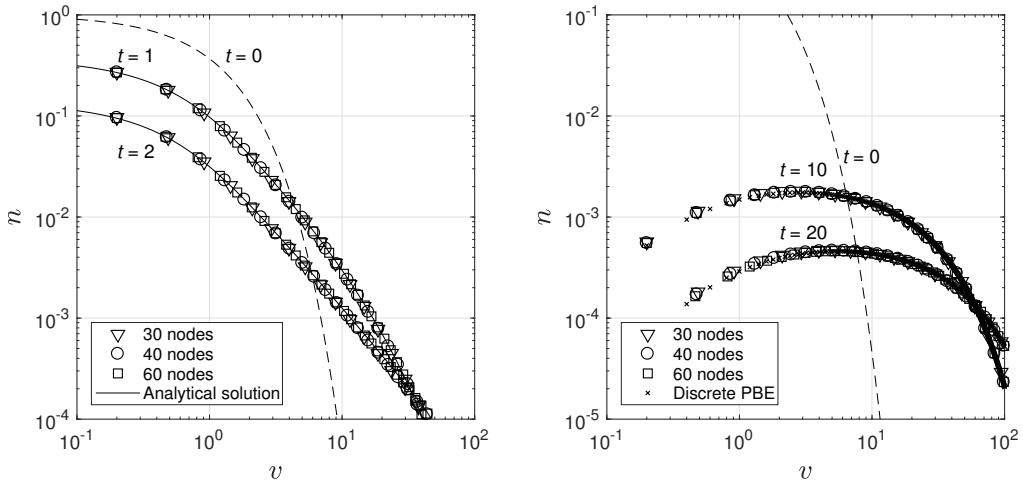

(a) Sum kernel (b) Free molecule regime kernel

Fig. 3.7 Grid convergence test for the coagulation process with an exponential initial distribution

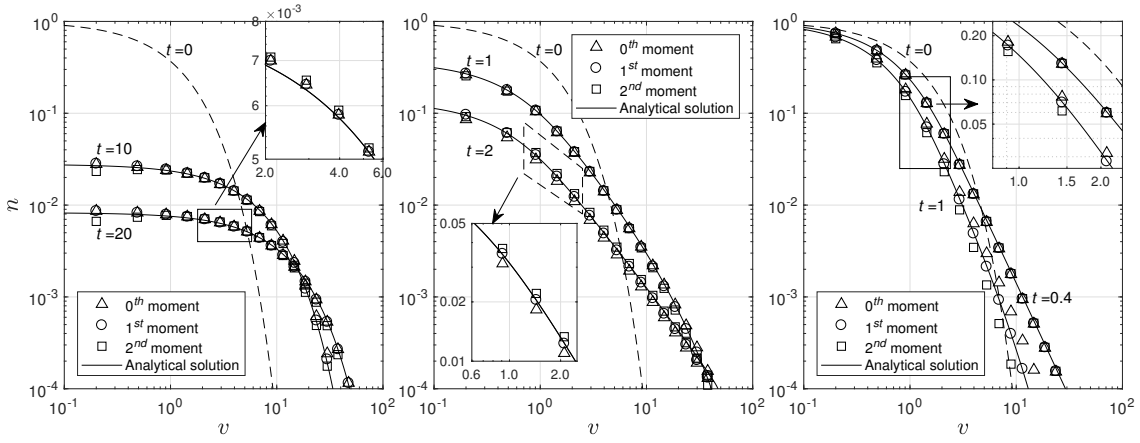

(a) constant kernel (b) sum kernel (c) product kernel

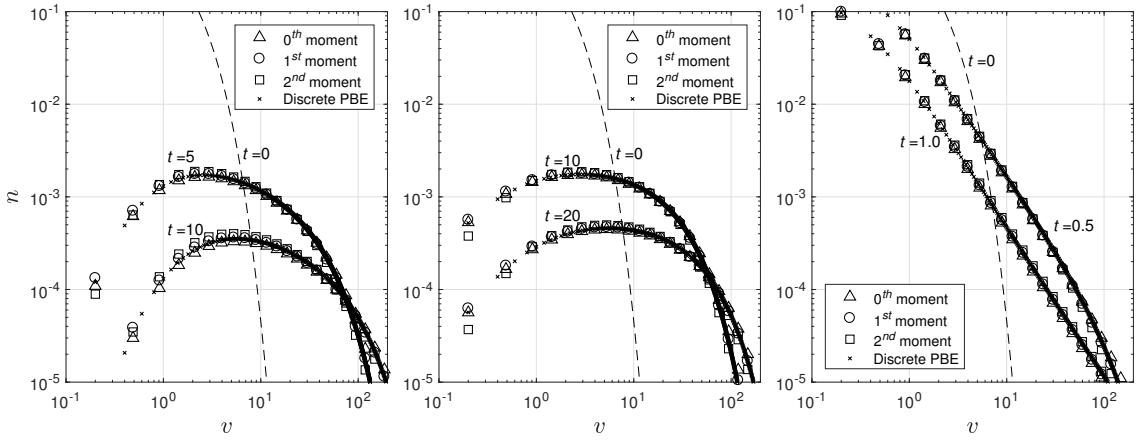

(d) Brownian kernel (e) free-molecular kernel (f) shear kernel

Fig. 3.8 Coagulation process with an exponential initial distribution

moment, although generally all of them are very accurate. The difference is more evident for $v > 10$, where the first moment-based solution is still very accurate, while the others exhibit slight deviations.

3.3.6 Monodisperse initial distribution

The method will now be tested for a coagulation process with a monodisperse initial distribution, with the same selection of kernels. This case is more more physically relevant, as it corresponds to the coagulation of an initially monodisperse population, which is encountered in many real processes. Comparison will be made with solutions of the discrete PBE. Figure 3.9 displays logarithmic plots of the distribution. As explained in Sec. 3.3.2, the implementation of the monodisperse initial distribution is not fully consistent in the two formulations and the comparison is meaningful above size 1. In general, the proposed method conserving the first moment performs very well. Some small deviations appear when the method is set up to conserve the zeroth or the second moment (Fig. 3.9).

3.3.7 Combined coagulation and growth with an exponential initial distribution

This case was studied by Ramabhadran et al. [141], who derived an analytical solution for the constant and sum coagulation kernels and a linear size-dependent growth term ($G = k_g v$), with an exponential initial distribution. In the discretised PBE, the growth term are treated with a total variation diminishing (TVD) method, as described in Sec 2.2.2. Fig. 3.10 shows the numerical results by the proposed method with 30 nodes of the PBE grid and the analytical solution ($k_g = 0.1$). The comparison with the analytical solution is again very good.

3.3.8 Comparison with Kumar and Ramkrishna method

In this section, the performance in the aspects of economy, accuracy and adaptivity of the proposed method is compared against with existing methods. Kumar and Ramkrishna method [121, 122] serves as one of the most practically used methods in solving the PBE for the aerosol dynamic [142], including soot formation [143].

First of all, the time expense for both methods is estimated by counting the number of operations in each time step, shown in Table 3.3. Two different sets of exponential grid, with 30 and 60 grid nodes, respectively have been tested for both

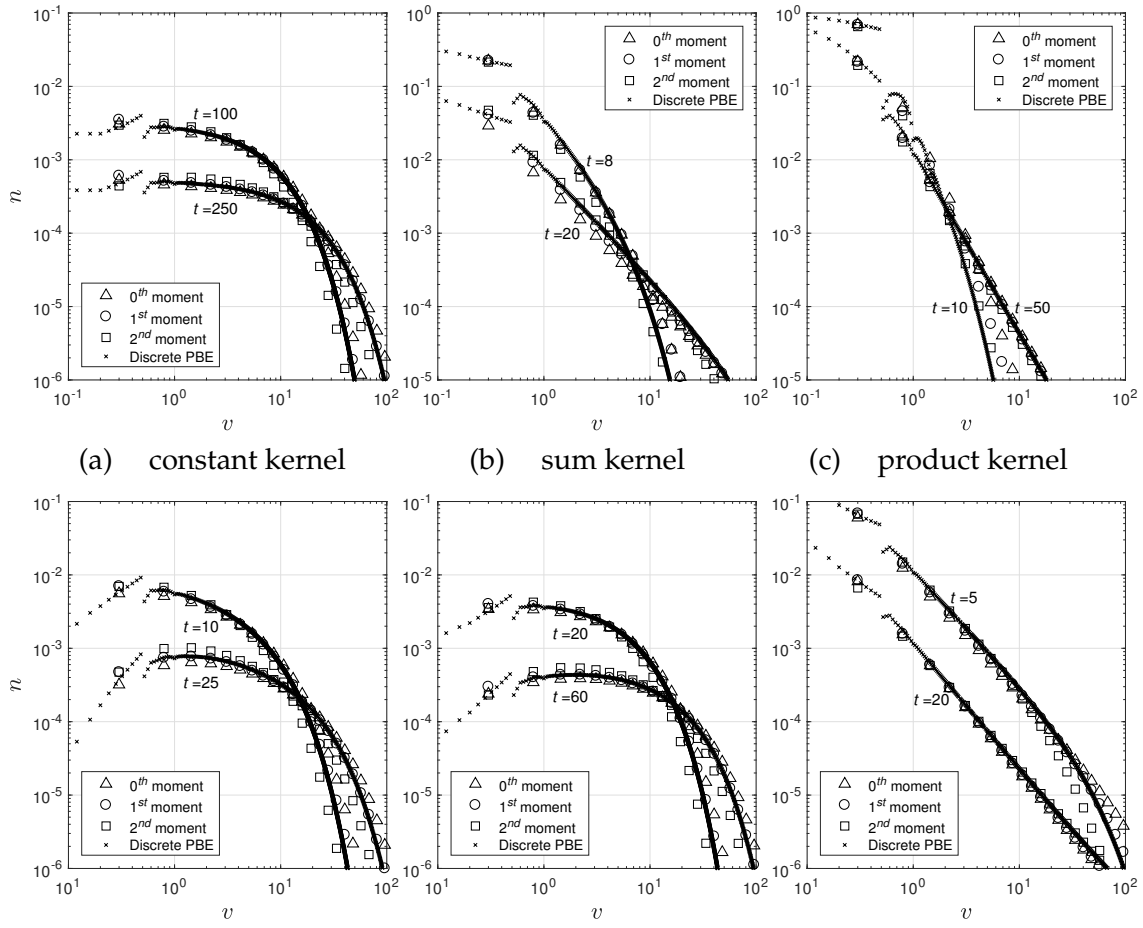

(a) constant kernel (b) sum kernel (c) product kernel

(d) Brownian kernel (e) free-molecular kernel (f) shear kernel

Fig. 3.9 Coagulation process with a monodisperse initial distribution

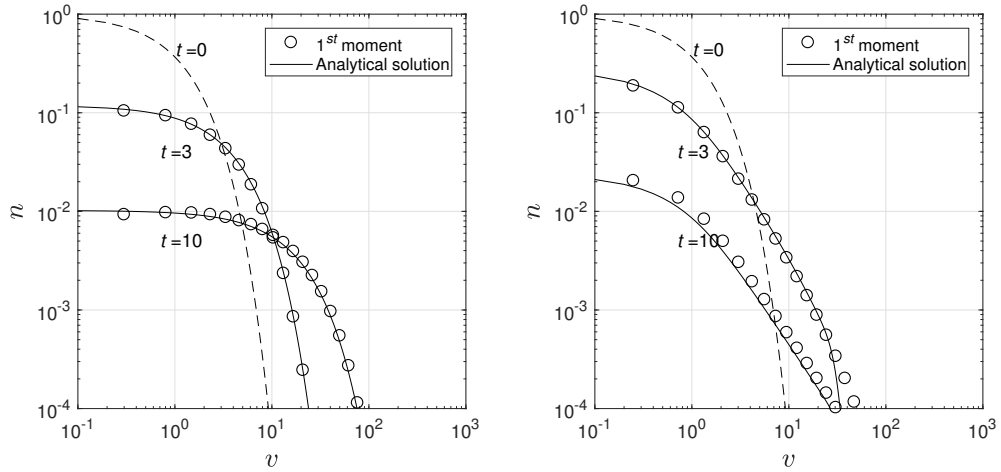

(a) constant kernel ($\beta(v,w) = 1$) (b) sum kernel ($\beta(v,w) = 0.5(v+w)$)

Fig. 3.10 Coagulation and growth (size-dependent), comparison of simulation with the analytical solution by Ramabhadran et al. [141]

	Number of sub-interval pairs		Number of product operations
Number of grid	30	60	in each sub-interval pair
Kumar and Ramkrishna method	1735	6863	3
the proposed method	1914	7244	3

Table 3.3 The number of sub-interval and number of product operations for Kumar's method and the proposed method

methods. About 10% more sub-interval pairs are divided in the proposed method than the Kumar and Ramkrishna method, according to Eq.3.20 and [121]. With respect to each sub-interval pair, three times of product operations are executed. Therefore, the time consumption of the proposed method is around 10% longer than Kuamr's method.

Now the aspect of accuracy and adaptivity of these two methods is compared. First of all, a standard exponential grid with an exponential rate of 1.3 and 30 grid points (Fig. 3.11(a)) is used for the pure coagulation process with the exponential initial distribution and the constant kernel to test the accuracy of the proposed method and Kuamr's method (Fig. 3.11(b). The results of both methods are in well accordance with the reference data by the discrete PBE method. However, the advantage of the proposed method is underlined in the test with a distorted grid in which the length ratio of neighbouring intervals is set to 1:9 on the basis of the exponential grid. The prediction by the novel method is still exactly lying on the reference curve while the points by the Kumar and Ramkrishna method are flying far away. Therefore, Kumar and Ramkrishna method fails in the senario of complicated grids due to that the coagulation source is only distributed on the neibouring two intervals with a fixed interpolating ratio. Nevertheless, the proposed method seeks for exact locations of sub-interval pairs according to the actual grid. Hence, novel method performs accurately with an excellent flexibility. This is very crucial when the distribution is in multi-mode, matched with the PBE grid with varying densities.

3.3.9 The study of self-preserving distributions

The shape of the size distribution of colloidal dispersion, starting with any initial distributions, undergoing Brownian coagulation does not change after some time and becomes 'self-preserving' [144–147]. The self-preserving size distributions, have been calculated for both the free-molecular (Eq. 3.25) and continuum (Eq. 3.24) and regimes. After a certain time-lag (τ^{fr} for the free-molecular regime and τ^{c} for the

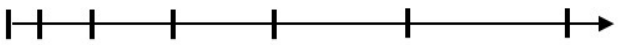

(a) The standard exponential grid with an exponential rate 1.3

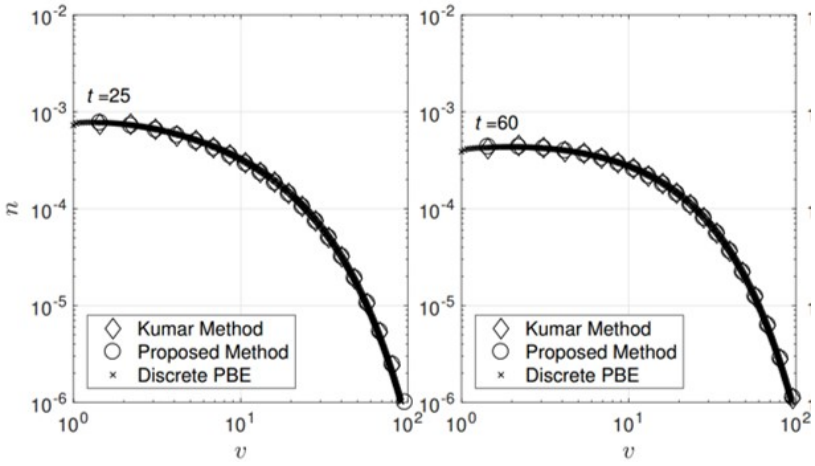

(b) The pure coagulation process on the standard exponential grid

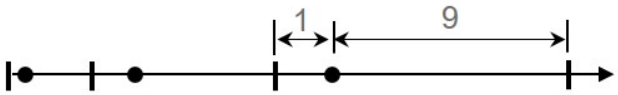

(c) The distorted grid with an exponential rate 1.3^2 and the distorted ratio of neighbouring interval 1:9

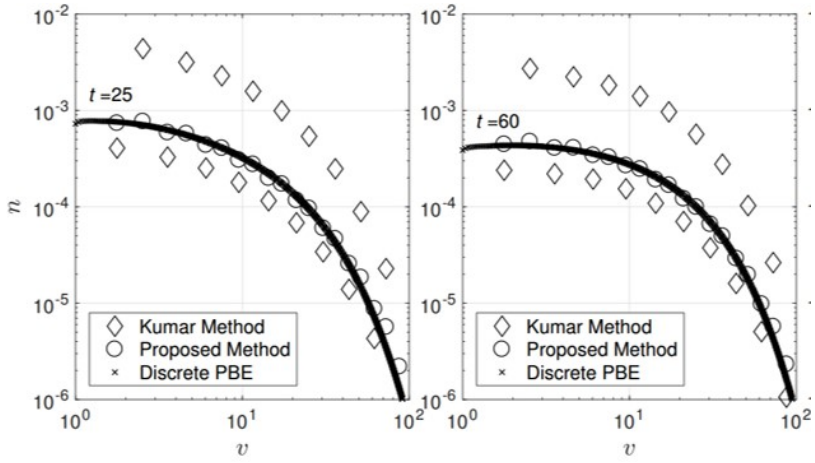

(d) The pure coagulation process on the distorted distribution

Fig. 3.11 The comparison of accuracy of the pure coagualtion process with the constant kernel and an exponential initial distribution on different discretised grids using the proposed method and Kuamr's method

continuum regime, the normalised distribution will converge to an unvarying one:

$$\tau^{\mathrm{fr}} = t \cdot N_0 K^{\mathrm{fr}} \approx 4.0 \tag{3.29a}$$

$$\tau^{\mathrm{c}} = t \cdot N_0 K^{\mathrm{c}} \approx 6.0 \tag{3.29b}$$

where N_0 is the total number of particles and K^{fr} and K^{c} are the coefficients for the continuum kernel and the free-molecular kernel which are set to 1.0 in Eq. 3.24 and Eq. 3.25.

Fig. 3.12 demonstrates the 'self-preserving' distribution in the continuum regime and free-molecular regime calculated by the present discretisation method (circle dots), the discrete-sectional model (triangle dots) by Vemury et al. [146] and that calculated by Friedlander and Wang [144]. The normalised particle volume and normalised particle number function is defined, respectively, as

$$\eta = \frac{M_0 v}{M_1} \tag{3.30a}$$

$$\eta = \frac{M_1 n(v,t)}{M_0^2} \tag{3.30b}$$

where M_0 and M_1 are the total number and total volume of the the coagulated aerosol.

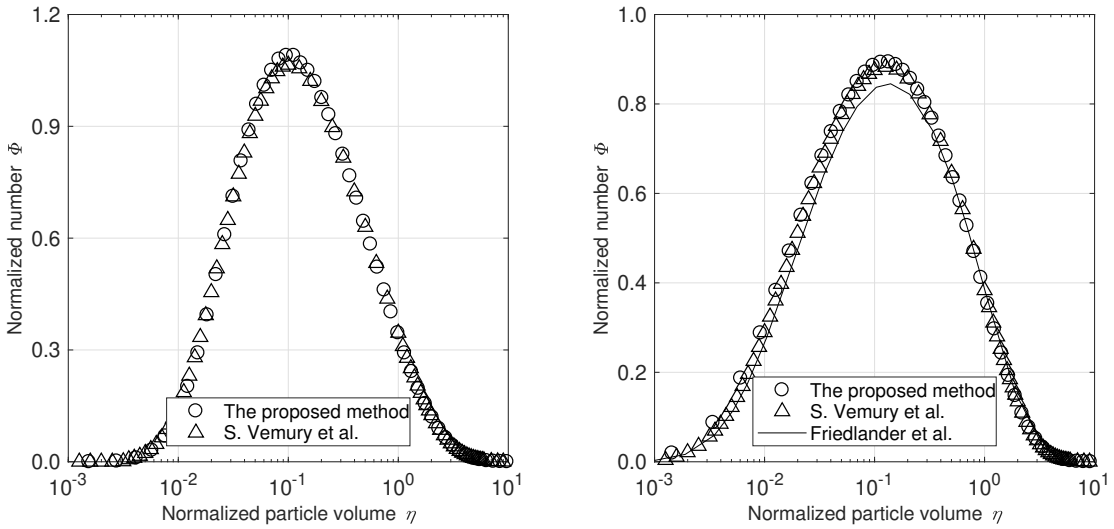

(a) Free-molecular kernel (b) Brownian kernel (Continuum regime)

Fig. 3.12 Numerical solutions of the self-preserving distributions for coagulation

The present number solution resembles closely the discrete solution by Vemury et al. [146] and is slightly different from that of Friedlander and Wang [144]. Therefore, the self-preserving distributions for the coagulation in the free-molecular regime and continuum regime can be captured by the present disctetisation method.

3.4 Application to an $Al(NO_3)_3$ suspension with coagulation process

In the present section, we apply the PBE method with our proposed conservative finite volume discretisation in a homogeneous case: an agitated coagulation-fragmentation process in a colloidal suspension solution in a batch reactor. The experiment was conducted by Bäbler and Morbidelli [148], with an aim to investigate how the initial values of solid volume fraction ϕ_0 and the stirred speed ω would affect the coagulation and fragmentation process in a 2.5 L stirred tank coagulator. The initial suspensions are white sulfate polystyrene latex, where the mean diameter of latex particles was 810 nm, measured by the authors using small-angle light scattering and declared by the producer, consistently. Before the batch experiments were carried out, the initial suspensions were stirred for approximately 15 min at 1000 rpm in order to break any loose aggregates. Subsequently, the coagulation process was triggered by quickly syringing the coagulant solution (20% $Al(NO_3)_3$ in water) inside the coagulator, finally reaching a steady state, balanced by the breakage process.

In this numerical work, the PBE formulation includes a coagulation rate function, which is a joint Brownian and flow induced coagulation, and a power law breakage rate function. With the particle or cluster mass as a continuous variable, the PBE reads as

$$\begin{aligned}\frac{\partial N(v,t)}{\partial t} = &\frac{1}{2}\int_0^v \beta(v-w,w)n(v-w,t)n(w,t)dw - n(v,t)\int_0^\infty \beta(v,w)n(w,t)dv' \\ &+ \int_v^\infty \gamma(w)b(v,w)n(w,t)dv' - \gamma(w)n(v,t)\end{aligned} \tag{3.31}$$

Two mechanisms contribute to the collisions of particles or clusters in the agitated suspensions: the Brownian motion and the induced relative velocity by the fluid flow. The coagulation rate functions for the Brownian and flow induced motions are donated [82, 149], respectively, as

$$\beta^{\mathrm{Br}}(v,w) = \frac{2k_{\mathrm{B}}T}{3\mu_f}\left(\frac{1}{R(v)} + \frac{1}{R(w)}\right)(R(v)+R(w)) \tag{3.32a}$$

$$\beta^{\mathrm{Fl}}(v,w) = \alpha G^{\mathrm{s}} \left((R(v) + R(w) \right)^3 \tag{3.32b}$$

$$\beta(v,w) = \beta^{\mathrm{Br}}(v,w) + \beta^{\mathrm{Fl}}(v,w) \tag{3.32}$$

Thereby, k_{B} is the Boltzman constant, T is the temperature, μ_f is the dynamic viscosity of the continuous fluid. $R(x)$ is the radius of a particle of mass x. G^{s} refers to the shear rate in the fluid, representing the intensity of the coagulation induced by the fluid. Bäbler and Morbidelli [148] calculated the average shear rate in the stirred coagulator using commercial CFD software Fluent. Correspondingly, α is a numerical constant depending on the type of flow. In an isotropic homogeneous turbulent flow and for particles smaller than Kolmogorov length scale with negligible inertial, Saffman and Turner [149] derived $\alpha = 1.29$ and $G^{\mathrm{s}} = (\epsilon/\nu_f)^{1/2}$. For many real coagulation experiments, the value of α is estimated smaller than unity, claimed due to physical features and chemical interactions of the clusters as well as heterogeneity of the flow field. For instance, Waldner et al. [150] estimate $\alpha \approx 0.2$ for the coagulation of fully destabilized polystyrene particles in a stirred tank, and Nopen et al. [151] report $\alpha \approx 0.01$ for the flocculation of activated sludge. The fractal scaling concept can often be used to characterized the structure of clusters created through coagulation in quiescent suspensions that the fractal aggregates is composed of spherical primary particles. Therein, a characteristic size of the fractal clusters is related with its dimensional volume x, as [152]

$$\frac{v}{V_{\mathrm{p}}} = k_{\mathrm{f}} \left(\frac{R_{\mathrm{g}}(v)}{R_{\mathrm{p}}} \right)^{d_{\mathrm{f}}} \tag{3.33}$$

where $R_{\mathrm{p}} = 405\mathrm{nm}$ and V_{p} are the radius and volume of the primary particle. In the batch reactor, we believe that loose connected aggregates are likely to be broken by stirring flow fluid, thus the particles tend to be somewhat denser clusters with $d_{\mathrm{f}} \approx 2.1$. Bäbler and Morbidelli [148] proposed $R_{\mathrm{g}}(V_{\mathrm{p}}) = 313.7\mathrm{nm}$ so that the fractal prefactor is determined $k_{\mathrm{f}} = 1.71$.

Comparatively, the knowledge of a breakage event is shortly given, despite its significant role in the agitated suspensions. The breakage is generally assumed as a kinetics process due to a hydrodynamic stress on the particles exerted by the fluid flow, expressed as [153]

$$k_\beta(v) = \gamma G^L R(v)^\nu \tag{3.34}$$

where γ, L and ν are positive empirical parameters. As well, since the explicit expressions for the fragment distribution are rarely provided, we use a minimalistic

Experimental conditions	$\phi(\times 10^{-6})$	1.8-40
	$R_{\mathrm{p}}(\mu\mathrm{m})$	0.41
Brownian coagulation	$T(\mathrm{K})$	298
	μ_f ($\mathrm{Pa}\cdot\mathrm{s}$)	1.0×10^{-3}
Flow induced coagulation	$G^s(\mathrm{s}^{-1})$	613
	α	0.15
Erosional breakage	L	0.001
	ν	6.3
	γ	1.75×10^{-5}

Table 3.4 Interpretation of the model parameters for 635 rmp

mode: the particles splits into $w \geq 2$ fragments of equal size, reads according to [154]

$$b(v,w) = w\delta(v - \frac{v}{w}) \tag{3.35}$$

Bäbler and Morbidelli [148] use non-dimensional PBE method with the consistent coagulation and breakage modes mentioned above to analyse this coagulation-fragmentation process. The key parameters were determined through dimensionless analysis and using the experimental findings that how the mean particles features (mean radius of gyration) varies with the solid volume fraction. We have modified some parameters in order to achieve the variation of mean radius of gyration in the temporal domain, correctly compared with the experimental results. The parameters are listed in Table 3,

Figure 3.13 shows the calculated normalized radius of gyration varies with regard to time on the effect of different solid concentrations, plotted together with the measured results. The agitated suspensions grow quickly before normalized T is less than 10 and after that, the aggregates grow smoothly and approach a steady state. It signifies the growth process yields to the similarity principle, which is the typical features of the coagulation process in the temporal domain. The solid concentration only affects the mean particle size in the steady state. Comparatively, the rapid growth period of the numerical solutions is much shorter than experimental data, implying that the parameters in the model still need to be calibrated.

Figure 3.14 vividly depicts the numerical solutions of the temporal evolution of the particle size distribution (PSD) for different solid volume fractions at stirring speed 630 rpm, which is the outstanding strength of the PBE method: to predict the evolution of the distribution of one or more properties that characterize the individual particles, rather than the integrated value of the properties. The primary impression of these plots seems to be of no differences, implying the similarity

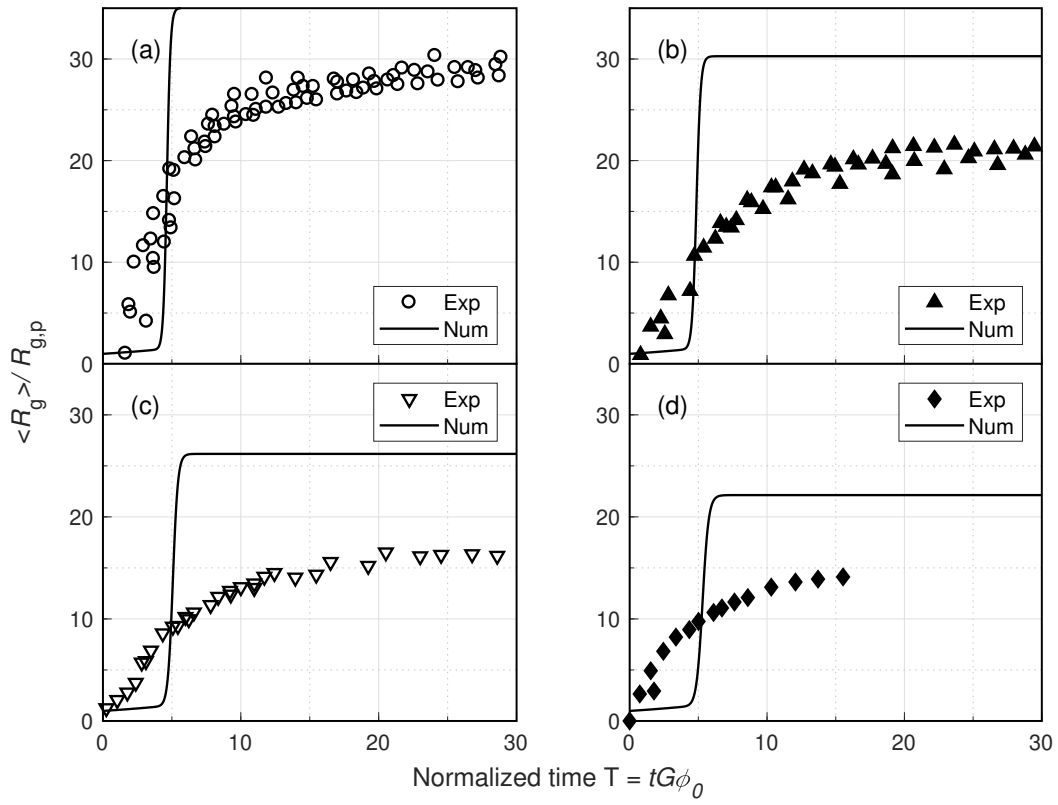

Fig. 3.13 Temporal evolution of the normalized radius of gyration for various values of the solid volume fraction at stirring speed of 635 rpm: (a) $\phi_0 = 4 \times 10^{-5}$, (b) $\phi_0 = 2 \times 10^{-5}$, (c) $\phi_0 = 1 \times 10^{-5}$, (d) $\phi_0 = 4.5 \times 10^{-6}$

principle of the coagulation process, although the critical particle size whose number density below 10^{15} is slightly larger at a higher solid concentration. We finds a turning point in each subplots at about $T = 4.5$, which is the moment that the clusters start a rapidly growth as well as the equally matched moment between the Brownian coagulation and the turbulent flow induced coagulation.

3.5 Conclusions

In this paper, we presented a conservative finite volume method for the discretisation of the PBE with nucleation, growth and coagulation. The main innovation of the method lies in the discretisation scheme for coagulation, in which the discretised source contributions are rigorously derived from the continuous PBE on the finite volume scheme, with the only approximation in coagulation kernels. The method thus attains accurate prediction of the distribution with a small number of PBE nodes (or sections) as well as conserves the first moment (or any other single moment).

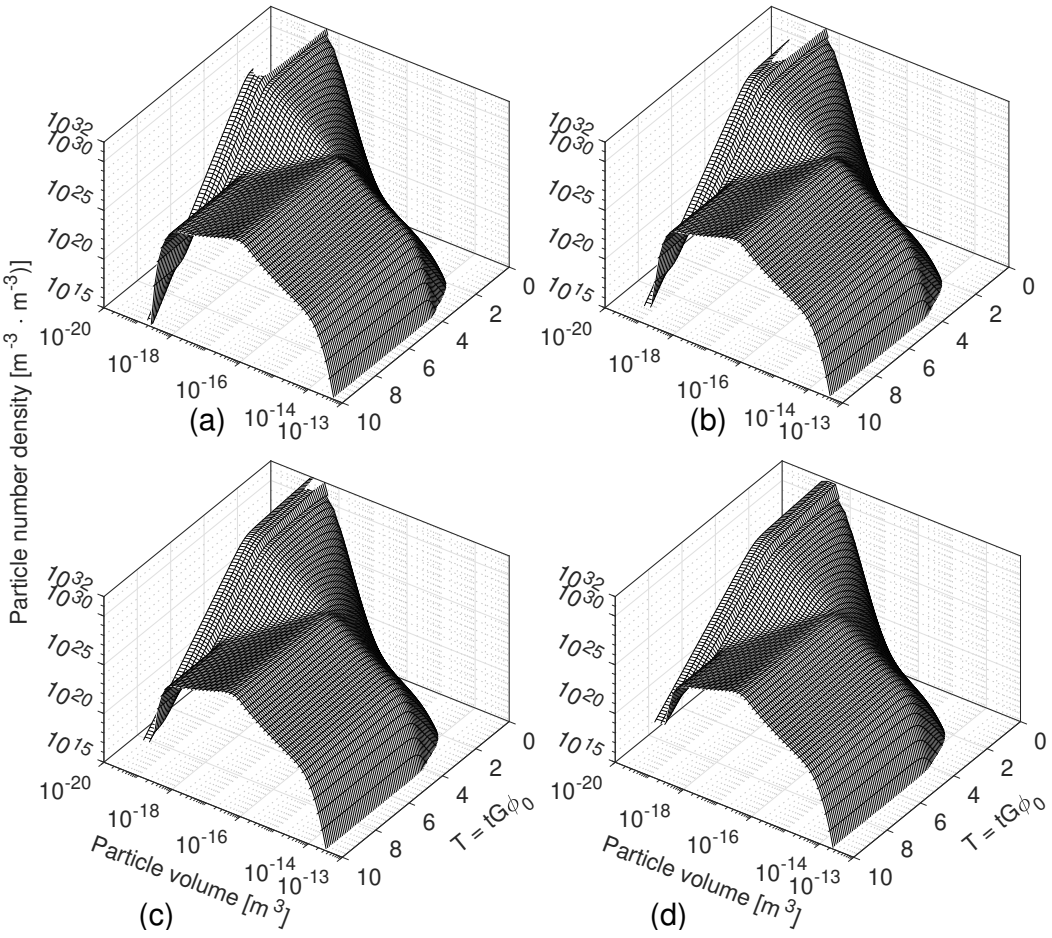

Fig. 3.14 Simulated temporal evolution of the PSD for various values of the solid volume fraction at stirring speed of 635 rpm: (a) $\phi_0 = 4 \times 10^{-5}$, (b) $\phi_0 = 2 \times 10^{-5}$, (c) $\phi_0 = 1 \times 10^{-5}$, (d) $\phi_0 = 4.5 \times 10^{-6}$

Furthermore, the method is applicable to an arbitrary non-uniform grid and could also be combined with an adaptive grid approach, such as the one developed in [102].

The main elements of the method are: a) the employment of an auxiliary grid of complementary points that are needed to accurately calculate all coagulation events, b) a geometric approach to the evaluation of the double integrals resulting from the finite volume integration of the coagulation terms, c) and c) the detailed balancing of source and sink terms to ensure moment conservation. The auxiliary grid, geometric factors and volumetric dependence of the kernels are all pre-calculated and stored, and thus do not affect the computational efficiency of the method. An Extensive test on the proposed method was carried out, by comparing with analytical solutions, direct numerical solutions by the discrete PBE approach and the 'self-preserved' distribution, with both theoretical and physically realistic kernels. Results showed

that the method produces very accurate solutions that conserve the chosen moment, even on coarse grids. Moreover, the proposed method preforms more accurately in the distorted PBE grid than traditional methods (Kumar and Ramakrishna method).

For an application, the proposed discretisation method of the PBE has successfully predicted the coagulation and breakage process of a colloidal suspension: white sulfate polystyrene and the coagulant $Al(NO_3)_3$ solution. The variation of mean radius of gyrations for the particles coincides well with the experimental results and the temporal evolution of the particle size distribution has showed powerful advantages of the discretised population balance modelling and robust feasibility of the novel moment-conserved method.

Chapter 4

Population balance modelling of laminar ethylene sooting flames and laser diagnostic signals

Laminar diffusion flames present an elementary configuration for investigating soot formation and validating kinetic models before these are transferred to turbulent combustors. In this chapter, the Santoro flames are simulated in order to test the proposed method and coupling the PBE with the a full 2D unsteady CFD simulation, as well as to explore the evolution of soot formation in the combustion issues.

In the first section, the proposed method in Chapter 3 is coupled with fluid dynamics, chemical kinetics, transport phenomena and radiation, in order to simulate soot formation in a laminar co-flow diffusion flame. This flame has been investigated experimentally by Santoro et al. [35, 155] and numerically in a number of studies (e.g. [66, 107]).

The reason for employing the laminar co-flow diffusion flame as our test case is that its simulation requires coupling of the PBE with a full 2D unsteady CFD simulation, as opposed to ideal reactors and 1-D premixed laminar flames that can be computed with 0-D and 1-D codes and assumed temperature profiles. The main objective here is to investigate the numerical performance of the method in the context of a comprehensive unsteady CFD simulation, and in particular to measure the CPU overhead imposed by the proposed method. The study therefore paves the way for the application of the method to turbulent flames and combustors.

In the rest, we present a joint experimental and modelling investigation of soot formation in a laminar co-flow burner. The diffusion flames are analysed with the aid of laser diagnostic techniques, including elastic light scattering (ELS), planar

laser-induced fluorescence of OH (OH-PLIF) and line-of-sight attenuation (LOSA). The experimental dataset is supplemented by location-specific TEM images of thermophoretically sampled soot particles. Additionally, the experimental line-of-sight attenuation signal is converted into a measure for the integrated soot volume fraction along the centreline. In order to predict the evolution of the soot particle size distribution throughout the flame, we combine a soot model based on the population balance equation (PBE) with an in-house CFD software. Our approach incorporates a complete set of soot kinetics for PAH-based nucleation and condensation, HACA-based surface growth and oxidation as well as size-dependent coagulation and agglomeration. For chemical reactions in the gas phase, we consider three different detailed mechanisms (ABF, BBP and KM2, respectively). The model is validated comprehensively by comparing experimental laser diagnostic signals with 'predicted signals' computed from the modelled gas phase composition and soot size distribution.

The predicted signals obtained from the PBE-based modelling approach are in acceptable agreement with laser diagnostic measurements in terms of the spatial distribution of soot and the absolute values of soot volume fraction. Our analyses of the remnant discrepancies indicate that the accuracy of soot predictions is much influenced by the gas phase reaction mechanism. In particular, we find that the simulations using the BBP and KM2 mechanisms reproduce the correct lateral separation of the two sooty wings of the flame. Unfortunately, the soot production near the centreline in between the sooty wings is overestimated by the BBP and KM2 mechanisms and completely omitted by the ABF mechanism. In addition, sensitivity analyses on the empirical parameters show that while the magnitude of the nucleation rate does not significantly affect soot formation, the competition between nucleation and growth influences the temporal and spatial distribution of soot.

4.1 Application of the conservative method in Santoro flame

4.1.1 Test case and simulation setup

The co-flow diffusion burner (Santoro burner) [35] consists of an 11.1 mm ID nozzle protruding 4 mm above a 101.6 mm diameter co-flow, and is shown schematically in Fig. 4.6. The simulation is carried out with the in-house CFD code BOFFIN. The

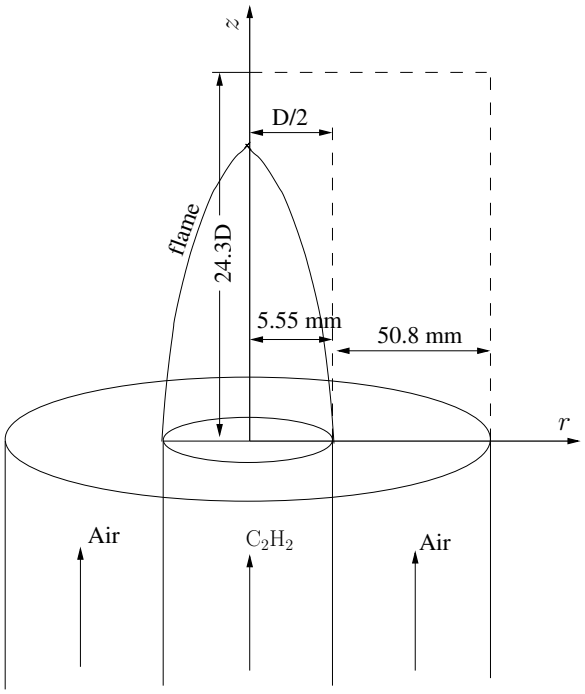

Fig. 4.1 Representation of the computational domain

spatial grid includes 200 and 100 cells in the axial and radial directions respectively, and is refined towards the jet exit and the interface between the fuel and air streams. A uniform velocity profile is set at the inlet, while ambient pressure is assumed at the outlet. A symmetry boundary condition is applied along the flame centreline, while the velocity at the edge of the domain is set equal to the input velocity of the air channel.

4.1.2 Coupling of PBE and flow

To obtain the spatially inhomogeneous population balance equation, we consider a spatially varying number density, $n(v,\mathbf{x},t)$, and augment the PBE with terms representing transport in physical space, while the nucleation and growth kinetics are functions of the species concentration vector $\mathbf{Y}(\mathbf{x},t)$:

In a continuum approach, soot is commonly described in terms of the number of particles per unit of volume in physical space whose characteristic properties take on particular values, $n(v,\mathbf{x},t)$. Formally, the population balance equation (PBE) is a statement on the continuity of number density in $(v,\mathbf{x})$, with the augmented terms representing transport in physical space. Considering soot nucleation and coagulation as source/sink processes, the PBE is given by

$$\begin{aligned}\frac{\partial n(v,\mathbf{x},t)}{\partial t} + \sum_{j=1}^{3}\frac{\partial\left((u_j + U_j^{\mathrm{T}})n(v,\mathbf{x},t)\right)}{\partial x_j} + \frac{\partial\left(G(v,\mathbf{Y})n(v,\mathbf{x},t)\right)}{\partial v} = \\ -\sum_{j=1}^{3}\frac{\partial K_j(v,\mathbf{x},t)}{\partial x_j} + \dot{B}(\mathbf{Y})\delta(v-v_0) \\ +\frac{1}{2}\int_0^v \beta(v-v',v')n(v-v',\mathbf{x},t)n(v',\mathbf{x},t)\,dv' \\ -\int_0^\infty \beta(v,v')n(v,\mathbf{x},t)n(v',\mathbf{x},t)\,dv',\end{aligned} \tag{4.1}$$

where $G(v,\mathbf{Y})$ is the combined surface growth and oxidation rate, $\dot{B}$ represents the nucleation rate, v_0 is the nuclei volume and $\beta(v,v')$ denotes the coagulation kernel. $K_j(v,\mathbf{x},t)$, moreover, represents the diffusive flux of number density along the j^{th} coordinate direction in physical space,

$$K_j(v,\mathbf{x},t) = -D_{\mathrm{p}}(v,\mathbf{x},t)\frac{\partial n(v,\mathbf{x},t)}{\partial x_j}, \tag{4.2}$$

and $D_{\mathrm{p}}(v,\mathbf{x},t)$ represents the kinematic diffusivity of a particle with volume v [13]. For spherical particles, $D_{\mathrm{p}}(v,\mathbf{x},t)$ is determined by the particle diameter, while for aggregates the hydrodynamic diameter $d_{\mathrm{h}}(v)$ controls $D_{\mathrm{p}}(v,\mathbf{x},t)$ as indicated in investigations on the dynamic properties of polymers suspended in a solvent [156].

In the spatial convection term of Eq. 4.1, $\mathbf{U}^{\mathrm{T}}$ represents the thermophoretic velocity that a particle immersed in a flow with temperature gradients experiences. Depending on the Knudsen number Kn, two different cases for computing the thermophoretic velocity are considered [157]. In the free-molecular regime ($Kn > 10$), particles are small in size and thus spherical in shape and the thermophoretic velocity $\mathbf{U}^{\mathrm{T}}$ can be estimated as [158]

$$U_j^{\mathrm{T}} = -\frac{3\nu}{4(1+\frac{\pi\alpha_{\mathrm{m}}}{8})}\frac{1}{T}\frac{\partial T}{\partial x_j}, \tag{4.3}$$

where the accommodation factor α_{m} is set to 0.9. For small Knudsen numbers ($Kn < 0.1$) and in the continuum regime, thermophoresis is negligible. However, in the transient regime between the free-molecular and continuum limiting cases, the thermophoretic velocity is estimated according to [159]

$$U_j^{\mathrm{T}} = -\frac{2C_{\mathrm{s}}\nu(\frac{k_{\mathrm{g}}}{k_{\mathrm{p}}} + C_{\mathrm{t}}Kn)}{(1+2C_{\mathrm{m}}Kn)(1+\frac{2k_{\mathrm{g}}}{k_{\mathrm{p}}}+2C_{\mathrm{t}}Kn)}\frac{1}{T}\frac{\partial T}{\partial x_j}, \tag{4.4}$$

where k_g represents the thermal conductivity of the ambient gas and $k_p = 0.26\,\mathrm{W/m-K}$ is the thermal conductivity of a soot particle [160]. $C_m = 1.14$ and $C_t = 2.18$, moreover, are model parameters [159]. Toda et al. [161] conducted accurate measurements of thermophoresis in microgravity conditions and introduced a correction parameter C_s based on the diameter d_p of a spherical particle

$$C_s = 2.72 \times 10^5 (d_p - 2.7 \times 10^{-6}) + 3.19. \tag{4.5}$$

For fractal aggregates, d_p is replaced by the diameter of gyration d_g in Eq. 4.5, see Section 4.3.3.

In order to allow for the application of tailored time integration schemes, the PBE in Eq. 4.1 is solved in two fractional steps [162, Section 6.3]. The first step involves convection and diffusion in physical space, while the second fractional step encompasses convection and source/sink processes in particle volume space. The governing equations are discretised in $(\mathbf{x}, v)$ using a standard volume scheme [163] and incorporated into our in-house research software BOFFIN [164]. For the cell face fluxes in v-space, we adopt the high resolution formulation of Koren [108]. The double integrals that occur in the cell averages of the coagulation terms, moreover, are evaluated using the novel approach recently developed in Chapter 3. In light of previous accuracy and convergence analyses, we invoke $m_p = 60$ finite volume cells in v-space, $v \in [0, v_{max}]$, $v_{max} = 10^{-17}\,\mathrm{m}^3$.

The convection-diffusion step is temporally integrated using the second order accurate Crank-Nicolson scheme, while we employ the fifth order accurate Runge-Kutta scheme DOPRI5 by Hairer et al. [165] for the PBE fractional step.

Eq. 4.1 must be coupled with the continuity, Navier-Stokes, energy and species transport equations. Numerical solution of the complete system is accomplished by treating the discretised number densities as transported scalars, with the source terms for the PBE provided by the proposed method.

4.1.3 Kinetic models

The gas phase chemical kinetics are described by the ABF mechanism [60] The soot model considers a complete set of processes: nucleation, surface growth and oxidation, PAH surface condensation and particle coagulation. The nucleation step is described by the dimerisation of two PAH species [61], while the HACA mechanism [60] extended with three extra reactions [62] is employed for the growth and oxidation processes. Soot surface growth is also enhanced by the condensation

of PAHs, especially in lower temperature regions of a diffusion flame. The detailed modelling of soot kinetics and morphology is elaborated in 4.3.2.

4.1.4 Results

Figure 4.2 shows the radial profiles of C_2H_2 mole fraction, OH mole fraction and the temperature in several axial cross-sections. The C_2H_2 mole fraction, OH mole fraction and the temperature profiles at the cross-section of 20 mm are matched well the experiment data, despite small deviations for the mole fraction of C_2H_2 around the center line and the mole fraction of OH on the area of peak concentration. However, the simulated C_2H_2 mole fraction at the cross-section of 7 mm is less than 80% higher than the measured results if the distance away from the centerline is less than 5 mm. This is due to the overprediction of C_2H_2 in the rich fuel zone by the ABF mechanism where The ethylene fuel should not transform in a very fast way. In addition, the predicted OH mole fraction at the cross-section of 70 mm is smaller than experiment data if the radial distance is less than 3 mm while it is higher if the radial distance is above 3 mm. The predicted peak zone of OH concentration is approximately 1.5 mm away from the centerline, compared with the experimental capture. That deviation shows that in the simulation, the OH species is over consumed close to the centerline due to the overproduction of soot, while the opposite for the radial distance is larger than 3 mm. The calculated temperature is 100 - 200 K higher near the centerline region at 70 mm above the nozzle exit plane, which affects the growth and oxidation rate in the simulation.

Figure 4.3 compares the measured values of the integrated soot volume fraction (ISVF) [35] on each cross-section above from the nozzle exit plane with the predictions by the coupled CFD-PBE simulation. A convergent result is achieved by the PBE with 60 PBE grid nodes, while the solution with 40 nodes exhibits an underprediction. The comparison with the experimental results for the integrated soot volume fraction is quite good.

Fig.4.4 shows comparisons of the predicted temperature profiles with the measured data of Santoro [35] at several heights and at the centreline of the flame. The predicted temperature is about 50-100 K lower than the measured data around the flame centre at 20-30 mm height above the burner, while it is about 50 K higher downstream at 50 mm height. However, the temperature profiles are overall well predicted at the two wings of the flames, around 3 mm or further away from the centreline. Finally, Figure 4.5 shows the spatial evolution of the particle size distributions on the axial line of 3 mm parallel to the centreline, where the soot production

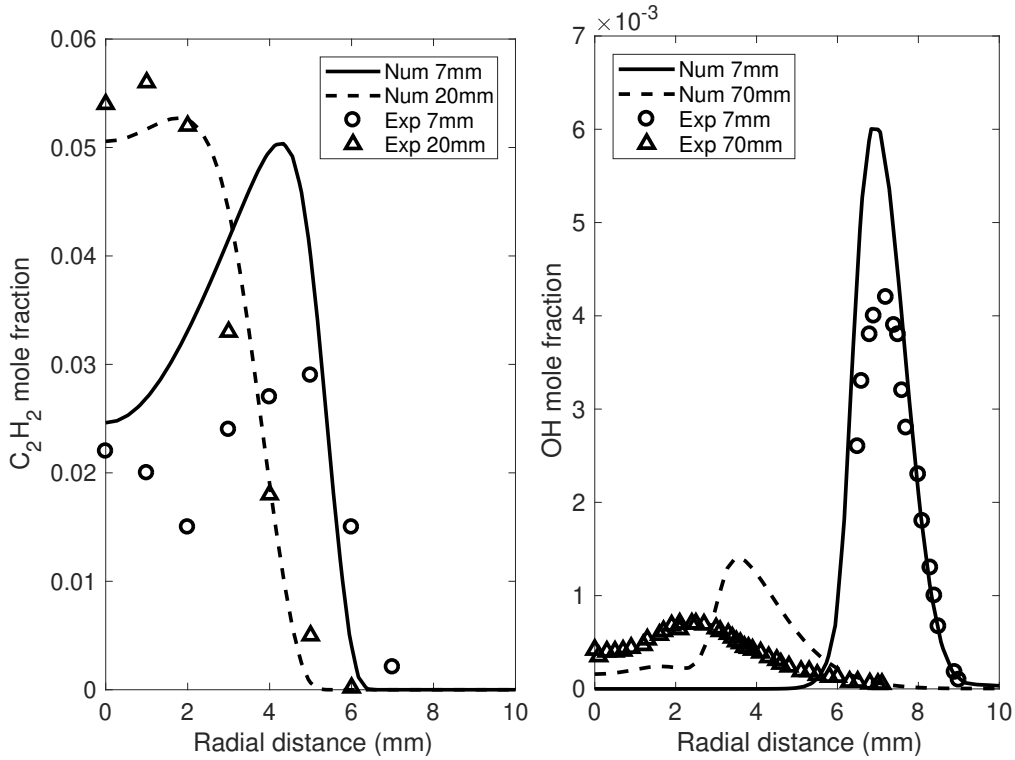

(a) C_2H_2 (b) OH

Fig. 4.2 Radial profiles of C_2H_2, OH

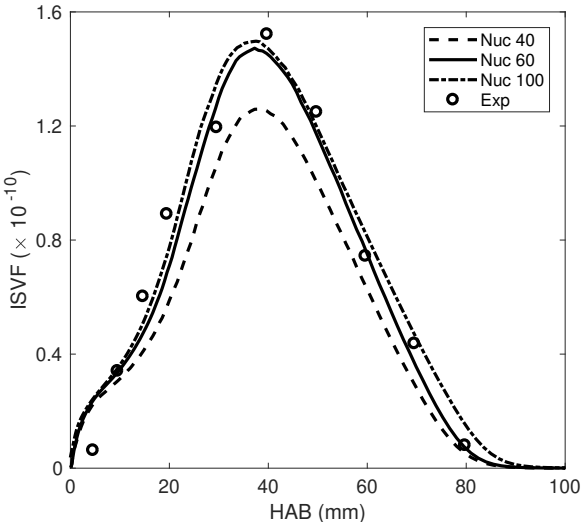

Fig. 4.3 Integrated soot volume fraction at different heights above burner, predictions with different PBE grids

is maximum. A bimodal distribution begins to form at a height of 10 mm and is evident at 30 mm height above the burner.

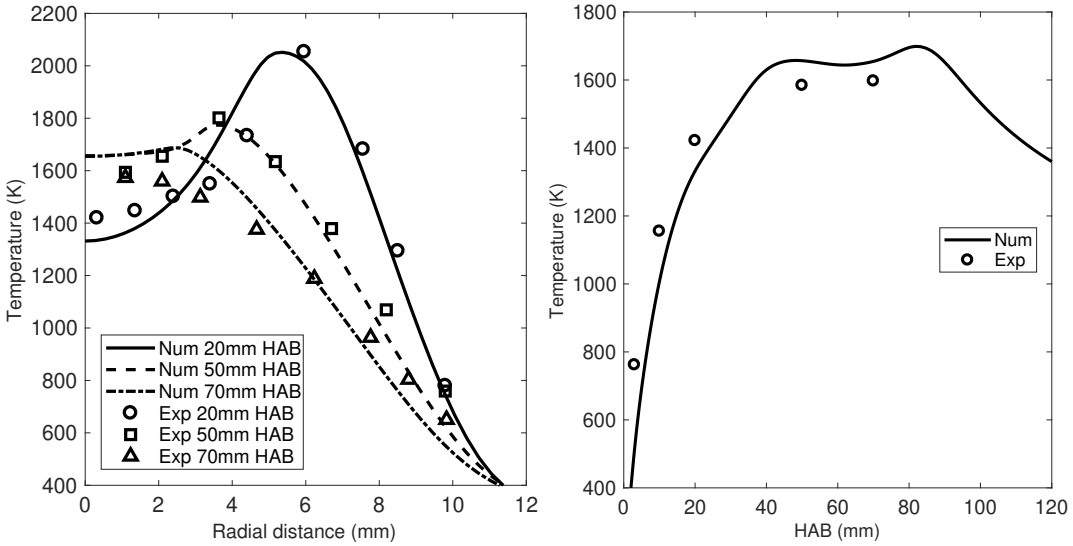

(a) Radial profiles of temperature at various (b) The temperature profile on the centreline cross-section

Fig. 4.4 Comparisons of temperature profiles at different height above the burner and on the centreline

Subroutines	Time consumption (%)		
	40 nodes	60 nodes	100 nodes
Flow field	19.5	15.5	11.1
Scalar convection & diffusion	29.5	40.0	51.2
Chemistry	46.0	36.3	23.5
PBE (total)	5.0	8.2	14.2
Breakdown of PBE step:			
nucleation & growth	0.8	0.8	0.7
coagulation algorithm	1.6	2.8	5.1
coagulation kernel	2.6	4.6	8.4

Table 4.1 CPU time breakdown for the various parts of the coupled CFD-PBE simulation (average over 200 time steps).

Table 4.1 shows a breakdown of the CPU time spent in different parts of the code, for three different PBE grids. The part spent in the PBE solution occupies only 5.0% of the total CPU time when 40 PBE nodes are employed, which increases to 8.2% with 60 PBE nodes and to 14.2% with 100 nodes. The number of operations in the growth term is proportional to the number of PBE grid nodes, while that in the coagulation term is proportional to square of the number of nodes. Therefore, the coagulation process is the most time-consuming part of the PBE calculation.

Furthermore, more than 50% of the computational cost for the PBE (in the 60-node case) is consumed for updating the coagulation kernel to account for its dependence on the ambient conditions. The main purpose of this case study is to demonstrate that the coupling of the proposed method for discretising the PBE is feasible for coupling with CFD, as it only occupies 5% - 15% of the total time spent in the complete CFD-PBE simulation.

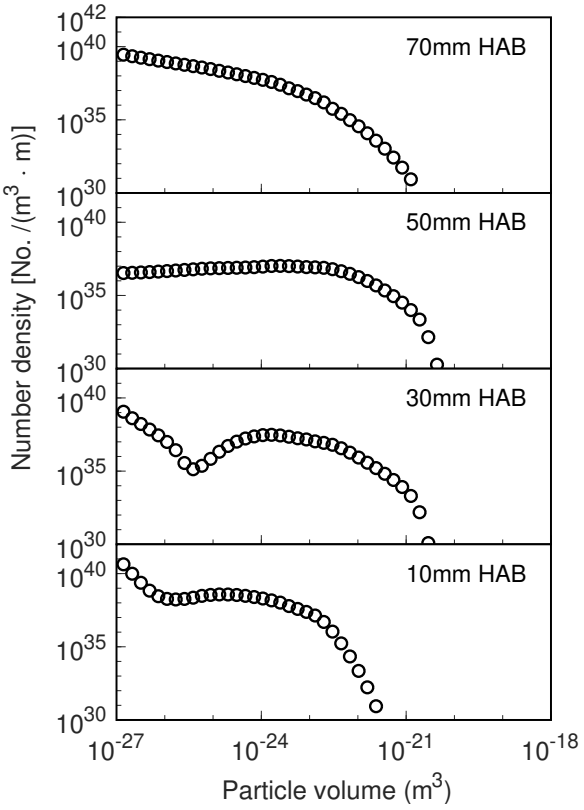

Fig. 4.5 Particle size distribution at different heights on the axial line 3mm away from the centerline

4.2 Simulation of Carlos' flames and the experimental setup

In the present and following sections, the spatially inhomogeneous, univariate PBE is combined with the conservation laws of mass, momentum, energy and gas phase composition, enabling us to predict the evolution of soot formation with respect to particle size throughout the flow domain. Here, we adopt a complete set of soot kinetics, accounting for nucleation, surface growth, coagulation, aggregation,

thermophoresis and radiation. Furthermore, laser diagnostic measurements on a laminar co-flow diffusion flame are conducted and samples of soot particles are thermophoretically extracted. In particular, planar laser-induced fluorescence of OH (OH-PLIF) is used to validate the chemical kinetics and mixing, elastic light scattering (ELS) provides information about the spatial distribution of soot and line-of-sight attenuation measurements (LOSA) allow us to determine the soot volume fraction. Location-specific samples are extracted with the aid of a thermophoretic sampling device similar to that originally designed by Dobbins and Megaridis [166]. Following an idea pioneered by Connelly et al. [167], our physical model is validated by comparing 'predicted signals' computed from the gas phase composition and soot particle size distribution with experimental laser diagnostic signals. This approach is advantageous as it circumvents assumptions that are commonly made in converting experimental laser diagnostic signals into physically meaningful quantities. Finally, sensitivity analyses on key kinetic model constituents indicate potential causes for the remnant discrepancies we observe.

The spatial and temporal evolution of an ensemble of soot particles can physically be described by the population balance equation (PBE) [5]. The PBE is a convection-diffusion-reaction equation in which space and time are augmented by the particle properties, for example, size or volume, as additional independent coordinates. While we focus on the univariate PBE based on soot particle volume, more detailed multivariate population balance models for soot have been advanced in the course of the last decade. Blanquart and Pitsch [61] and Kholghy et al. [28], for instance, described a soot particle in terms of its volume, surface area and the hydrogen content on the surface or the hydrogen/carbon ratio.

In recent years, researchers have investigated directly discretising the PBE in particle property space. Gelbard et al. [128] and Rigopoulos and Jones [99], for example, applied a collocation-based finite element method, while Qamar et al. [100] investigated the accuracy of different high resolution finite volume schemes. In processes that are dominated by particle nucleation and growth, the number of grid points in particle property space can be significantly reduced by combining a direct discretisation scheme with grid adaptivity [101, 102, 168]. This is particularly advantageous in spatially inhomogeneous reactors, where the resolution requirements in particle property space may vary not only in time, but also across the flow domain [103, 169]. In many past investigations, about 30 grid points were invoked to represent the particle property distribution [104, 105], although much more stringent

resolution requirements were also reported, especially in the absence of coagulation and aggregation [106, 107].

The objectives of this work are threefold: First, we present OH-PLIF and ELS measurements characterising the flame structure, precursor species and soot appearance, as well as LOSA measurements that can be directly linked to the line-of-sight integrated soot volume fraction. Second, we combine a detailed PBE model for soot formation with an in-house CFD code to predict the evolution of the soot PSD throughout the flame. Herein, sensitivity analyses in terms of the gas-phase mechanisms and key empirical parameters in the soot kinetics aid us in deducing practical guidance for tuning the soot model. Third, based on predictions of chemical composition and soot PSD, we compute OH-PLIF, ELS and LOSA signals as a basis for a direct comparison with the experimental signals.

The work is organised as follows: In this section, the flame configurations investigated here and on the experimental measurement techniques is briefly summarised. Subsequently, in Section 4.3, the physical model for a reacting multicomponent gas is presented and the PBE-based soot model discussed. Here, we provide details on the evaluation of kinetic rates controlling the soot PSD and lay emphasis on an account of soot morphology. The computation of laser-diagnostic signals in terms of the gas phase composition and soot PSD is addressed in Section 4.4, prior to the validation of the physical model by comparing predicted and measured laser-diagnostic signals in Section 4.5. Concomitantly, the influence of the gas phase chemistry on the spatial distribution of soot precursors and key kinetic rates is elucidated. This is followed by a summary of the main observations in Section 4.6.

In order to elucidate the mechanisms of soot formation and for model validation, the laminar diffusion flame originally investigated by Santoro et al. [35] is well-suited as it constitutes a geometrically simple and reproducible standard configuration. The co-flow diffusion burner consists of a nozzle with an internal diameter of 11.1 mm protruding 4 mm above a 101.6 mm diameter co-flow tube (Figure 4.6). The flame is shielded from ambient air currents by a 400 mm tall chimney. The flame configurations we consider correspond to the non-smoking (NS) and incipient smoking (IS) cases analysed by Santoro et al. [35, 155]; ethylene flow rates were set to agree with these values to within experimental error. Three non-intrusive laser diagnostic techniques are employed: Elastic light scattering (ELS), planar laser-induced fluorescence (OH-PLIF) and line-of-sight attenuation (LOSA), supplemented by thermophoretic sampling.

For the ELS measurements, a Q-switched frequency-doubled Nd:YAG laser with four independent heads is used in conjunction with sheet-forming optics to illuminate a 23 mm $\times 400\,\mu$m region across the burner centreline (Figure 4.7). The ELS signal is collected using a CCD camera with a 105 mm f/2.8 lens placed perpendicular to the laser beam. The laser pulse energy is approximately 0.5 mJ and the repetition rate 10 Hz. Data from different heights is obtained by vertically translating the burner. Post-processing steps include background subtraction, pulse energy correction, beam profile correction, spatial calibration and image de-warping. Besides corrections that stem from the particulars of the experimental setup, no physical interpretation of the signal is attempted since the measurement process is, in part, included in our physical model [167]. The ELS signal originates from light scattered by both gas phase molecules and soot particles. In the presence of soot particles, however, the molecular contribution to the ELS signal is generally negligible and the Rayleigh-Debye-Gans theory of light scattered by fractal aggregates (RDG-FA) may be applied to compute the ELS signal [38].

The Nd:YAG laser is further used to pump a frequency-doubled Rhodamine 6G dye laser tuned to 283.6 nm to excite the $Q_1(8)$ $(v = 1 \leftarrow 0)$ transition in the $A^2\Sigma \leftarrow X^2\Pi$ electronic system of the OH radical. This transition has been chosen in order to reduce the sensitivity of the LIF signal to temperature. The fluorescence signals from the $(v = 0 \leftarrow 0)$ and $(v = 1 \leftarrow 1)$ branches were collected at 309 nm–315 nm with a gated intensifier and a CCD camera. Strong broadband fluorescence attributed to PAH species was detected in addition to fluorescence from the OH radical. The two fluorescence signals were separated by subtracting the signal detected when the laser is detuned from the OH spectral line from the signal recorded when the laser is tuned. Laser energy and sheet thickness were adjusted to ensure operation inside the linear LIF regime [170]. Post-processing steps similar to the ELS experiment were performed.

Furthermore, we employed a thermophoretic sampling device to extract soot particles. The device consists of a double-action pneumatic cylinder that introduces a 3 mm diameter holey carbon TEM grid into the flame, retracting after a pre-set residence time of 120 ms. The grid was held vertically during sampling in order to keep disruption of the flow at a minimum. Samples were imaged in a Jeol 2100+ transmission electron microscope (TEM) at an acceleration potential of 200 kV and particle size statistics were determined based on TEM images.

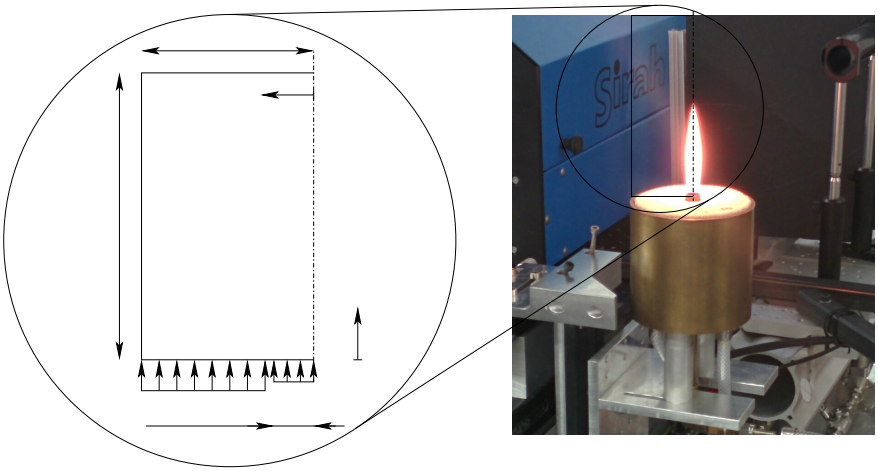

Fig. 4.6 Schematic illustration of the computational domain (left) and view of the non-smoking flame on Santoro's co-flow burner (right).

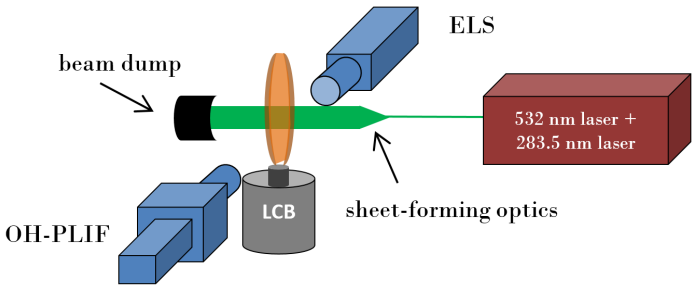

Fig. 4.7 Schematic of the laser diagnostic setup. The 532 nm and 283.5 nm beams are coincident above the burner.

4.3 Physical models

4.3.1 Gas phase transport and chemistry

Figure 4.6 schematically depicts the axisymmetric, two-dimensional domain we consider for the diffusion flame on the Santoro burner. A symmetry boundary condition is applied along the flame centreline, while homogeneous Neumann boundary conditions are applied along the lateral domain boundary and the outlets. Initially, the domain contains only air at ambient pressure and temperature; starting from this initial condition, the governing equations are temporally evolved into steady-state. The spatial grid encompasses 200 and 100 cells in the axial and radial directions, respectively, and is refined towards the jet exit and the interface between the fuel and air streams. Following common practice, we describe the gas phase in terms of $n+1$ reactive scalars $\mathbf{Y}(\mathbf{x}) = (Y_1(\mathbf{x}), \ldots, Y_n(\mathbf{x}), Y_{n+1}(\mathbf{x}))$, representing n species mass fractions and the mixture enthalpy. Within the ambient flow, the reactive scalars evolve according to the species transport equations and the energy conservation equation, respectively, and obey the constitutive relations for a multi-component ideal gas. The flow field, moreover, is governed by the continuity and momentum conservation equations for a Newtonian fluid.

In order to support the PAH-HACA framework for soot formation, three different chemical reaction mechanisms are considered. The first one is the ABF mechanism which encompasses 101 species and 544 chemical reactions [72, 60]. Here, the chemistry for small hydrocarbons is based on the GRI 1.2 mechanism which contributes most C_2 species as well as a skeletal mechanism for C_3 and C_4 species. The ABF mechanism includes polycyclic aromatic hydrocarbon (PAH) species up to pyrene ($C_{16}H_{10}$ or A_4), in particular, benzene, naphthalene, phenanthrene and pyrene (A_1–A_4), thus bridging the gap between PAH chemistry in the gas phase chemistry and soot formation. The ABF mechanism also serves as a reference for other reaction mechanisms used in modelling soot formation [66, 171].

The second chemical reaction mechanism we consider is provided by Blanquart et al. [172]. It involves 149 species and 928 reactions and accounts for all major pathways of PAH formation up to cyclopentapyrene ($C_{18}H_{10}$); for brevity, we refer to this mechanism as BBP in the following. The BBP mechanism has been developed based on an optimised version of GRI 3.0 [173] with an emphasis on the chemistry of soot precursors such as acetylene, the C_3H_4 isomers (allene and propyne), propene, butadiene and benzene. Finally, it has been extended to include the chemistry relevant to PAHs (benzene and toluene) and larger alkanes. The complete mechanism

has been validated for a large set of fuels ranging from methane to iso-octane and one-ring aromatics using different flame configurations including homogeneous auto-ignition, laminar premixed flames and diffusion flames.

The final reaction mechanism is the KAUST PAH Mechanism 2 (KM2) [171] which includes species up to coronene $C_{24}H_{12}$ and comprises of 202 species and 1351 reactions in total. The reactions for small chemical species up to benzene were adopted from the USC II mechanism. The KM2 mechanism was validated in several premixed flames for the quantitative prediction of PAH concentrations. In addition, [174] assessed predictions of large PAH species by comparison with signals from an LII experiment, indicating that the KM2 mechanism is better suited for modelling larger PAH molecules as soot precursors than the ABF and BBF mechanisms.

In order to also account for the reduction in mixture enthalpy due to radiation by CO, CO_2, H_2O, CH_4 and soot, we include a radiation model based on the assumption of optical thinness [110]. Here, the temperature dependence of the Planck mean absorption coefficients is approximated by polynomials [175].

4.3.2 Soot kinetics

Nucleation

Frequently, the coalescence of two PAH molecules to form an incipient soot particle is considered as the main soot inception step [60–62]. Compared with semi-empirical acetylene-based models, PAH dimerisation constitutes an intermediate stage between the gaseous phase and the mature solid phase. In the present article, we consider the dimerisation of PAHs with two or more aromatic rings as a newly formed soot nucleus. For the BBP and KM2 mechanisms, the dimerisation rate is computed by assuming a Maxwell velocity distribution in the kinetic theory of molecular collisions such that the nucleation rate (in $[1/\mathrm{m}^3]$) is given by the collision frequency of two PAH molecules, PAH_j and PAH_k,

$$\dot{B}(\mathrm{PAH}_{jk}) = C_\mathrm{r}\gamma_{jk}N_\mathrm{A}d_{jk}^2\sqrt{\frac{8\pi R_\mathrm{J}T}{W_{jk}}}[\mathrm{PAH}_j][\mathrm{PAH}_k], \tag{4.6}$$

where N_A denotes Avogadro's number, R_J is the gas constant (in $[\mathrm{kmol}-\mathrm{K/kJ}]$) and d_{jk} indicates the mean diameter of the molecules PAH_j and PAH_k. W_{jk}, moreover,

represents the equivalent molar mass of PAH_j and PAH_k,

$$W_{jk} = \frac{W_j W_k}{W_j + W_k}. \tag{4.7}$$

and square brackets indicate molar concentration (in $[\mathrm{kmol/m^3}]$). The PAH species and the associated dimerisation efficiencies γ_i are chosen based on the original articles by Blanquart and Pitsch [61] and Wang et al. [62]. We maintain the custom that only the self collisions of a series of PAH molecules are considered in the BBP chemistry, whereas also heterogeneous nucleation involving different PAHs is accounted for in the KM2 chemistry. Here, the collision efficiencies γ_{jk} for the heterogeneous dimerisation rates are computed as the square root of product of the associated single species collision efficiencies.

$$\gamma_{jk} = \begin{cases} \gamma_j & \text{if } i = j \\ \sqrt{\gamma_j \gamma_k} & \text{otherwise } i \neq j \end{cases} \tag{4.8}$$

The correction constant C_r in Eq. 4.6 is set to 1.0 for the BBP mechanism [61] and to 0.127 for the KM2 mechanism [62]. As reference, Table 4.2 summarises the PAH molecules that are included in the dimerisation step for either reaction mechanism along with the molar masses M_i and single species collision efficiencies γ_i. This table also includes the species and parameters for the ABF mechanism. Contrary to Appel et al. [60], we do not only include the dimerisation of pyrene, but, for consistency with the BBP chemistry, also the dimerisation of those PAHs which the ABF and BBP mechanisms have in common.

Within the scope of a finite volume discretisation in v, the contribution of nucleation to the temporal rate of change of number density on the ith finite volume cell $[v_{i-1}, v_i]$ with width $\Delta v_i = v_i - v_{i-1}$ is evaluated as

$$\dot{B}_i = \sum_j \sum_{k \leq j} \frac{1}{\Delta v_i} \int_{v_{i-1}}^{v_i} \dot{B}(\mathrm{PAH}_{jk}) \delta(v - v(\mathrm{PAH}_{jk}))\, dv, \tag{4.9}$$

where $v(\mathrm{PAH}_{jk})$ is the volume of a dimer formed from PAH_j and PAH_k.

Surface growth and condensation

Following Appel et al. [60], soot particles grow according to the hydrogen abstraction and acetylene addition (HACA) mechanism. Here, surface reactions occur on active

Species	Molar mass M_i [kg/kmol]	Name	Collision efficiency γ_i		
			ABF	BBP [61]	KM2 [62]
$C_{10}H_8$	128.17	Naphthalene	0.0010	0.0010	–
$C_{12}H_8$	152.20	Acenaphthylene	0.0030	0.0030	–
$C_{12}H_{10}$	154.21	Biphenyl	0.0085	0.0085	–
$C_{14}H_{10}$	178.24	Phenathrene	0.0150	0.0150	–
$C_{16}H_{10}$	202.26	Pyrene	0.0250	0.0250	0.006
		Acephenanthrylene	–	0.0250	–
		Fluoranthene	–	0.0250	–
$C_{18}H_{10}$	226.28	Cyclo[cd]pyrene	0.0390	0.0390	–
		1-Ethynyl pyrene	–	–	0.010
		2-Ethynyl pyrene	–	–	0.010
		4-Ethynyl pyrene	–	–	0.010
$C_{20}H_{12}$	252.31	Benzo(a)pyrene	–	–	0.011
		Benzo(e)pyrene	–	–	0.011
$C_{22}H_{12}$	276.34	Benzo(ghi)perylene	–	–	0.014
$C_{24}H_{12}$	300.36	Coronene	–	–	0.020

Table 4.2 List of PAH species that are involved in dimerisation and surface condensation for three chemical reaction mechanisms.

sites that are distributed across the surface of a particle. These sites may either be associated with hydrogen atoms bonded to carbon atoms or radical sites on dehydrogenated carbon atoms. The number density $C_{soot} - H$ of the first type of sites is estimated to remain constant at 2.3×10^{19} based on the diameter of a benzene ring and the distance between PAH layers in soot [19]. The number density of radical sites $C_{soot}\cdot$, on the other hand, is rationalised by assuming that both types of sites are in steady state. Hydrogen is mainly abstracted by the H and OH radicals, but Hwang and Chung [176] and Wang et al. [62] emphasised that CH_3, C_3H_3 and C_2H may also play an important role in hydrogen abstraction.

$$C_{soot} - H + CH_3 \quad \Leftrightarrow \quad C_{soot}\cdot + CH_4 \tag{4.10}$$

$$C_{soot} - H + C_3H_3 \quad \Leftrightarrow \quad C_{soot}\cdot + C_3H_4 \tag{4.11}$$

$$C_{soot} - H + C_2H \quad \Leftrightarrow \quad C_{soot}\cdot + C_2H_2 \tag{4.12}$$

A complete list of the enhanced HACA mechanism including surface reaction rates can be found in Supplementary Material 2 of Wang et al. [62]. In order to model the experimentally observed dependence of reactive sites on particle size [31, 32] and temperature [33, 34], Frenklach and Wang [19] introduced the fraction α of active surface sites. In the past, α has been used to adjust the soot growth rate at

high temperatures; recently, values and submodels for α have been summarised by Veshkini et al. [177]. In this article, we consider α to be temperature dependent and adopt the functional form proposed by Guo et al. [75]. The coefficients in this representation are determined by manual adjustment in such a way that the experimental measurements of the line-of-sight integrated soot volume fraction are well reproduced in the ethylene flames, see Table 4.3.

Reaction mechanism	C_r	Coefficients in $\alpha(T) = \beta_u \exp(T_u/T)$	
		β_u	T_u
ABF	1.0	0.0095	9000
BBP	1.0	0.0037	9000
KM2	0.127	0.0025	9000

Table 4.3 Correction constant C_r in the PAH-based nucleation rate (Eq. 4.6): temperature dependency of the fraction of active surface sites $\alpha = \alpha(T)$ in the HACA mechanism for the three different chemical reaction mechanisms we consider here.

Particularly at low temperatures, soot surface growth is also enhanced by the direct condensation of PAHs onto the particle surface. Unlike the chemical surface reactions in the HACA mechanism, PAH condensation involves the collision and physical combination of a PAH molecule and a soot particle that is independent of active surface sites. In our growth rate model, all PAH molecules that contribute to the nucleation step may condense onto the surface of a soot particle with the same collision rate γ_i and correction factor Cr (Tables 4.2 and 4.3). The rate of increase in soot mass per surface area (in $[\mathrm{kg/m^2 - m^3}]$) due to PAH condensation may be computed according to

$$\dot{R}(\mathrm{PAH}) = C_\mathrm{r} \sum_i \gamma_i \sqrt{\frac{R_\mathrm{J} T}{2\pi M_i}} [\mathrm{PAH}_i] M c_i \tag{4.13}$$

where Mc_i (in [kg/kmol]) denotes the carbon weight per mole for PAH_i.

The cumulative volumetric growth rate encompasses contributions from the enhanced HACA mechanism for acetylene-based growth and oxidation as well as the the PAH condensation process

$$G(v, \mathbf{Y}) = \frac{A_{\mathrm{s},v}}{\rho_\mathrm{s}} \left[\dot{R}(\mathrm{HACA}) + \dot{R}(\mathrm{PAH}) \right], \tag{4.14}$$

where $\dot{R}(\mathrm{HACA})$ represents the surface-specific soot growth rate of the enhanced HACA mechanism, $\rho_\mathrm{s} = 1800\,\mathrm{kg/m^3}$ is the density of solid soot and $A_{\mathrm{s},v}$ denotes

the soot surface density. If the growth rate $G(v, \mathbf{Y})$ is negative, then this indicates that the oxidising species O_2 and OH dominate the soot surface reactions.

Particle coagulation

The collision kernel in the coagulation term for the free molecular and continuum regimes, respectively, may be described according to [147]

$$\beta^{\mathrm{fm}}(v_i, v_j) = 2.2\sqrt{\frac{\pi k_{\mathrm{B}} T}{\rho_{\mathrm{s}}(v_i + v_j)}}\left(d(v_i) + d(v_j)\right)^2, \tag{4.15}$$

$$\beta^{\mathrm{c}}(v_i, v_j) = \frac{2k_{\mathrm{B}} T}{3\mu}\left(\frac{C(v_i)}{d(v_i)} + \frac{C(v_j)}{d(v_j)}\right)\left(d(v_i) + d(v_j)\right), \tag{4.16}$$

where k_{B} denotes Boltzmann's constant, $d(v)$ represents either the diameter of a spherical particle $d_{\mathrm{p}}(v)$ or the diameter of gyration of an aggregate $d_{\mathrm{g}}(v)$ (Eq. 4.19 and 4.22 below) and $C(v)$ is a function that encapsulates the Knudsen number dependency

$$C(v) = 1 + 1.257 \times \mathrm{Kn}(v). \tag{4.17}$$

The diameter of gyration d_{g} is a parameter used to measure the mass distribution in a fractal aggregate. We employ the free-molecular coagulation kernel β^{fm} for $\min(\mathrm{Kn}(v_i), \mathrm{Kn}(v_j)) > 10$ and the continuum kernel for $\max(\mathrm{Kn}(v_i), \mathrm{Kn}(v_j)) < 0.1$. In between these two extreme cases, the transition kernel β^{tr} is used [178],

$$\beta^{\mathrm{tr}}(v_i, v_j) = \frac{\beta^{\mathrm{fm}}(v_i, v_j)\beta^{\mathrm{c}}(v_i, v_j)}{\beta^{\mathrm{fm}}(v_i, v_j) + \beta^{\mathrm{c}}(v_i, v_j)}. \tag{4.18}$$

4.3.3 Soot morphology

As previous research on soot morphology [179–182] and our TEM observations indicate, soot particles tend to assemble into aggregates of fractal 'grape-like' shape, consisting of many connected spherical primary particles. In order to account for fractal shapes while maintaining a one-dimensional particle property space, we assume a soot particle to be spherical in shape if its volume is less than a critical value v_{c1}. On the other hand, it is assumed to be an aggregate consisting of several primary particles with identical volumes v_{c1} if the volume of this aggregate is greater than another critical value v_{c2}. By examining TEM images of thermophoretically sampled particles (Figure 4.8), we determined an average primary particle size of

$d_{\mathrm{p,a}} = 30.8$ nm which agrees well with the average size of 29 nm reported by Tian et al. [179]. For this reason, we define the first critical size to be the average size of primary particles $v_{\mathrm{c1}} = v_{\mathrm{p,a}}$; concomitantly, the second critical size is taken as $v_{\mathrm{c2}} = 10v_{\mathrm{p,a}}$. The number of primary particles in a fractal-like aggregate can be estimated from the power law [13]

$$N_{\mathrm{p}}(v) = \frac{v}{v_{\mathrm{p,a}}} = k_{\mathrm{f}} \left(\frac{d_{\mathrm{g}}(v)}{d_{\mathrm{p,a}}} \right)^{D_{\mathrm{f}}}, \tag{4.19}$$

where v represents the volume of an aggregate, $d_{\mathrm{g}}(v)$ denotes the diameter of gyration, $k_{\mathrm{f}} = 1.94$ is the fractal prefactor [181] and $D_{\mathrm{f}} = 1.8$ is the fractal dimension [183]. For large non-spherical or elongated aggregates, the diameter of gyration and the hydrodynamic diameter are related according to [184]

$$\frac{d_{\mathrm{g}}}{d_{\mathrm{h}}} = 0.775. \tag{4.20}$$

Within an aggregate, neighbouring primary particles are assumed to be in point contact such that the surface area $A_{\mathrm{s}}(v)$ of an aggregate is estimated as [183]

$$A_{\mathrm{s}}(v) = A_{\mathrm{p,a}} N_{\mathrm{p}}(v) \left(1 - \phi C_{\mathrm{ov}} \left(1 - \frac{1}{N_{\mathrm{p}}(v)} \right) \right). \tag{4.21}$$

Here, $A_{\mathrm{p,a}}$ represents the surface area of a spherical particle with diameter $d_{\mathrm{p,a}} = 30.8$ nm, $C_{\mathrm{ov}} = 0.15$ is an overlapping parameter for neighbouring primary particles and ϕ is defined as the coordination number (number of contacts per primary particles), approximated as 1.3 for large $N_{\mathrm{p}}(v)$.

Figure 4.8 shows that soot particles are initially liquid-like and carbonise progressively, in agreement with the recent results of Kholghy et al. [28]. At heights above the burner of 20 mm in the non-smoking flame and 30 mm in the incipient smoking flame, the liquid-like particles are generally larger than a primary particle and appear to possess a shape that is intermediate between a spherical particle and a fractal aggregate. For this reason, we assume that the volume of particles with an intermediate shape ranges in $[v_{\mathrm{c1}}, v_{\mathrm{c2}}] = [v_{\mathrm{p,a}}, 10v_{\mathrm{p,a}}]$ and treat the associated morphological diameters $d_{\mathrm{h}}(v)$ and $d_{\mathrm{g}}(v)$ in a special way. For example, rather than using the statistically empirical expression 4.19 and 4.20, the diameter of gyration and the hydrodynamic diameter in the size range $[v_{\mathrm{p,a}}, 4v_{\mathrm{p,a}}]$ are computed based on the theoretical expressions for primary particles, dimers, trimers and tetramers derived by Sandkühler et al. [152] and fitted as cubic polynomials. For the size

range $[4v_{\mathrm{p,a}}, 10v_{\mathrm{p,a}}]$, by contrast, linear interpolations based on the values at the two boundaries are used to maintain continuity over the whole size domain.

$$d_{\mathrm{g}}(v) = \begin{cases} d_{\mathrm{p,a}}\big[-2.98\times10^{67}\cdot N_{\mathrm{p}}^3 + 2.90\times10^{45}\cdot N_{\mathrm{p}}^2 - 6.68\times10^{22}\cdot N_{\mathrm{p}} + 1.45\big], \\ \qquad\qquad\qquad\qquad\qquad\qquad v_{\mathrm{p,a}} < v < 4v_{\mathrm{p,a}} \\ d_{\mathrm{p,a}}\big[1.20\times10^{22}\cdot(v - 4v_{\mathrm{p,a}}) + 1.38\big], \qquad 4v_{\mathrm{p,a}} < v < 10v_{\mathrm{p,a}} \end{cases} \tag{4.22}$$

$$d_{\mathrm{h}}(v) = \begin{cases} d_{\mathrm{p,a}}\big[-4.75\times10^{67}\cdot N_{\mathrm{p}}^3 + 4.64\times10^{45}\cdot N_{\mathrm{p}}^2 - 1.10\times10^{23}\cdot N_{\mathrm{p}} + 1.35\big], \\ \qquad\qquad\qquad\qquad\qquad\qquad v_{\mathrm{p,a}} < v < 4v_{\mathrm{p,a}} \\ d_{\mathrm{p,a}}\big[1.85\times10^{22}\cdot(v - 4v_{\mathrm{p,a}}) + 1.51\big], \qquad 4v_{\mathrm{p,a}} < v < 10v_{\mathrm{p,a}} \end{cases} \tag{4.23}$$

In addition, the surface area of a particle in this intermediate size range is also fitted based on the two boundary values and the 2/3 power of its volume, thus,

$$A_{\mathrm{s}}(v) = A_{\mathrm{p,a}}\left[1.72\times N_{\mathrm{p}}^{\frac{2}{3}} - 0.72\right], \quad v_{\mathrm{p,a}} < v < 10v_{\mathrm{p,a}}. \tag{4.24}$$

As reference, the morphological parameters of primary soot particles, aggregates and particles with an intermediate shape are summarised in Table 4.4.

Geometric parameter [1]	Symbol	$v \le v_{\mathrm{p,a}}$	$v_{\mathrm{p,a}} < v < 10v_{\mathrm{p,a}}$	$10v_{\mathrm{p,a}} \le v$
Diameter of gyration	d_{g}	$(6v/\pi)^{1/3}$	Eq. 4.22	$d_{\mathrm{p,a}}(k_{\mathrm{f}}v/v_{\mathrm{p,a}})^{1/D_f}$
Hydrodynamic diameter	d_{h}	$= d_{\mathrm{g}}$	Eq. 4.23	$d_{\mathrm{g}}/0.775$
Surface area	A_s	πd_{g}^2	Eq. 4.24	Eq. 4.21

Table 4.4 Summary of the geometric parameters we employ to describe the morphology of soot particles of a range of particle volumes v.

4.4 Modelling of LIF, ELS and LOSA signals

The central aspect of our model validation in Section 4.5 is to compare 'predicted laser diagnostic signals' computed from model predictions of major chemical species and the soot size distribution with laser diagnostic measurements, as advocated by

[1] Here, the diameter of gyration d_{g} and the hydrodynamic diameter d_{h} are distinguished. d_{g} plays an important role in the collisional kinetics of soot and is defined as the mass weighted average distance between the centre of a molecule and its mass elements. d_{h}, by contrast, controls the spatial diffusion of particles and is defined as the diameter of a hard sphere that diffuses at the same rate as the molecule under consideration. In general, the values of d_{g} and d_{h} are of the same order of magnitude.

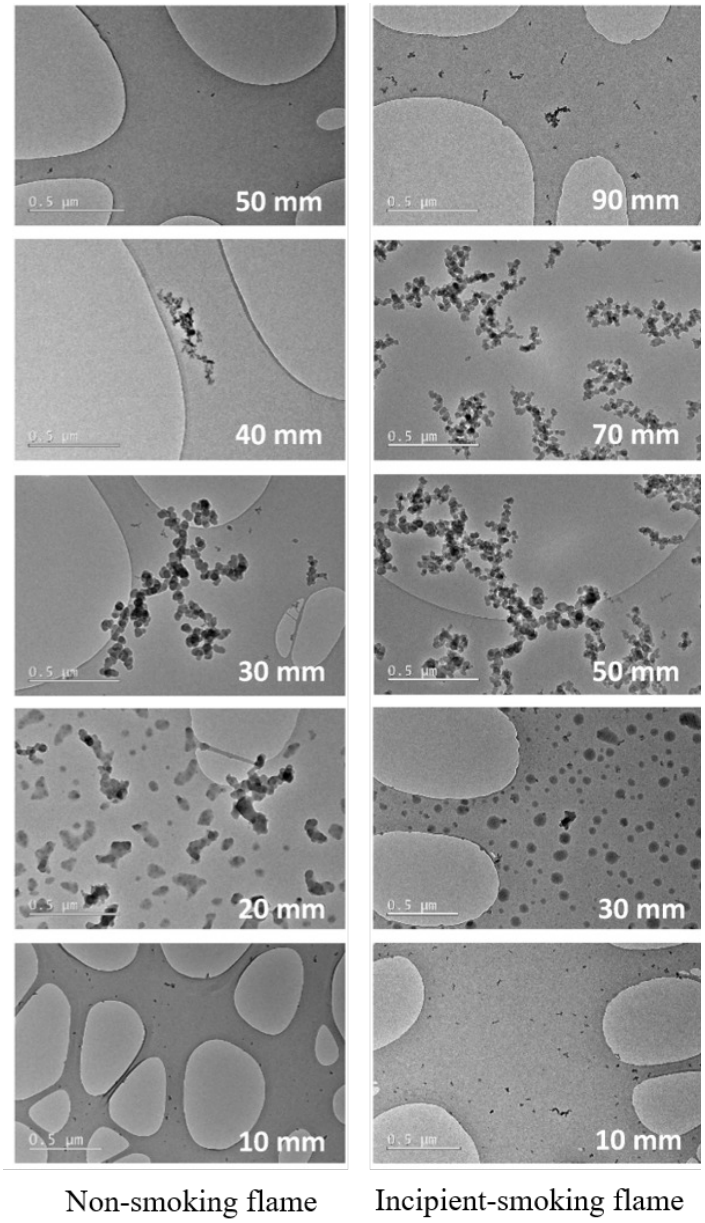

Fig. 4.8 TEM micrographs of thermophoretically sampled soot particles on the centreline in the non-smoking and incipient smoking flames. Each image covers approximately 1.5×2 μm and soot particles are supported on a holey carbon film.

Connelly et al. [167]. The intensity of the LIF signal, for instance, may be estimated according to [185]

$$S^{\mathrm{OH-LIF}} \propto I_{\mathrm{inc}} n_{\mathrm{OH}} \sigma_{\mathrm{A}} Q_{\mathrm{Y}}, \tag{4.25}$$

where I_{inc} is the intensity of the incident laser beam with wavelength λ and n_{OH} represents the number concentration of OH molecules. Additionally, σ_{A} and Q_{Y} denote the molecular absorption cross section and the quantum yield, respectively. Since both σ_{A} and Q_{Y} are functions of λ and the local temperature T, their product is modelled in terms of the normalised Boltzmann fraction of electrons in the ground level $f_{v,J}(T)$ for a transition of quantum numbers v, J at temperature T and corrected by the collisional quenching of OH radicals by other major species (N_2, O_2, H_2O, H_2, CO_2, CO, H and OH) using the quenching rates $w_i(T)$ of Tamura et al. [186]. Assuming that spontaneous emission is negligible compared with quenching, we hence calculate the normalised OH-LIF signal as

$$S^{\mathrm{OH-LIF}} \propto [\mathrm{OH}] \frac{f_{v,J}(T)}{w(T)}, \tag{4.26}$$

For our purposes, the temperature dependence of the Boltzmann fraction is determined approximately with the aid of LIFBASE [187]

$$f_{0,8}^{\mathrm{OH}}(T) \approx 1.206 \times 10^{-10} T^3 - 9.163 \times 10^{-7} T^2 + 2.146 \times 10^{-3} T - 0.586 \tag{4.27}$$

and the local quenching rate is obtained as

$$w(T) = \sum_i X_i w_i(T), \tag{4.28}$$

where X_i denotes the mole fraction of the colliding species i and w_i is the corresponding quenching rate.

The ELS signal intensity S^{ELS} is modelled according to the Rayleigh-Debye-Gans theory of light scattering by fractal aggregates (RDG-FA). Since we consider molecular light scattering to be negligible, S^{ELS} is proportional to both the number density and the scattering cross-section $\sigma_{\mathrm{s}}(v)$ of soot particles. The scattering cross-section may be computed according to [181]

$$\sigma_{\mathrm{s}}(v) = k_f \begin{cases} k^4 F(m) \left(\frac{d(v)}{2}\right)^6 & \text{For primaries} \\ k^4 F(m) S(q) N_{\mathrm{p}}(v)^2 \left(\frac{d_{\mathrm{p,a}}}{2}\right)^6 & \text{For aggregates} \end{cases}, \tag{4.29}$$

where k_f is the fractal prefactor, k denotes the wavenumber of the incident light and $F(m) = |(m^2-1)/(m^2+1)|^2$ is a function of the complex refractive index of soot ($m = 1.57 - 1.56\mathrm{i}$ [188]). $S(q)$, moreover, represents a structure factor which adopts different expressions for the Rayleigh, Guinier and power-law scattering regimes [38] depending on the size parameter qR_g

$$S(q) \propto \begin{cases} 1 & \text{if } qR_g < 0.1 \\ 1 - \frac{(qR_g)^2}{3} & \text{if } 0.1 \leq qR_\mathrm{g} \leq 1 \\ (qR_\mathrm{g})^{-D_f} & \text{otherwise} \end{cases}, \tag{4.30}$$

where $q = 2k\sin(\theta/2)$ is the norm of the scattering wave vector, θ is the angle of observation and R_g is half of the diameter of gyration. The relative ELS signal is thus calculated based on the soot PSD as

$$S^\mathrm{ELS} \propto \int_0^\infty N(v)\sigma_\mathrm{s}(v)\,\mathrm{d}v. \tag{4.31}$$

The Beer-Lambert law describes how a laser beam is attenuated as it travels through a flame for a distance L due to a combination of absorption and scattering by soot particles. Based on this law, the LOSA signal along the line of sight (spatial coordinate s, $s \in [0, L]$) may be expressed in terms of the soot volume fraction $f_\mathrm{v}(s)$ according to

$$\int_0^L f_\mathrm{v}(s)\,\mathrm{d}s = -\frac{\lambda}{6\pi\,\mathrm{Im}\left(\frac{m^2-1}{m^2+1}\right)} \ln\left(\frac{I}{I_0}\right), \tag{4.32}$$

where λ is the laser wavelength, I/I_0 is the relative attenuation signal and $\mathrm{Im}(\cdot)$ indicates the imaginary part of a complex number.

4.5 Results and Discussion

4.5.1 Laser diagnostic signals

In this section, we compare the measured OH-PLIF, ELS and LOSA signals with the corresponding model predictions.

The line-of-sight integrated soot volume fraction (ISVF) is related to the LOSA signal according to Eq. 4.32. For this formulation, Tian et al. [41] reported measurement errors of up to 40 %. These are indicated by error bars in Figure 4.9, where the measured and predicted line-of-sight ISVF along the centreline are compared for the

non-sooting and incipient sooting flames. Here, the modelled signals correspond qualitatively well to the LOSA measurements for all three reaction mechanisms, although the maximum is noticeably underpredicted. In the non-smoking flame, the three reaction mechanisms lead to quantitatively similar predictions; however, compared with experimental data, the line-of-sight ISVF obtained from the three chemistries decay slowly. In the incipient sooting flame, the differences in the downstream decay of the three model predictions are less pronounced, albeit a minor discrepancy of the slightly slower decay of the line-of-sight ISVF obtained from the KM2 mechanism compared with the ABF and BBP chemistries. For the three mechanisms, the line-of-sight ISVF decrease at a similar rate beyond the maximum, but the reduction commences about 10 mm further upstream in the ABF results. The BBP mechanism appears to yield intermediate results that are characterised by a late onset of signal decay and slightly larger decay rate. In the early stages of soot formation far upstream, we also observe minor deviations between the three predicted signals, emphasising that the choice of chemical reaction mechanism influences the fast nucleation and oxidation processes.

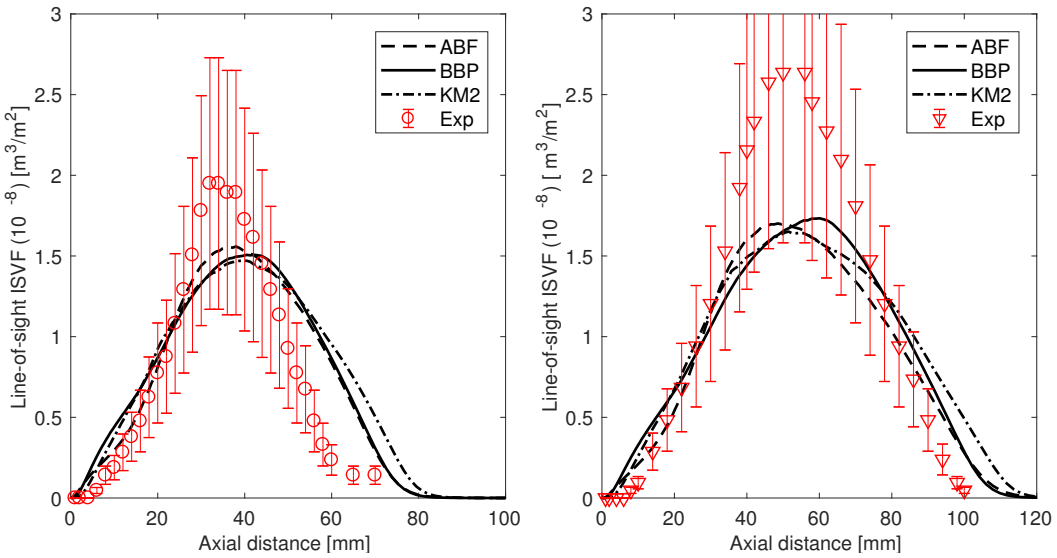

(a) Non-smoking flame (b) Incipient smoking flame

Fig. 4.9 Comparison between the predicted ISVF and the ISVF obtained from discrete line-of-sight attenuation measurements.

Complementary to Figure 4.9, Figure 4.10 depicts predicted and measured radial profiles of the line-of-sight ISVF for the non-smoking and incipient smoking flames, respectively. Similar to the previous figure, LOSA measurements are supplemented by error bars corresponding to an error of 40 %. The LOSA measurements indicate

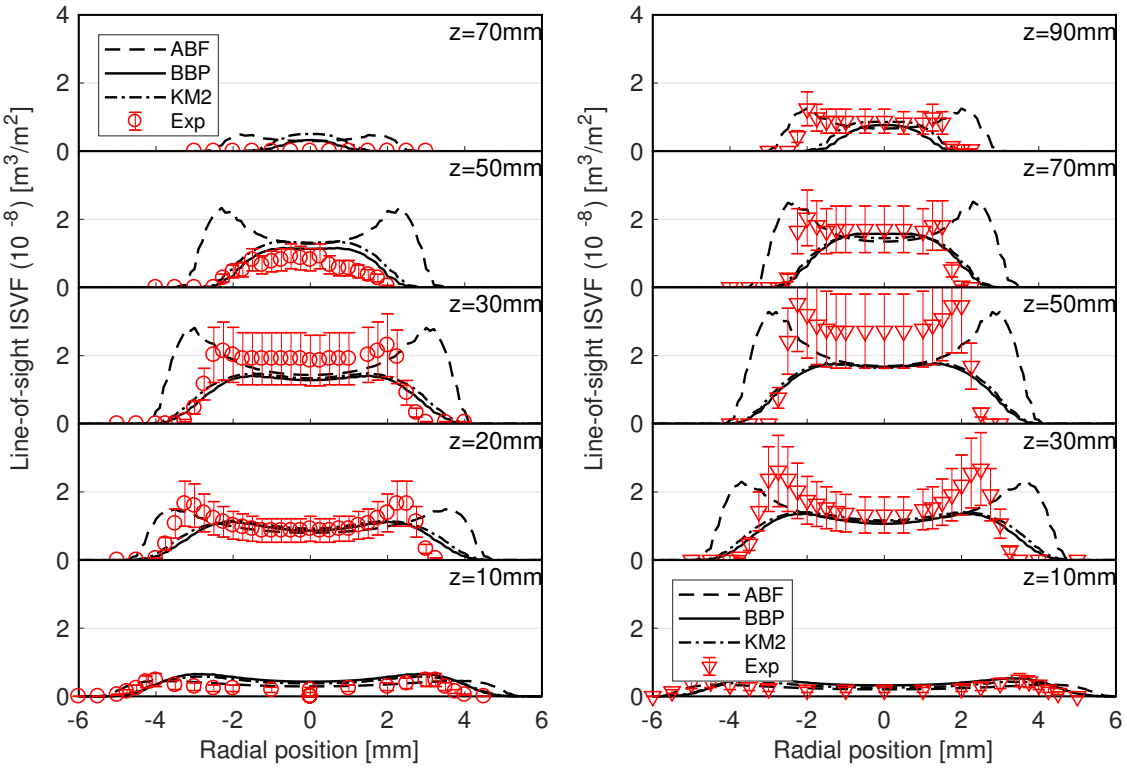

(a) Non-smoking flame (b) Incipient smoking flame

Fig. 4.10 Comparison of predicted and measured radial profiles of the ISVF.

the presence of two sooty flame wings which we also observe in the signals obtained from the ABF chemistry, albeit at slightly further radial locations. Quantitatively, the distance between the two sooty wings is overpredicted in the ABF simulations by about 2 mm. For the BBP and KM2 reaction mechanisms, by contrast, the radial increase in line-of-sight ISVF away from the centreline and subsequent drop are significantly less pronounced and the radial profiles are much smoother. Downstream, the prominence of the sooty wings seems to disappear completely, leaving a maximum in the line-of-sight ISVF on the centreline. If we disregard, however, the representation of the sooty wings and focus on the region near the centreline, then the signals predicted from all three reaction mechanisms correspond rather well quantitatively with the LOSA measurements, at least to within the measurement uncertainty.

The left panels in Figure 4.11 show the radial profiles of the normalised ELS signal at several downstream positions for the two flame configurations. As above, the measurements are compared with predicted signals obtained from simulations with the ABF, BBP and KM2 reaction mechanisms. The radial locations at which the

ELS signal peaks are correctly reproduced by the BBP and KM2 mechanisms, while the maxima are slightly displaced radially outwards for the ABF signals, echoing our observation from Figure 4.10. Additionally, the experimental ELS signal indicates that a significant amount of light is scattered close to the centreline in between the sooty flame wings. This is also reflected in the BBP and KM2 predictions, but seems to be absent in the ABF simulation. Analysing the axial changes in the ELS profiles, we find that the axial location of maximum ELS signal is well predicted by the ABF mechanism in the non-smoking flame, but that the signal peaks about 20 mm upstream in the incipient sooting case. On the other hand, the axial locations of maximum ELS signals can be accurately captured for the BBP and KM2 mechanisms; however, the ELS signals are noticeably overestimated in other cross-sections.

The right panels in Figure 4.11 depict measured and predicted radial profiles of OH-LIF signals which we may contrast with the ELS signal from soot in the left panels. Throughout the flames, the predicted normalised OH-LIF signals correspond qualitatively well with the experimental observations. As the axial distance increases, the OH-LIF peaks seem to migrate towards the centreline until they overlap with the sooty flame wings. For both flames, the measured OH-LIF profiles are slightly more skewed towards the centreline at the downstream distances than the predicted profiles and OH is also detected near the flame centre. Physically, soot forms and grows on the rich side of the flame and is oxidised (mainly by OH) in the vicinity of stoichiometric conditions. This rationale is reflected in the HACA mechanism for soot growth and oxidation and implies that OH rapidly consumes soot such that both are largely precluded from coexisting. Indeed, for the ABF and KM2 mechanisms, the ELS and OH-LIF profiles in Figure 4.11 are mainly non-overlapping, except by a small amount at furthest downstream locations. In the BBP predictions, soot and OH are seen to overlap by a larger fraction downstream, albeit not quite as much as indicated by the experimental measurements near the centreline and close to the flame tip.

Further to Figure 4.11, 4.12 and 4.13 show contour plots of the predicted and measured normalised ELS and OH-PLIF signals in the non-smoking and incipient smoking flames. The experimental ELS contours indicate that the two sooty wings appear approximately 15 mm above the nozzle exit plane and disappear at axial distances of about 60 mm and 95 mm, respectively. Although the sooty wings are also prominent in the predicted ELS signals, the three different gas phase mechanisms lead to qualitative differences. For the BBP and KM2 mechanisms, for instance, soot formation seems to commence further upstream than in the experimental records

and soot persists until the wings converge on the centreline near the flame tip. Additionally, we observe that the sooty wings are thicker, eliciting a strong ELS signal from the centreline upstream of the flame tip. This is quite in contrast to the ELS contours obtained from the ABF mechanism. Here, the sooty wings are almost as sharp as indicated by the experimental measurements; however, radially, the wings are shifted outwards and there does not appear to be any light scattering near the centreline. These observations on the contour plots are in line with our previous discussion of the corresponding radial profiles in Figure 4.11.

Apart from the downstream tails, the experimental ELS signals are almost completely enveloped by the OH-PLIF signals. The experimental measurements indicate that OH-PLIF wings emanate from the edges of the fuel tube and convene on the centreline about 70 mm and 100 mm above the burner exit plane, respectively. Although in the incipient smoking flame the predicted OH-PLIF tip is approximately 10 mm to 15 mm further downstream than in the experimental image, we consider the model predictions to be in reasonably good agreement with the measurements. For the BBP and KM2 mechanisms, the OH-PLIF signals near the flame tip are slightly sharper and more similar in appearance to the experimental record than the ABF signals, possibly owing to weaker cross-centreline diffusion.

Using the TEM images of soot samples, we can manually achieve the average primary particle diameters on the centreline of the flame. Therefore, we also calculate the average primary particle diameters from the numerical results. Since no primary particle smaller than 5 nm were discovered in the experiment, probably due to the resolution of the thermopheretical instrument, we simply subtract the particles smaller than 5 nm in the simulation for the statistics of average primary particle size. It is hard to conclude a favorable predicted results comparing with the measured one in Fig. 4.14. However, two promising aspects should be pointed out for the simulations with KM2 mechanism. First of all, peak values in the TEM samples occur at 20 mm and 30 mm HAB for the two flame conditions, and only 15 - 20 mm upstream than the simulations. Second, the predictions with BBP and KM2 mechanisms are able to achieve the equivalent peak average size of primary particles to the measurement. These two aspects ensure the surface area of a soot particle, which determines the surface growth of soot, is in a range of physical rationale. Another interesting issue is that the average primary particle size by KM2 mechanism climbs to the peak platform at about 10 mm upstream than the BBP mechanism for the reason that the soot precursors are larger based on the dimerisation of A4 - A7 species in the KM2 mechanism.

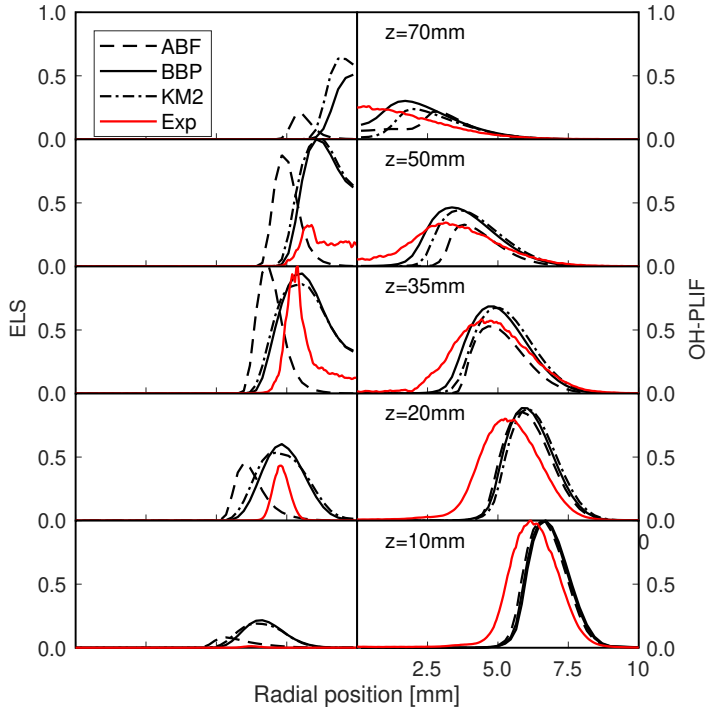

(a) Non-smoking flame

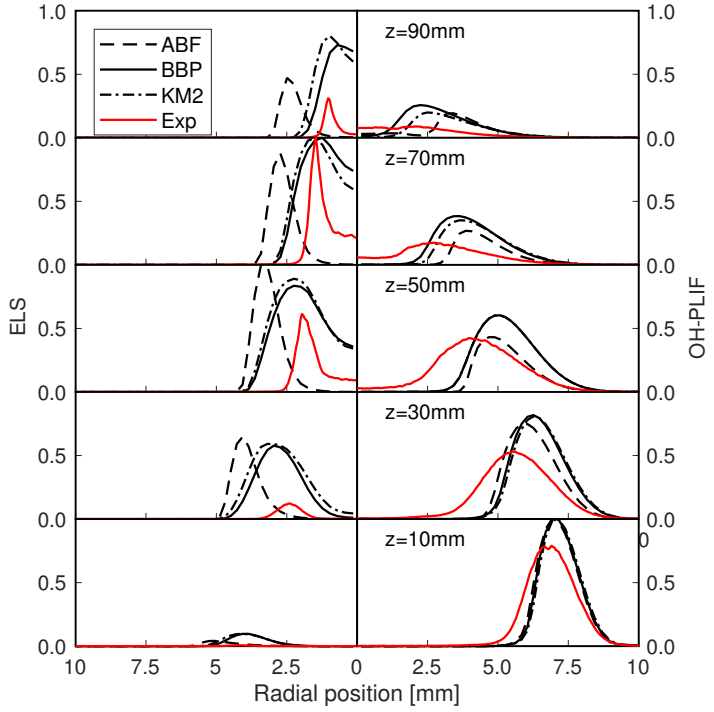

(b) Incipient smoking flame

Fig. 4.11 Radial profiles of the ELS and OH-PLIF signals at different axial locations for the sooting and incipient sooting flames.

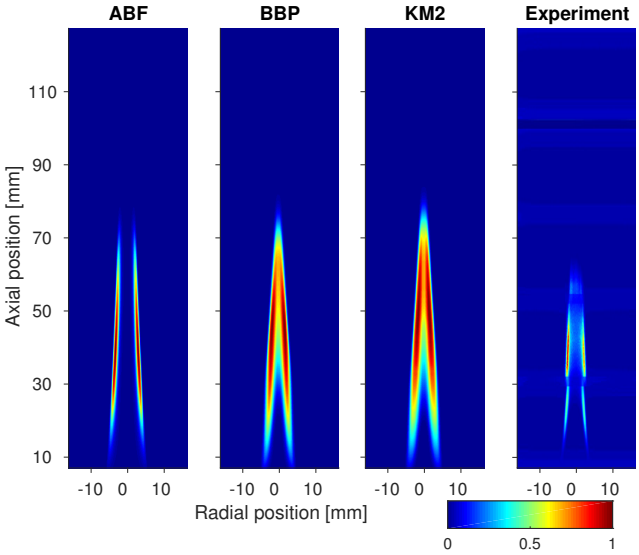

(a) ELS signals

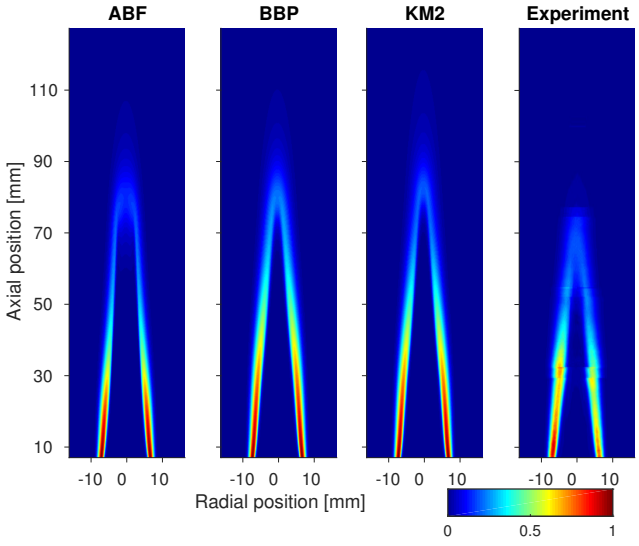

(b) OH-PLIF signals

Fig. 4.12 Contour plots of the ELS and OH-PLIF signals at different downstream locations in the non-smoking flame

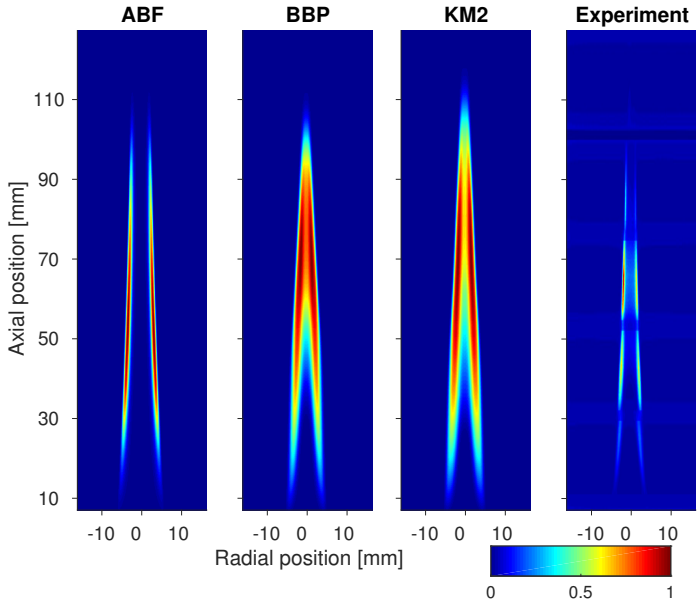

(a) ELS signals

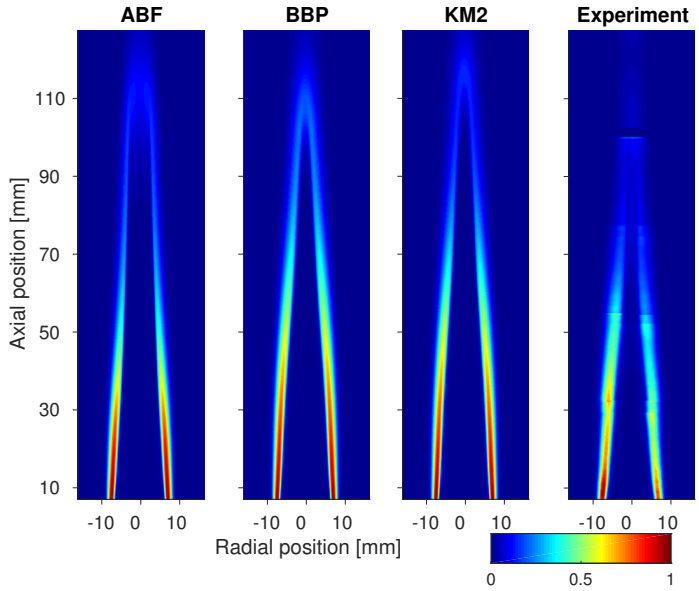

(b) OH-PLIF signals

Fig. 4.13 Contour plots of the ELS and OH-PLIF signals at different downstream locations in the incipient smoking flame

However, the causes of the major discrepancy should be carefully considered, preliminary illustrated as follows. First of all, if the growth rate could be larger in the early stage of soot formation while it became much smaller in the post-stage, which is the outcome of soot-aging, the primary particle size would increase to the maximum earlier and decay much faster. On the other hand, the limitations of the one-dimensional PBE naturally fails to conserve the number of primary particle during the process of coagulation, leading to the skewed surface area and the size of primary particles. As a consequence, the errors have been compensated in a certain extent by fitting the parameters of soot modelling to keep the integrated soot volume correct in this research.

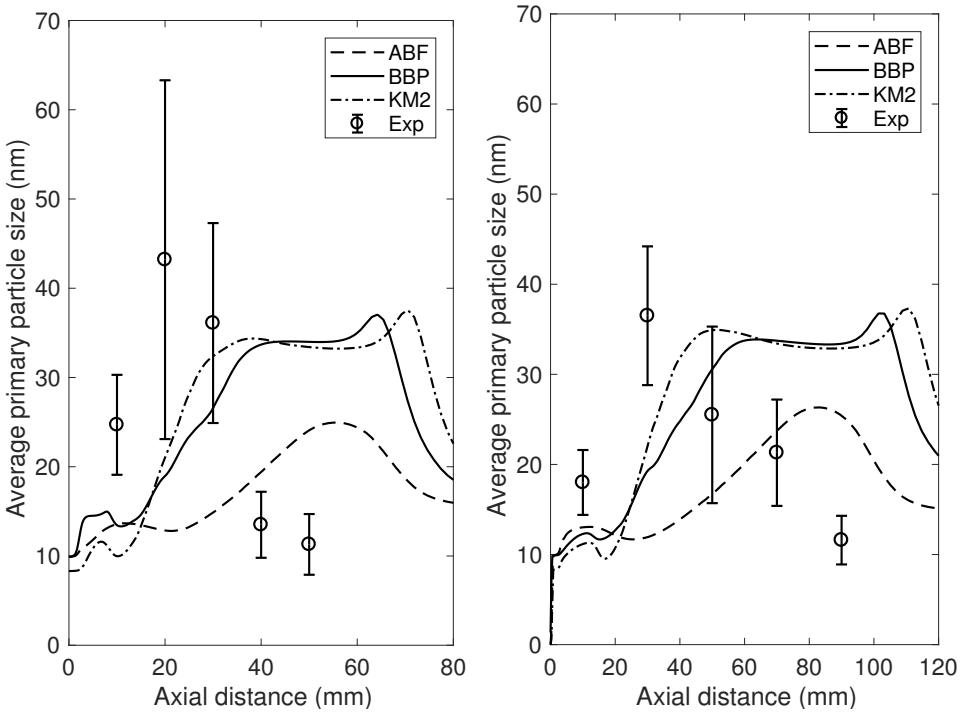

(a) Non-smoking flame (b) Incipient-smoking flame

Fig. 4.14 Comparison of axial average primary particle size profiles. Experimental data is based on the analysis of TEM images from soot samples.

In summary, our model predictions correspond reasonably well with the experimental laser diagnostic signals, although some discrepancies persist. In terms of the location and intensity of soot production, the PBE-based soot model is contingent upon the reaction mechanism used to describe the gas phase chemistry. In particular, the predictions obtained from the BBP and KM2 mechanisms reproduce the distance between the sooty flame wings very well. On the centreline, the experimental mea-

surements indicate that a small amount of soot is produced, but this is overestimated by the BBP and KM2 mechanisms and completely absent in the predictions obtained with the ABF chemistry.

Moreover, the differences in shape and magnitude of the predicted and measured ELS signals may be related to a limitation of the acetylene-based nucleation and growth kinetics. Near the centreline, where the acetylene concentration is very low, our model is likely to underpredict soot formation. Finally, the assumption that all aggregates consist of primary particles of the same size could affect the surface growth and coagulation processes by mis-estimating the surface area and fractal shape of the aggregates. This assumption may also have an impact on the spatial distribution of the predicted ELS signals.

4.5.2 Radial profiles of key variables controlling soot formation

In the present section, we turn to the analysis of the spatial distribution of key gas phase variables along with the nucleation, surface growth, condensation and oxidation rates they control. For brevity, model predictions are shown only for the incipient smoking flames, but we emphasise that the corresponding predictions for the non-smoking flame share similar features.

Since the HACA mechanism is mainly driven by temperature and C_2H_2 concentration, these two variables play an important role in determining not only the flame structure, but also the amount of soot produced. Figure 4.15(a) depicts radial profiles of temperature and C_2H_2 mole fraction at different heights above the burner exit. Beyond an axial distance of about 30 mm, the temperature profiles obtained from the ABF mechanism fall below the BBP and KM2 profiles by up to 200 K. The C_2H_2 profiles obtained from the three reaction mechanisms, by contrast, match for a slightly larger axial distance, up until about 50 mm above the burner exit. Further downstream, the BBP simulation indicates a more rapid decrease in C_2H_2 than we observe for the ABF and KM2 chemistries. By an axial distance of 90 mm, C_2H_2 has completely disappeared for the ABF and BBP mechanisms, whereas the KM2 profiles still indicate a small amount of C_2H_2 here. As soot growth thus persists longer, this may explain why the ELS signals predicted by the KM2 mechanism vanish further downstream than predicted by the ABF and BBP mechanisms (Figure 4.13(a)).

According to the soot nucleation and condensation models we adopt here (Sections 4.2 and 4.3), the presence of PAH species determines the formation of soot precursors and also reinforces the soot growth. Since A2 serves as the main species

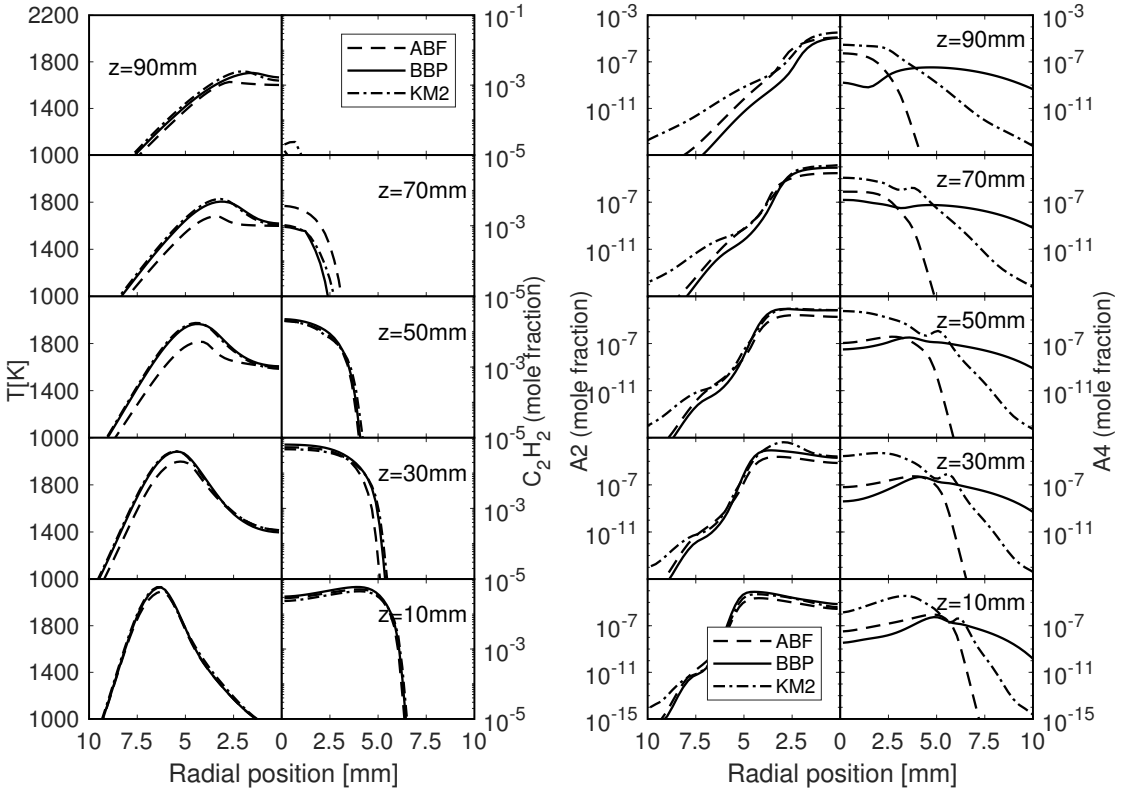

(a) Temperature (left) and C_2H_2 mole fraction (right)

(b) A_2 mole fraction (left) and A_4 mole fraction (right)

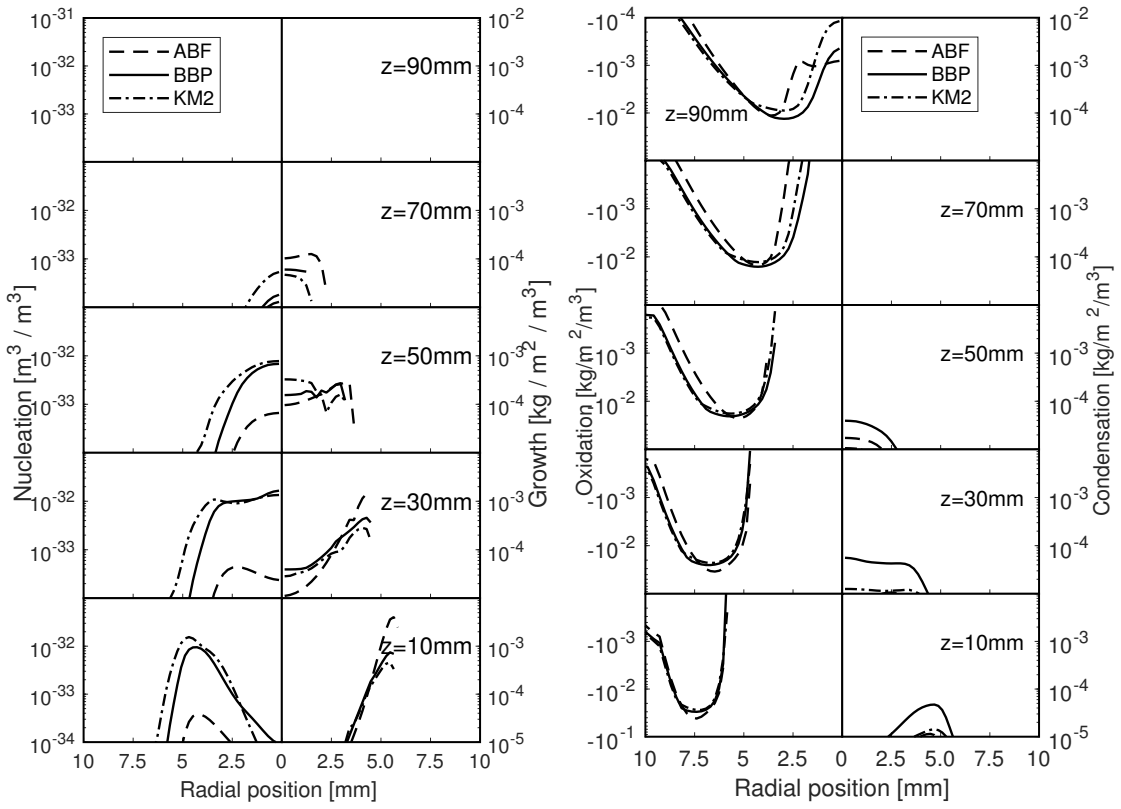

(c) Nucleation rate (left) and HACA surface growth rate (right)

(d) Oxidation rate (left) and PAH condensation rate (right)

Fig. 4.15 Radial profiles of key variables controlling soot formation at different downstream locations in the incipient smoking flame.

for PAH dimerisation and condensation in the ABF and BBP mechanisms, Figure 4.15(b) shows profiles of the A2 mole fraction along with A4. In the early to middle stages of soot formation (about 10 mm to 50 mm above the burner exit), the A2 mole fraction predicted by the BBP mechanism is about one or two orders of magnitude larger than that obtained from the ABF mechanism. By consequence, although the same formula is used for the nucleation rate with the ABF and BBP chemistries, we obtain significant differences in soot formation. The A4 mole fractions, on the other hand, are orders of magnitude lower than the A2 mole fractions in the ABF and BBP simulations, particularly in the central region of the flame. This is at odds with the KM2 results, where the A2 and A4 mole fractions take on similar values. Since the increased presence of large PAHs may contribute to the pool of soot precursors, Wang et al. [62] selected A4 to A7 as incipient species for the nucleation process. Additionally, the dimerisation of large PAHs is thought to play an important role in soot nucleation [7, 28]

Figure 4.15(c), moreover, depicts radial profiles of the nucleation and growth rates in the incipient smoking flame. Here, the profiles of nucleation rate correspond well with the spatial distribution of the PAHs in Figure 4.15(b), while the growth rate peaks in regions of high temperature and large C_2H_2 concentration. Interestingly, the nucleation rates computed from both the BBP and KM2 mechanisms using the parameters proposed by Blanquart and Pitsch [61] and Wang et al. [171] are one to two orders of magnitude larger than those obtained from the ABF chemistry, leading to different spatial distributions of light scattering soot. Yet, since the soot volume fraction is mainly controlled by surface growth, the α parameter in the HACA mechanism may be adjusted to restore consistency among the soot volume fraction profiles predicted by the three different simulations (Table 4.3). This adjustment is reflected by the similar levels of growth rates in Figure 4.15(c).

Finally, Figure 4.15(d) shows the specific surface oxidation rate due to OH and O_2 alongside the PAH surface condensation rate. The oxidation profiles coincide for the three different reaction mechanisms almost up to the flame tip, indicating that the spatial distributions of OH and O_2 are only slightly affected by a change in gas phase chemistry. The condensation rate is shown on the same scale as the surface growth and oxidation rates and we observe that PAH addition occurs predominantly close to the centreline, while C_2H_2 addition is stronger on the sooty flame wings. In comparison, the HACA surface growth appears to dominate over PAH condensation as evidenced by the two distinct sooty wings of the ELS signals (Figures 4.12(a) and 4.13(a)).

4.5.3 Sensitivity analysis on nucleation and growth rates

In the present section, we explore the sensitivity of the predicted line-of-sight ISVF and ELS signals with respect to the nucleation and growth rates. In Eqs. 4.6 and 4.13, the dimerisation and condensation rates are scaled by a correction factor of C_r. Similarly, the HACA surface growth rate is parameterised by the fraction of active sites α. In order to maintain the experimental levels of soot volume fraction, the changes in C_r and α are coordinated as indicated in Table 4.5. As base test case, we consider the incipient smoking flame using the BBP reaction mechanism because sufficient PAHs with a large molecular weight persist here (Figure 4.15(b)).

Case	C_r	α
Base	1.0	$0.0037 \times \exp(9000/T)$
Adjusted 1	0.1	$0.0062 \times \exp(9000/T)$
Adjusted 2	0.01	$0.0105 \times \exp(9000/T) \approx 1.0$

Table 4.5 Summary of the parameter sets (C_r, α) considered for a sensitivity analysis with respect to nucleation and growth rates.

The (C_r, α) parameter sets in Table 4.5 indicate that soot formation is much less sensitive to the nucleation rate than the growth rate. For example, a ten-fold reduction of the nucleation rate results in less than two-fold increase in the growth rate. In Figure 4.16, the predicted line-of-sight ISVF profiles are compared with the experimental measurements for the three different parameter sets listed in Table 4.5. A ten-fold reduction in the nucleation rate causes a slight delay in soot formation in the nearfield, leaving, however, the decaying branch of the line-of-sight ISVF profile in the farfield unaffected. If we further reduce the nucleation rate, then this shift is reversed and the line-of-sight ISVF profile appears to widen axially, possibly, owing to the concomitant increase in the soot growth rate.

Figure 4.17 shows the influence of the (C_r, α)-sets on the radial profiles of key variables indicating or controlling soot formation. Despite the slightly better agreement in terms of the line-of-sight ISVF for the first adjusted case, the corresponding spatial distribution of the ELS signal changes noticeably only near the burner exit plane at an axial distance of about 30 mm, where the ELS signal is almost halved. At the same time, the nucleation rate decreases slightly and the ten-fold reduction of C_r is counterbalanced by an increase in the PAH mole fractions, indicating that, for the modified kinetic rates, a new reaction equilibrium is attained whose conditions are more amenable to PAH formation. The increase in the surface growth rate takes

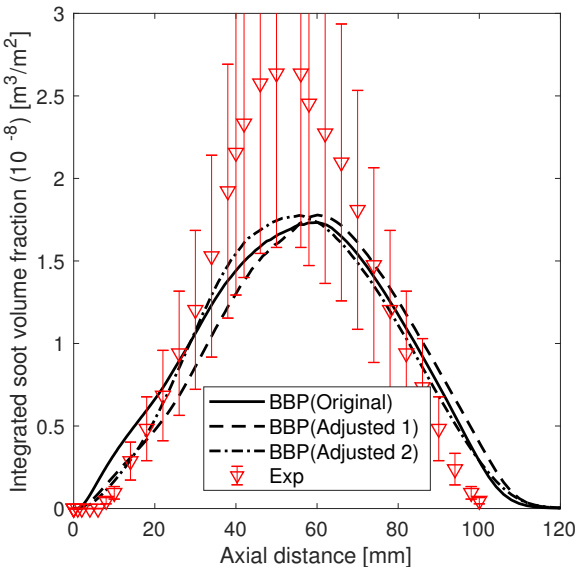

Fig. 4.16 Comparison between experimental measurements and line-of-sight ISVFs predicted by the three parameter sets listed in Table 4.5.

effect about 2.5 mm ~5 mm away from the centreline. Here, the sooty flame wings are slightly affected by the modified surface growth rate that the simulated peaks move a bit outwards from the centreline.

As the nucleation rate is further reduced to a fraction of $C_r = 0.01$, we find that the predicted ELS profiles are qualitatively more similar to those obtained from the ABF mechanism than the BBP base case. In particular, the sooty wings are shifted radially outwards. However, as a positive side effect and contrary to the ABF results, some soot remains in between the wings on the centreline and the ELS signal emitted here appears to be quantitatively accurate at 50 mm and 70 mm above the burner exit. Although the nucleation rate has been significantly reduced in the present sensitivity analysis, we emphasise that the adjusted nucleation rates computed from the BBP mechanism are still much larger than those of the ABF mechanism. This may indicate that too small a nucleation rate results in a radial displacement of the sooty wings for ethylene diffusion flames and a reduction in soot formation near the centreline.

4.6 Conclusions

In this chapter, the proposed conservative method (in Chapter 3) is robust and economical to allow for the solution of the discretised PBE when coupled with flow,

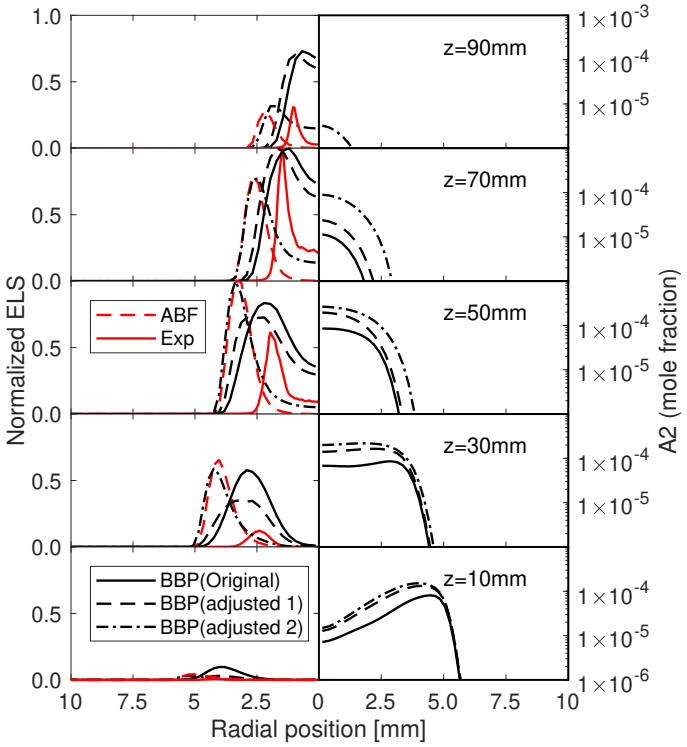

(a) ELS signal (left) and A_2 mole fraction (right)

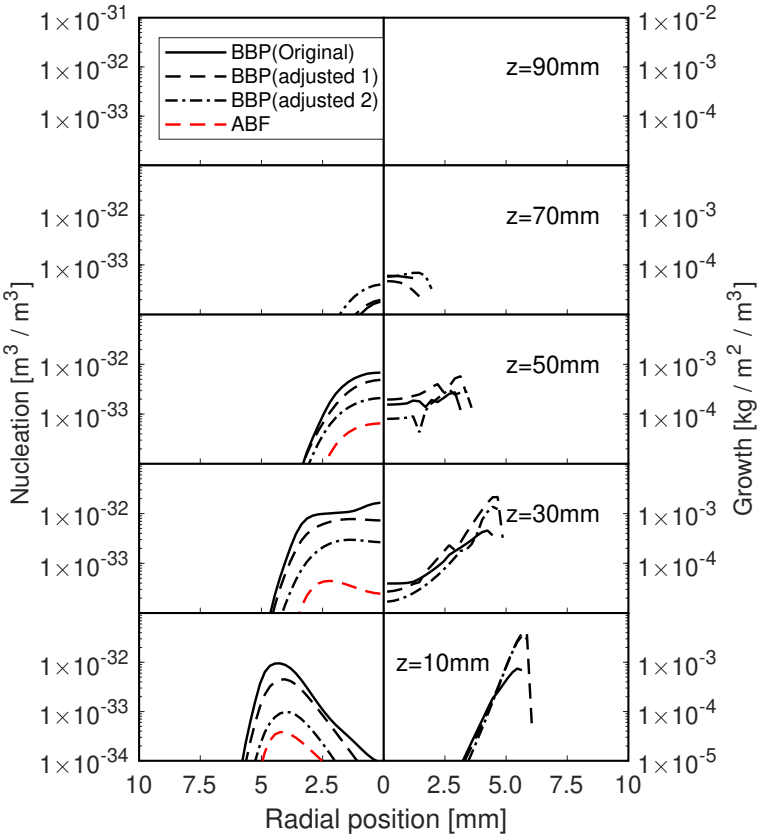

(b) Nucleation rate (left) and HACA surface growth rate (right)

Fig. 4.17 Radial profiles of key variables for the sensitivity analysis in terms of nucleation/condensation and growth rates based on the parameter sets in Table 4.5.

and thus enable the modelling of problems such as soot formation in flames. To test the method in this context, a laminar co-flow diffusion sooting flame (Santoro flame) was simulated, for which the PBE solver had to be coupled with a CFD solver, chemical kinetics, transport and radiation models. Good agreement with experimental results was obtained, and furthermore two important conclusions can be drawn from this case. First, a relatively coarse grid comprising 60 nodes was sufficient, and second, the computational effort required to solve the discretised PBE was only 8.2% of the time taken for the complete simulation. These facts indicate that the discretisation method is both accurate and economical, and therefore suitable for coupling with comprehensive CFD simulations.

In the following, a combined experimental and modelling investigation has been presented with an objective to characterise the gas phase chemistry and soot formation in a laminar diffusion flame and to provide guidance on kinetic model adjustments. Drawing on a single data source and employing multiple diagnostics gives us confidence that the simultaneous measurements reflect the same flame conditions. Planar OH laser-induced fluorescence (OH-PLIF), elastic light scattering (ELS) and line-of-sight attenuation (LOSA) measurements were used to characterise the flame structure and spatial distribution of soot and to quantify the line-of-sight integrated soot volume fraction (ISVF). The experimental dataset was supplemented by location-specific TEM images of soot particles extracted with the aid of a thermophoretic sampling device. The detailed experimental data provide guidance for validating soot models.

Our physical model integrates the population balance equation governing the soot particle size distribution into a reactive flow solver for multicomponent ideal gases. Three well-established PAH-based chemical reaction mechanisms, ABF, BBP and KM2, were employed to model the inception of soot precursors and oxidants. With regard to soot formation kinetics, our model incorporates a complete set of PAH-based nucleation, condensation, HACA-based surface growth and oxidation kinetics as well as size-dependent coagulation and aggregation. The surface area and collision efficiency of particles were estimated separately for primary particles and aggregates based on morphological considerations. A selection of empirical parameters for the processes of nucleation, condensation and growth, in coordination with corresponding chemical reaction mechanisms, were adjusted to match the experimental line-of-sight attenuation profiles. Following a recently advocated methodology [167], the experimental signals were modelled directly, allowing us to

circumvent previous physical approximations and take account of the polydispersity of soot.

The comparisons between model predictions and experimental measurements we showed reflect present predictive capability for soot formation in laminar diffusion flames. By combining a single skeleton of soot formation kinetics with three different but well validated gas phase mechanisms, the flame structure and soot appearance could be captured to a satisfying degree of accuracy. In terms of the localisation of soot in wings and the amount of soot produced, our analysis shows that soot modelling crucially relies on the background gas phase chemistry. In particular, we found that the simulations with the BBP and KM2 mechanisms were able to accurately reproduce the radial distance between the sooty flame wings. Unfortunately, soot formation or persistence on the centreline seems to present a severe challenge; the soot produced here is significantly overestimated by the BBP and KM2 mechanisms and completely absent in predictions obtained from the ABF mechanism. Our sensitivity analysis suggests that the centreline soot signals may be tuned to some extent by reducing the nucleation rates and adjusting the surface growth rate concomitantly, causing an axial delay in soot proliferation. However, on the minus side, too small a nucleation rate leads to a radial shift in the sooty wings and a depletion of soot near the centreline as shown by the ABF predictions.

Chapter 5

Population balance modelling of soot formation in laminar diffusion flames with biodiesel fuels

Modelling of soot formation and oxidation of biomass fuels is a considerable challenge, due to the complexity of the chemical reactions and soot formation pathways in the biomass fuel. In this chapter, the discretised population balance approach and the same PAH-HACA-based soot model as in Chapter 4 have been coupled with an in-house CFD code to simulate laminar diffusion flames with different blends of oxygenated biodiesel fuels and predict the associated soot formation.

Two main objectives are completed: first of all, the diffusion terms with respect to the effect of molecular weight, thermal diffusion and Dufour effect are evaluated in the transport equations and the energy equation. Second, an soot modelling of the flames with biodiesel blended fuels are compared with the experiments, and the strength and weakness of the modelling will be analysed.

5.1 Introduction

Biomass is regarded as one of the potential alternative fuels, not only to alleviate energy shortage, but also to control pollutant emissions. Extensive experiments on soot emissions for the biomass have been conducted, including solid fuels such as paper-mill residues, hard pine-wood [189], straw [190] and other biomass briquettes [191], as well as liquid fuel, usually named as biodiesel [192], as some of them have

already been employed in diesel engines [193–196] to reduce the emissions of total particulate mass.

However, soot modelling in the combustion with biodiesel fuels severely falls behind the development of experimental research due to the following several reasons. First of all, biodiesel fuels are usually composed of many unformulated heavy-molecular substances, because, they are mainly manufactured by trans-esterification reactions and their main components are saturated and unsaturated methyl esters with long alkyl chains. However, in simulations, biodiesel fules have to be specified as a few particular substances. For example, the soybean biodiesel was specified as two components: Methyl butanoate ($C_5H_{10}O_2$) and n-heptane (C_7H_{16}) by Brakora et al. [197], or three components: Methyl-9-decenoate ($C_{11}H_{20}O_2$), 1,4-hexadiene (C_6H_{10}) and n-dodecane ($C_{12}H_{26}$) by Yu et al. [198], or four components: methyl decanoate ($C_{11}H_{22}O_2$), n-hexadecane ($C_{16}H_{34}$), methyl trans-3-hexenoate ($C_7H_{12}O_2$) and 1,4-hexadiene [199]. As a result, the uncertainty in the chemical composition leads to an ambiguous foundation in the simulation of combustion with biodiesel fuels.

Secondly, a large number (hundreds or even thousands) of species and reactions should be considered in the chemical mechanism, which are usually sourced from different databases of reaction kinetics and chemical/physical properties. Errors occur when the connections of different chemical databases are not well coordinated. Besides, thermophysical and transport parameters of heavy-molecular substances are usually estimated based on species of similar molecular structures.

Thirdly, in the CFD simulations of laminar flames, the process of molecular diffusion is much more important than in the turbulent flames. Therefore, the effect of differential diffusion should be included, but an error is introduced if transport data is approximated. Besides, the transport equations of species and energy are usually numerically implemented in a simple format, by neglecting three additional terms (the effect of molecular weight, thermophoresis and Dufour effect) in the complete equations (Eq. 2.29 and 2.32). However, the additional terms are of importance in the combustion of heavy molecular weight fuels.

Last but not least in importance, the modelling of soot formation has primarily been managed and calibrated in the flames with small-molecule fuels, like ethylene [61, 62, 200], methane [110, 201] and propane [202, 203]. Soot formation modelling with heavy-molecule fuels like diesel [204, 205] and biodiesel [206, 207], are still in the stage of using simplified soot kinetics (such as the acetylene-based model) and affordable numerical method (the two-equation moment method), in order to be

implemented with complex chemistry and turbulent flows in practical diesel engines. In order to cover comprehensive soot models and numerical methods, numerical researchers explored diffusion flames with traditional methane/ethylene fuel added by the biodiesels [208, 209], or with gasoline/diesel added by biodiesel fuel [210] and make achievements within a certain extent of accuracy. However, only limited studies have explored the modelling of soot formation in flames with the blended fuel of oxygen-containing surrogates.

The main task of this paper is to employ a recently developed method for solving the population balance equation (in Chapter 4), coupled with an in-house CFD code (BOFFIN) with comprehensive transport properties, to predict soot formation in two different experiments of laminar diffusion flames with biodiesel blends. The first experiment in this study were conducted by Gao et al. [39]. In this experiment, dibutyl ether ($C_8H_{18}O$, DBE) was added in the base fuel of methyl decanoate ($C_{11}H_{22}O_2$, MD), a major component in most biodiesel fules. When the mole fraction of DBE in the fuel stream rises from 0% to 40%, the soot formation is largely suppressed. The second experiment was conducted by Tian et al. [211], where the soot concentration generated from four different practical biodiesels, and their blends with petroleum diesel are measured in a series of fully pre-vapourised co-flow diffusion flames.

5.2 Case I: the experiment on flames with pure biodiesel components by Gao et al. [39]

5.2.1 Experiment and simulation setup

The burner in the experiment consists of three concentric brass tubes. The central tube supplies the mixture of fuel: MD, DBE and carrier gas (N_2). The intermediate tube is used to supply co-flow air stream with the flow rate (8.43 L/min). The outer tube is used for N_2 as a shield to protect flames from the interference of the surrounding air (16.2 L/min). The inner diameters of three tubes are 10, 26 and 59 mm, respectively. The fuel transferred and the burner were heated at 573 K to keep the fuel above the boiling point. The air and protecting gas were preheated to 473 K. In the experiment, the carbon atom flow rates for all the fuel blends remained constantly at 6 g/h. Three flames with different fuel blends are presented in Table 5.1.

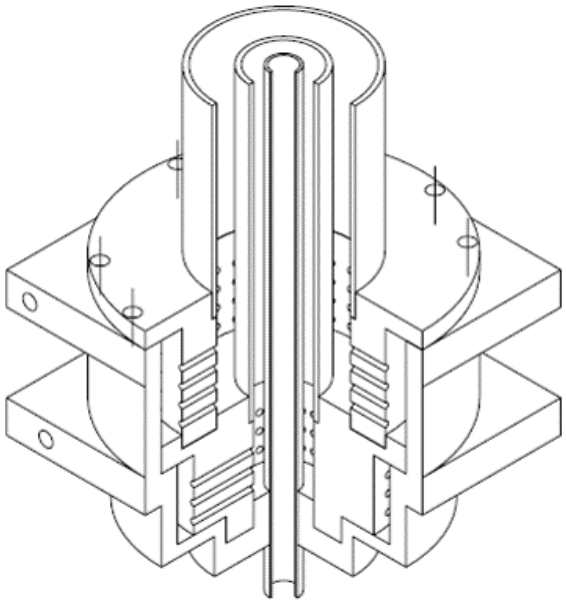

Fig. 5.1 The configuration of the burner consisting of three concentric brass tubes

A brief description of the experimental apparatus is presented in [39]. Temperature profiles in flames were measured by the rapid thermocouples and the soot volume fraction was performed by the 2D LII measurements.

5.2.2 Numerical methods and chemical kinetics

The discretised population balance equation 4.1 must be coupled with the continuity, Navier-Stokes, energy and species transport equations to solve the combustion with soot formation. The burning surrogates are of heavy molecular weight, the effect of average molecular weight, thermophoresis and Dufour effect make a difference. Therefore, the transport equations of species and energy in the complete form will be applied (Eq. 2.29 and Eq. 2.32).

Blended fuel	Biofuel			Carrier gas
	Components(mol %)		Fuel flow rate (g/h)	N_2 flow rate
	MD	DBE		
Pure MD	100	0	8.45	
70% MD	70	30	8.38	5.82 L/h
60% MD	60	40	8.35	

Table 5.1 Simulation cases: fuel components and mass flow rates

The soot model involves the processes of nucleation by the PAH dimerisation, surface growth by the HACA mechanism and PAH condensation, the coagulation of spherical particles and fractal aggregates. Empirical parameters as in Chapter 4 remain, in the model of soot formation corresponding to the BBP chemical kinetics by Blanquart and Pitsch [61].

To get insight into the process of soot formation in the laminar flame with blended fuels, a MD-DBE-PAH chemical mechanism needs to be constructed. Three detailed sub-mechanisms, respectively, of MD by Sarathy et al. [212], of DBE by Cai et al. [213], and of PAH by Blanquart and Pitsch [61] are adopted.

The skeletal mechanism for MD [212] , consisting of 648 species and 2998 reactions, reproduces the behaviour of its fully detailed mechanism in plugflow and stirred reactors for temperatures of 900 – 1800 K, equivalence ratios of 0.25 – 2.0, and pressures of 1 and 10 bar. This mechanism well predicts the test data in opposed-flow diffusion flames. The oxidation kinetics of DBE Cai et al. [213] was validated in the measurement of ignition delay times and laminar flame speeds in a laminar flow reactor. The sub-mechanism by [172], adopted in the the simulation of Santoro flame (Chapter 4) with the correct prediction, still accounts for the PAH formation. In this research, the MD and DBE are combined in the first step. Then, the combined MD-DBE mechanism is reduced to a smaller size of 447 species, by using the DRGEPSA method in the Commercial Software CHEMKINN PRO. The species shared by the PAH, MD and DBE sub-mechanism, are selected as the target species for reduction [**?**]. Numerical simulations of the closed homogeneous reactor model are performed under the stoichiometric, rich and lean conditions for the chemical reduction. Finally, the reduced MD-DBE mechanism is combined with the PAH sub-mechanism.

The reduced-combined MD-DBE-PAH mechanism includes 530 species and 3437 chemical reactions. It is compared in the homogeneous reactor with original mechanisms to predict the temperature and concentrations of species C_2H_2, OH and C_3H_3, which are important for PAH / soot formation and oxidation. All variables are well reproduced by the reduced-combined mechanism except that C_3H_3 is reduced by half due to mutual interference among the three chemistry branches.

5.2.3 Evaluation of additional diffusion terms in transport equations

For the simulation of combustion, transport equations of species and energy are always used in the simplified way (Eq. 2.57 and 2.58), with the neglect of inhomo-

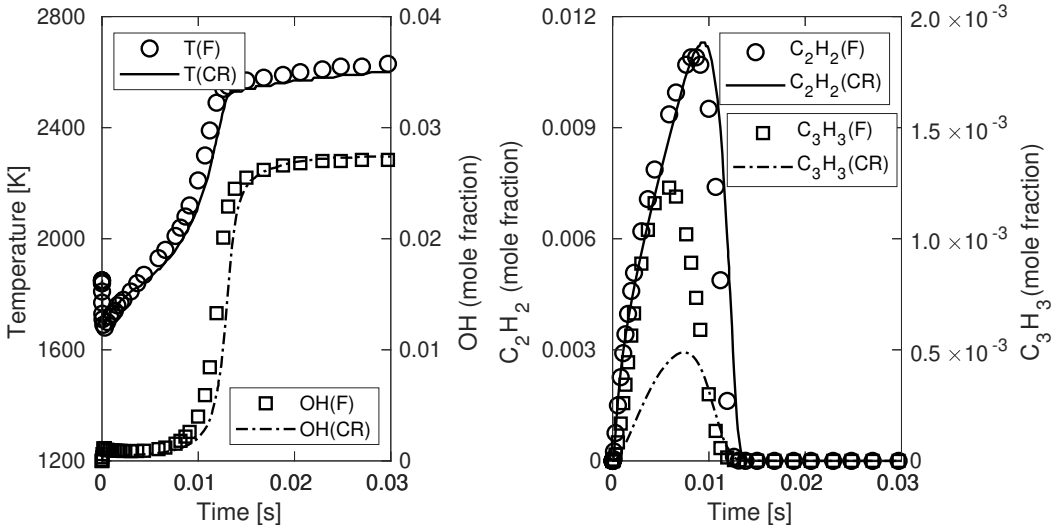

(a) The comparison of the simulation with the full MD mechanism [214] (labelled as F) and the reduced-combined mechanism (labelled as R) at the stoichiometric condition of MD and air

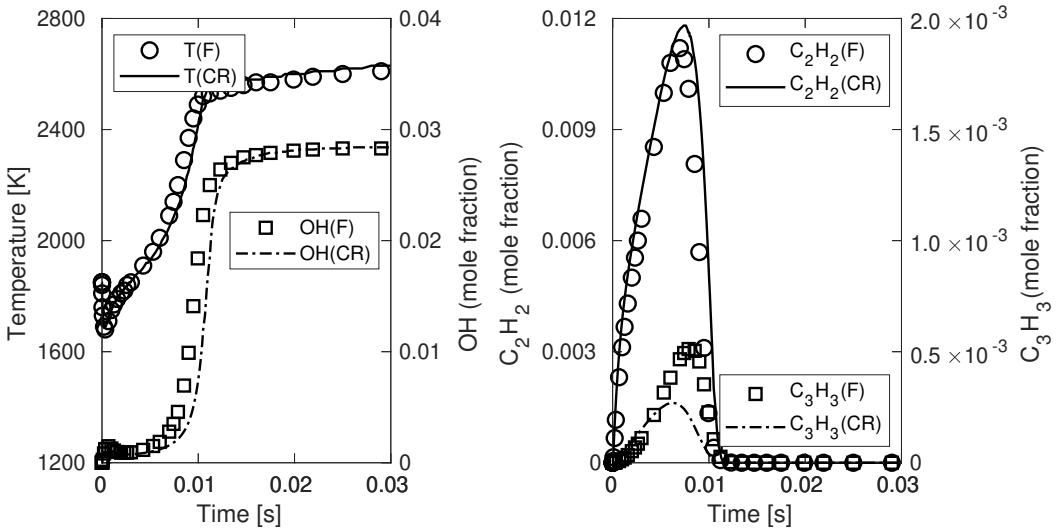

(b) The comparison of the simulation with the full DBE mechanism [215] (labelled as F) and the reduced-combined mechanism (labelled as R) at the stoichiometric condition of DBE and air

Fig. 5.2 Comparison of the simulations with full mechanisms (labelled as F) and the reduced-combined MD-DBE-PAH mechanism (labelled as CR) in a homogeneous reactor

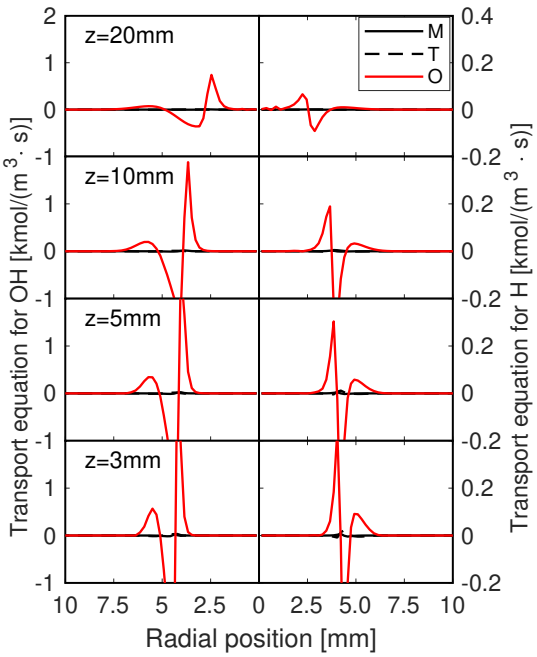

Fig. 5.3 Radial profiles of three components of diffusion terms in the transport equations of OH (left) and H (right) species at various cross-section. 'M': the effect of molecular weight; 'T': thermophoresis; 'O': the ordinary diffusion term

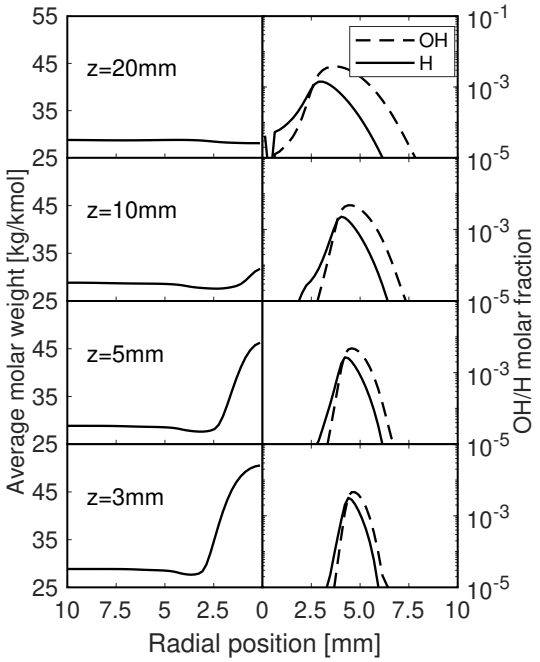

Fig. 5.4 Radial profiles of the average molecular weight (left) and the concentrations for OH and H species (right)

geneity of the average molecular weight, thermophoresis and Dufour effect (only in the energy equation). This is normally valid in the case for the fuel mixture of similar molecular weight with the air or oxidants. However, for gasoline, diesel and biodiesel fuels, the molecular weight is always around 100 ~250, so that the spatial gradient of local average molecular weight and the thermal diffusion coefficients make a difference. In this section, the components of diffusion terms, including the effect of local molecular weight, thermophoresis and Dufour effect in the species transport equations and the energy equations are evaluated.

From Fig.5.3, the transport equations with respect to H and OH species, respectively, are selected to evaluate the difference of three diffusion components since the molecular weights of molecule H and OH are much smaller than the average molecular weight $\bar{W}$ in the field (the left part of Fig. 5.4) and their thermal diffusion coefficients D_k^{T} are relative larger than that in the transport equations of other species [113]. Three diffusion components, ordinary diffusion term, effect of the average molecular weight and thermophoresis, are marked as 'O', 'M' and 'T' in the legend.

The original term oscillates in the region where the species concentrations increase and decrease (the right part of Fig. 5.4). By comparison, the effect of the molecular weight and thermophoresis is much smaller than the original term. Therefore, the additional diffusion terms are negligible in transport equations of species.

On the other hand, the additional diffusion components account more, compared with the original diffusion term at different cross-sections above the burner jet in the energy equation. 'M', 'T', 'D', 'O' in the legend represent the effect of average molecular weight, thermophoresis, Dufour effect and the original diffusion term, correspondingly. First of all, the effect of the gradient of local average molecular weight starts from positive magnitude close to the jet burner until the 10 mm above, corresponding to the large average molecular weight in Fig. 5.4. The effect of the molecular weight starts from positive magnitude close to the jet burner until 10 mm above, corresponding to the region of high average molecular weight in Fig. 5.4. Then the effect becomes negative due to the varying average molecular weight, compensating the positive original diffusion term. Around the reacting zone of peak temperature (the left column in Fig. 5.5) and species source (the right column of Fig. 5.4, thermophoresis and Dufour effect contribute an opposite equivalence to the original diffusion term, although the absolute values are minor compared with those around the centreline. Different from the transport equation of species (Eq. 2.57), no source term exists in the energy equation in terms of total enthalpy. Therefore, the additional components in the diffusion affect the transport of energy, thus mainly the temperature field.

5.2.4 Numerical results and discussion

In this part, the numerical results of temperature profiles and local soot volume fraction are demonstrated and compared with the experiment from Gao et al. [39].

Temperature profiles

Figure 5.6 compares the computed temperature profiles with the measurements. For all three flames, the predicted temperature profiles correspond well with the test data. The exception is that in the region from 20 mm to 30 mm HAB in the flame with pure MD, the predicted temperature is around 100 K to 150 K lower than experimental results. For the flame with 60% MD, the lower temperature is predicted prior to 10 mm HAB, which represents that the simulated heat release is slower than in the experiment. In general, both the experiment and simulation

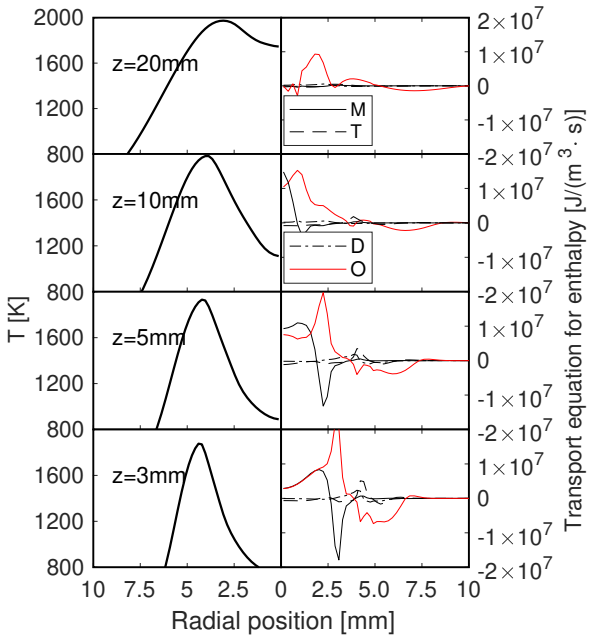

Fig. 5.5 Radial profiles of temperature (left) and components of diffusion terms in the energy equation (right). 'M': the effect of molecular weight; 'T': thermophoresis; 'D': Dufour effect; 'O': the ordinary diffusion term

indicate higher peak temperatures with more DBE addition, although the numerical solutions present a smaller difference among the three flames.

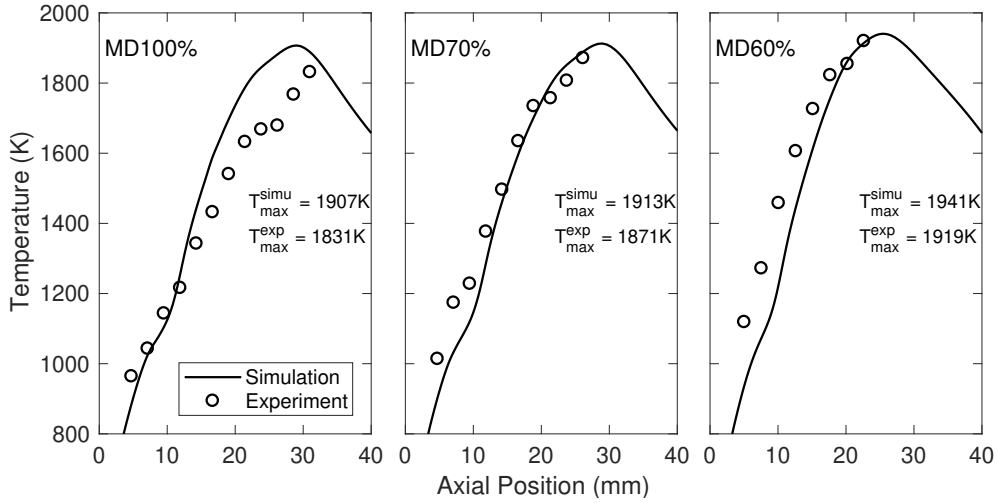

Fig. 5.6 Temperature profiles along the centreline of the flames with pure MD, 70% MD and 60% MD

Soot formation of the biodiesel surrogates

Figure 5.7 shows the two-dimensional distribution of soot volume fraction for both the experiment and simulation. The two contours are displayed in the same

unit (ppm), which illustrates that the numerical model predicts a correct magnitude of soot volume fraction. Essentially, the swallow-tail shape of the soot region is correctly captured by the simulation. Although the prediction shows the emergence of soot at around 7 mm upstream than in the experiment, the positions of soot decaying are correctly predicted in the cases of flames with pure MD and 70% MD. In the experiment, the soot loadings reduce with the addition of DBE, especially a significant reduction as the fraction of MD decreases from 70% to 60%, which is also presented in the simulation. Quantitatively, in Fig. 5.8, the predicted integrated soot volume fraction on the centreline reduces by about 33% as the mole fraction of DBE increases from none to 40%, compared to a much larger reduction of around 55% in the measurement. Besides, in the simulation, the position where soot particles are entirely burnt out moves forward by 5 mm, compared with 10 mm in the experiment as the DBE addition increases to 40%. Another weakness is that the sooty wings are overpredicted by the simulation while more soot forms around the centre region in the experiment.

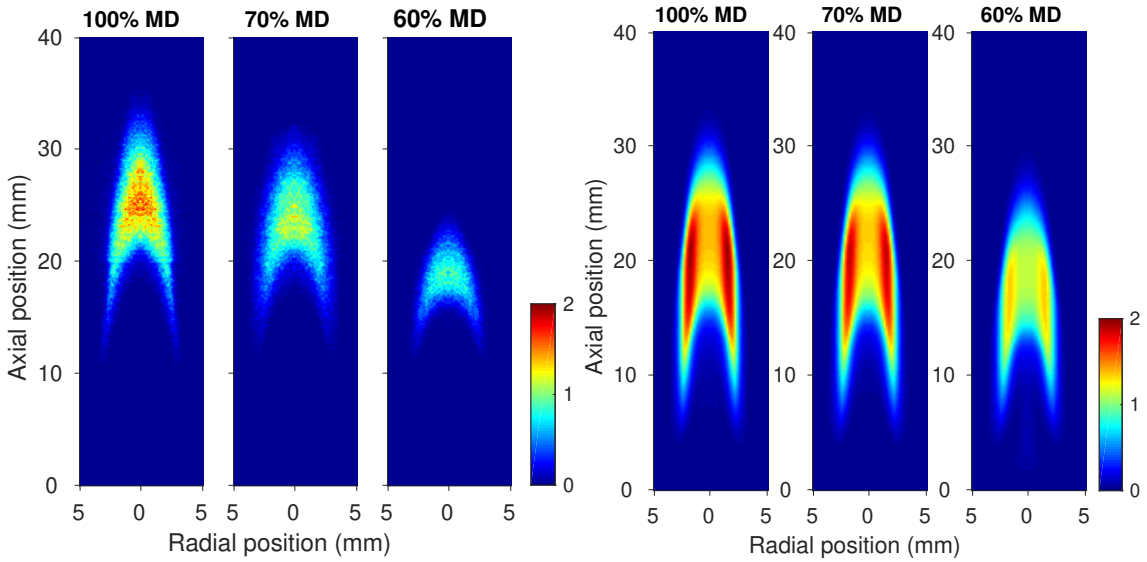

(a) The experimental results (unit: ppm)

(b) The numerical results (unit: ppm)

Fig. 5.7 Comparisons of the soot volume fraction in contours between the experiment [39] and simulation

Acetylene and PAH concentration

The population balance modelling of soot formation is based on the PAH-HACA mechanism, therefore, the soot formation is determined by the concentrations of C_2H_2 and PAH. Figure 5.9 and Figure 5.10 show contour plots of mole fractions

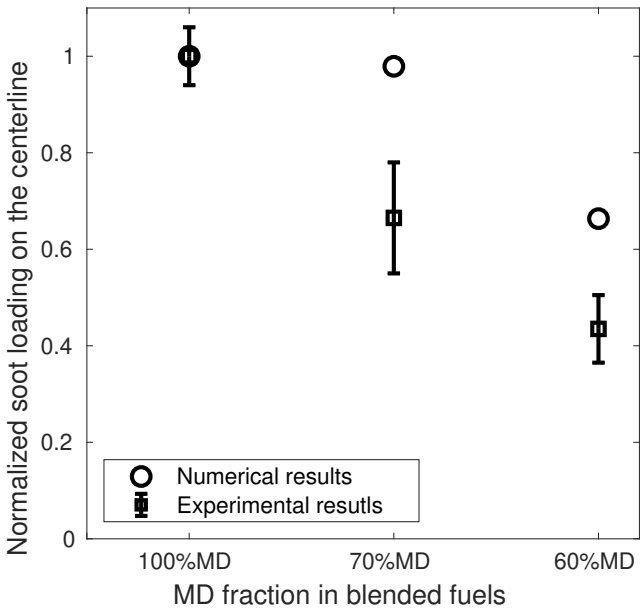

Fig. 5.8 Normalized total soot loading as a function of the MD mole fraction

of C_2H_2 and PAH by the simulation for the three flames, where the mole fraction of PAH accounts for the sum of species A_2, A_3 and A_4.The C_2H_2 concentration only drops slightly in the flame with 60% MD, while the PAH concentration is suppressed by adding DBE in the fuel blends, around 50% quantitatively smaller on the centreline in the flame with fuel of 60% MD than the pure MD, according to Fig. 5.11. As C_2H_2 contributes directly to the surface growth while the dimerisation of PAH lead to soot nucleation and condensation, the soot reduction is mainly caused by a decreasing nucleation and condensation rate.

Two different kinetics pathways: the combination of propargyl radicals and the reactions of C_4Hx species with acetylene, contribute to the cyclisation of the first aromatic rings (A1), which is a symbol to demonstrate the formation of PAH.

In Fig. 5.11, the concentrations of species C_3H_4, C_3H_3, C_4H_4, C_2H_3 along the centreline show 5% - 15% reduction as the DBE addition increases from none to 40%, which determines the reduced formation of PAH.

$$C_3H_4(P)/C_3H_4(A)/C_3H_3 + C_3H_3 = A_1(+H) \tag{5.1}$$

$$C_4H_4(C_4Hx) + C_2H_3(C_2H_2) = A_1(+H) \tag{5.2}$$

As a whole, the soot model can effectively capture the reduction of soot formation by adding DBE into MD fuels. However, the discrepancies between simulations and measurements arise, namely: early locations of soot occurrence and slighter

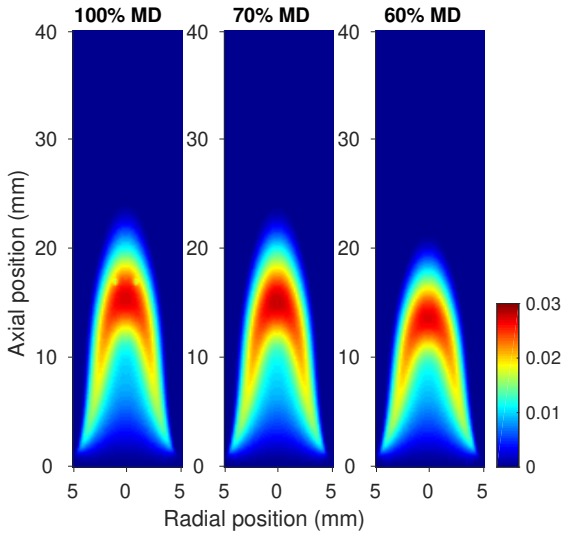

Fig. 5.9 The contour plot of C_2H_2 (mole fraction)

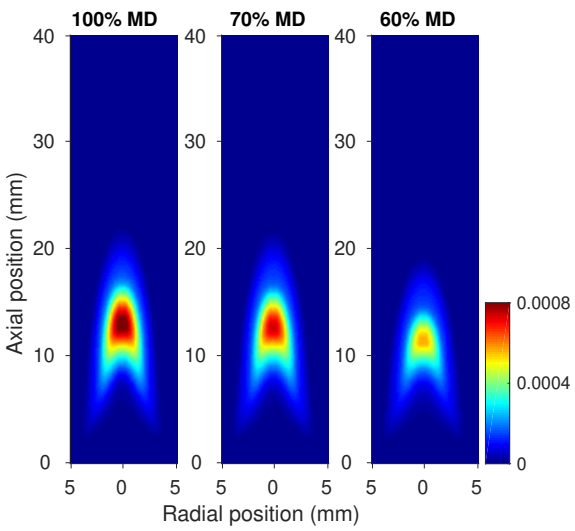

Fig. 5.10 The contour plot of PAH (mole fraction)

suppression of soot in the DBE adding cases. The differences can be attributed to the following reasons. A primary issue arises in the combined and reduced MD-DBE-BBP chemistry. All the three parts are from different research group and coordinating them leads to errors, as Fig. 5.2 displays. Second, the empirical parameters therein were calibrated based on ethylene diffusion flames [10]. The soot model applied in this research proves to be reasonable in dealing with sooting flames with different fuels, but is likely to be more accurate by adjusting based on morphological parameters in the biodiesel fuels individually.

5.3 Case II: the experiment on flames with practical biodiesel fuels by Tian et al. [211]

In this case study, four different practical methyl ester biodiesels derived from carotino red palm (CP), rice bran (RB), duck fat (DU), goose fat (GO), and their blends with petroleum diesel are investigated. Diesel are tested as references. Soot volume fraction in tested flames is then measured using extinction-calibrated LII [216] and corrected for signal trapping effects using the algorithm developed in [217].

The modelling part employs a comprehensive kinetic mechanism developed for a large variety of fuels related to diesel and biodiesel [218] to simulate the pyrolysis and combustion of fuel blends. The developed discretised population

balance method, considering a complete set of processes of soot evolution in Chapter 4, is coupled with the reacting flow to model soot formation in the combustion of biodiesel blends.

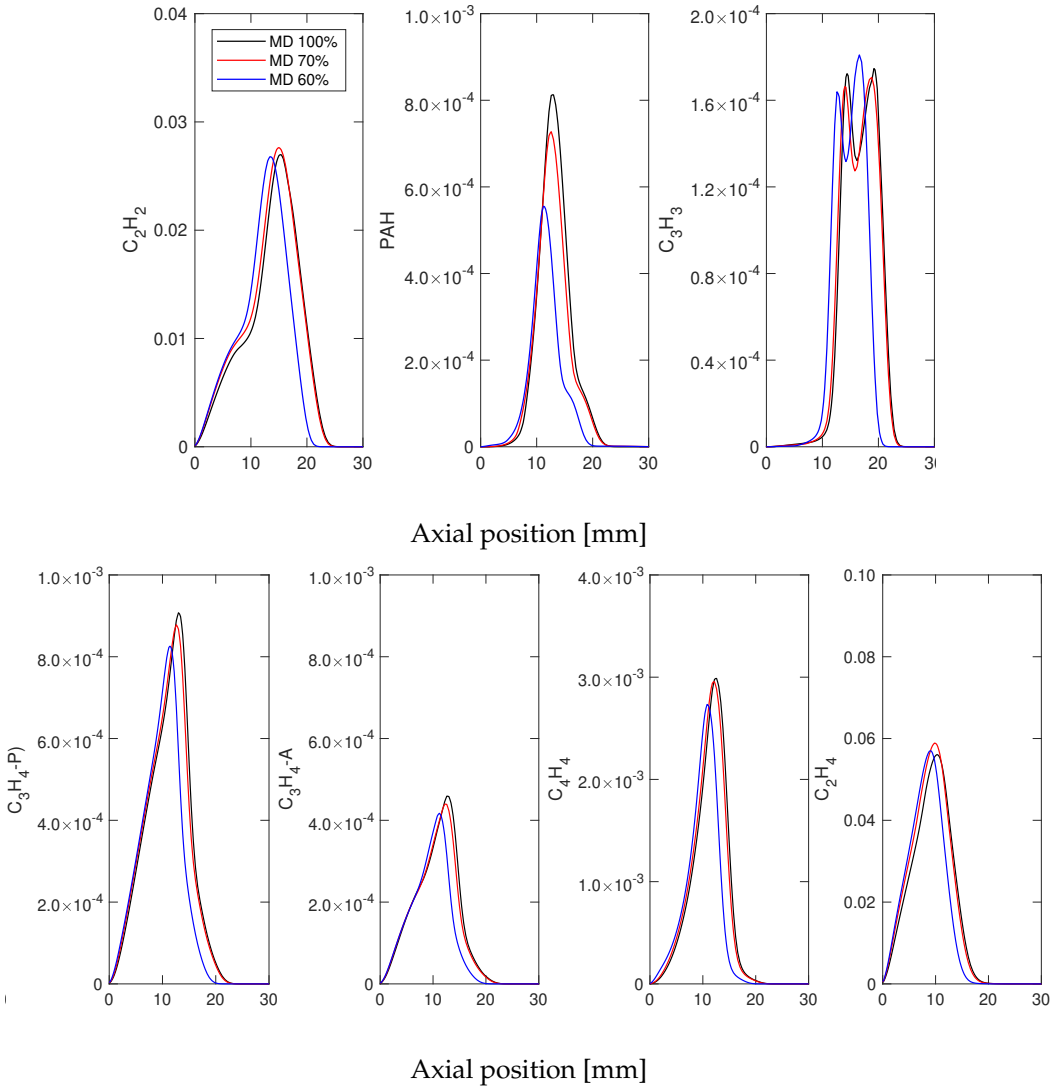

Fig. 5.11 The profiles of concentrations of C2, C3, C4 species on the centreline

A diagram of the pre-vapourised diffusion burner is shown in Fig. 5.12. The liquid fuels are injected into the vaporising system via a syringe pump. The mass flow rates of fuels are regulated based on the mass consumption rates of the liquid fuels in a buoyancy-induced standard pool flame as described in [217]. The values are selected as 0.1191 g/min for diesel, 0.1164 g/min for CP, 0.1036 g/min for RB, 0.1109 g/min for DU, 0.0936 g/min for GO.

The sligthly different mass flow rates are taken from an original study matching laminar pool flame burning rates and prevapourised fuel rates [**?**].

Nevertheless,the estimated heat release rates for all the tested neat cases are within $\pm 15\%$ of the mean. A co-flow of air at 0.18 m/s is used to stabilise the diffusion flame. The fuel delivery line is heated using electrical heating tapes (OMEGA STH102 series). The temperature of the tapes is controlled by two closed-loop temperature controllers, while a thermometer is used to monitor the temperature of the heating tape at the inlet of the system, which is denoted as T_1. The temperatures in the middle and the outlet of the system are denoted as T_2 and T_3 respectively. During the tests, T_1, T_2 and T_3 are maintained constant at 520 ± 30 °C, 470 ± 30 °C and 400 ± 30 °C, respectively. As the boiling point of the fuels are below 400 °C [219], the temperature is sufficiently high for a full vapourisation. The fuel vapourisation line is designed to achieve sufficiently long residence times (≥ 3 min) to ensure full evaporation.

The 2D LII measurements are performed using a setup similar to that in Ref. [217], in which the measured LII signal is quantitatively calibrated via absorption, with correction for signal-trapping. Soot particle samples are collected by using the thermophoretic deposition method used in [220].

5.3.1 Experiment setup

The tested fuels in the present study are all methyl esters (ME) produced from plant oil or animal fat feedstocks via the transesterification process. The feedstocks used are carotino red palm oil (CP), rice bran (RB), duck fat (DU) and goose fat (GO). Petroleum diesel is also tested as a baseline. The composition of different types of biodiesel is measured using a gas chromatograph (GC, Agilent 7620A) based on the EN14103 standard, and listed in Table 5.2. The measured average formula for CP, RB, DU and GO are: $C_{18.7}H_{36.9}O_{2.0}$, $C_{18.6}H_{36.9}O_{2.0}$, $C_{18.3}H_{36.5}O_{2.0}$ and $C_{18.5}H_{36.6}O_{2.0}$, respectively. All biodiesels tested contain about 11% (mass fraction) of oxygen. However, the unsaturation levels of the two types of animal fat derived biodiesel (DU and GO) are much lower than plant-based biodiesel (CP and RB), as listed on Table 5.2. A previous study [217] on unsaturation suggests that the soot yields of CP and RB are higher than DU and GO.

	CP	RB	DU	GO	ML	MM
C12:0	0.000	0.000	0.000	0.000	1.000	0.000
C14:0	0.003	0.004	0.009	0.004	0.000	1.000
C16:0	0.139	0.216	0.317	0.268	0.000	0.000
C18:0	0.602	0.431	0.565	0.588	0.000	0.000
C18:1	0.172	0.321	0.110	0.131	0.000	0.000
C18:2	0.068	0.012	0.000	0.009	0.000	0.000
C18:3	0.016	0.016	0.000	0.000	0.000	0.000
Unsat.	0.356	0.394	0.110	0.149	0.000	0.000
Avg. C Chain	17.71	17.55	17.33	17.45	12.00	14.00
MW^a	293.2	291.0	288.4	290.0	214.0	242.0
ΔH^b	40.6	37.50	39.4	39.4	38.02	39.03
Y_C	0.77	0.77	0.76	0.76	0.73	0.74
Y_H	0.13	0.12	0.13	0.13	0.12	0.12
Y_O	0.11	0.11	0.11	0.11	0.15	0.13
X_C	18.7	18.6	18.3	18.5	13	15
X_H	36.7	36.3	36.4	36.6	26	30
X_O	2	2	2	2	2	2

a: units: g/mol; b: units: MJ/kg

Table 5.2 Properties and compositions of biodiesel fuels. CP: carotino red palm oil biodiesel. RB: rice bran biodiesel. GO: goose fat biodiesel. DU: duck fat biodiesel. ML: methyl laurate. MM: methyl myristate. Top section: Composition (mole fraction) of biodiesels measured using GC. C12:0 means 12 carbon atoms in the main chain of fatty acid with zero double C = C bonds. Bottom section: Properties and elemental mass percentage of biodiesels. The degree of unsaturation is calculated by multiplying the mole fraction of each species times the associated number of C = C double bonds. Heating values ΔH of CP are from [219, 221]; heating value of yellow grease biodiesel from [219] is used as values of DU and GO; values for RB are from [222, 223]; values for ML and MM are from the NIST website [224, 225]. The mass fractions and average molecular formula are denoted by Y and X, respectively.

5.3.2 Modelling of chemistry and soot formation

The simulation employs a semi-detailed kinetic mechanism [218] for the pyrolysis and combustion of a large variety of fuels, where 249 chemical species and 8153 combined chemical reactions are considered. This mechanism was initially developed based on hierarchical modularity and then improved via the validation with a vast amount of experimental data on the laminar flame speeds of hydrocarbon and oxygenated fuels. In the mechanism, long-chain alkanes and alkenes represent the composition of the diesel, while saturated and non-saturated methyl esters represent the composition of biodiesel fuels. In addition, aromatic hydrocarbons are also involved in the chemical kinetics to model the nucleation process in the soot formation. Therefore, the mechanism cited in the supplementary material in Ref. [218] is integrated to deal with the chemical reactions of diesel and biodiesel surrogates, as well as the soot formation precursors.

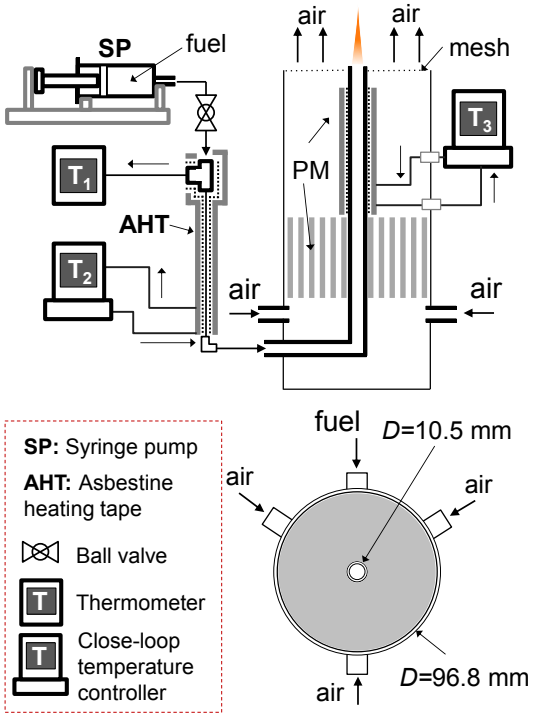

Fig. 5.12 Schematic of the co-flow diffusion flame.

According to [226, 227], the diesel fuel is approximated as a mixture of long-chain alkanes and alkenes, with a small fraction of aromatic hydrocarbons. The four biodiesel surrogates are assumed to be a mixture of a long-chain alkane (n-hexadecane, n-$C_{16}H_{34}$), a alkene (1,4-hexadiene, HXD14), a saturated methyl ester (MD) and a non-saturated methyl ester (methyl trans-3-hexenoate, MH3D) [228].

However, some species are absent in the mechanism [218], and are thus substituted by other substances of similar chemical structures. Therefore, the approximate composition of the diesel fuel and four biodiesel surrogates used in the simulation is shown in Tables 5.3 and 5.4.

Table 5.3 Setup of composition of diesel (mass %)

Composition	Refs. [226, 227]	Present
$C_{10}H_{22}$	5.6	7.6
$C_{12}H_{26}$	20.9	20.9
$C_{14}H_{30}$	26.0	26.0
$C_{16}H_{34}$	16.6	30.4
$C_{18}H_{36}$	15.8	—
C_6H_{12}	3.7	3.7
$C_{10}H_{18}$	6.4	6.4
C_7H_8	5.0	5.0

Table 5.4 Setup of composition of biodiesel surrogates (mole %)

Ref. [228]	Present	CP	RB	DU	GO
MD: $C_{11}H_{22}O_2$	$C_{11}H_{22}O_2$	53.09	54.98	52.99	52.84
MH3D: $C_7H_{12}O_2$	$C_5H_8O_2$	1.37	2.56	0.88	1.05
	$C_8H_{14}O_2$	2.74	5.13	1.76	2.10
Hexadecane: $C_{16}H_{34}$	$C_{16}H_{34}$	40.23	36.41	44.37	43.76
HXD14: C_6H_{10}	C_5H_8	1.28	0.46	0.00	0.13
	C_7H_{12}	1.28	0.46	0.00	0.13

The soot model involves the processes of nucleation by PAH dimerisation, surface growth by the HACA mechanism, PAH condensation and coagulation of spherical particles and fractal aggregates. Empirical parameters as in Chapter 4 remain, in the model of soot formation corresponding to the BBP chemical kinetics.

5.3.3 Results and discussion

Figure 5.13 presents the measured and modelled spatial distribution of the soot volume fraction, f_v , for the case of a neat diesel flame (D100) from HAB = 4 mm to 32 mm.

Both measured and model patterns of the sooting zone indicate a coincidence of the highest soot zone forming region on the inside of the high temperature zone. The model results show a significantly broader distribution compared to the very thin measured soot production zone.

The inception of soot takes place around the intersection between the fuel and air streams at the burner exit, and the maximum soot volume fraction $f_{v,m}$ appears near the reaction zone at the interface of fuel and air, at between 20 and 25 mm HAB (22.0 mm for measured data and 24.5 mm for model). The predicted maximum soot volume fraction obtained by the simulation (6.9 ppm) is only 52% of the experimentally measured value of 13 ppm).

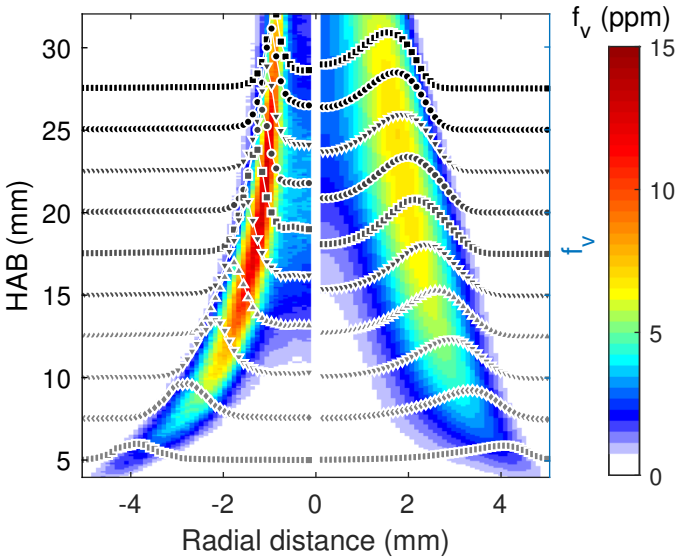

Fig. 5.13 Measured (left) and modelled (right) local volume fraction of soot in D100 flame from HAB = 4 to 32 mm. Dotted lines show profiles plotted in steps of 5 mm HAB.

The sooting propensity of biodiesel fuels is investigated in four series of cases (from CP to GO). The tested cases are noted by the two initial letters of the biofuel and the percentage by mass used in the mixture, e.g. CP20 refers to 20% by mass in carotino red palm oil biodiesel. The results of all tested cases are shown in Fig. 5.14. Both measured and simulated f_v map of each case are shown in each sub-figure. For cases with blending ratio $r_b \leq 60\%$ of biodiesel, the visible flame height is not well-

defined, as the unburnt soot emits from the flame tips. In contrast, when $r_b \geq 80\%$, the soot no longer emits from the flame tip, which means all soot is oxidised across the flame.

Measurements show a dramatic drop in the observable height where soot is detected, r_b, from 60% to 80%. However, this behaviour is not reproduced well by the simulation. For all four cases of biodiesel blends, when $r_b \geq 80\%$, the calculated maximum heights where soot is found are significantly larger than experimental measurements. The behaviour of the sooting region height can be explained using

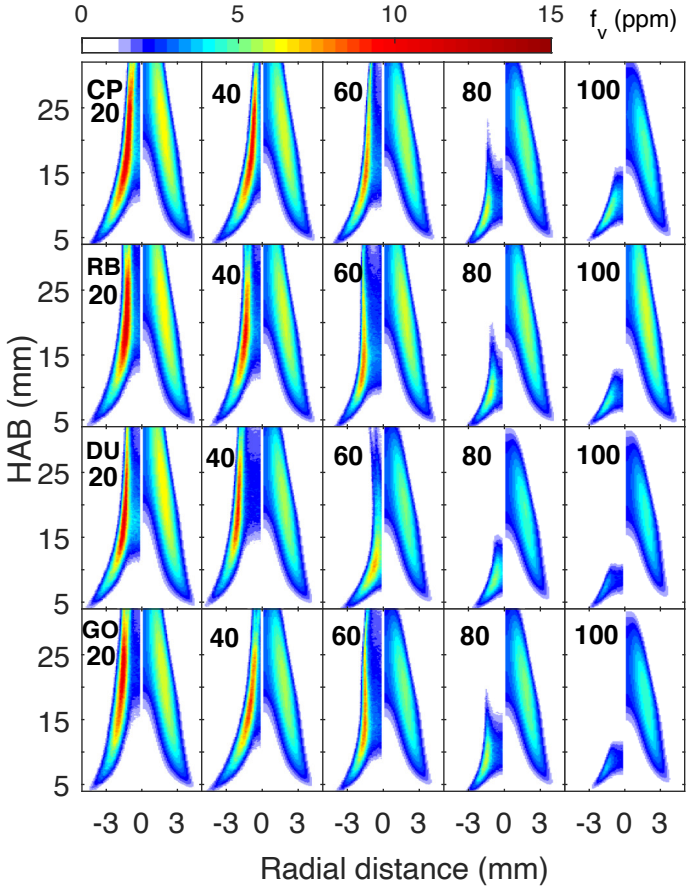

Fig. 5.14 Measured and modelled local volume fraction of soot for each test case. Measurements (left panels), models (right panels) for each fuel and % by mass addition.

the variation in the stoichiometric mixture fraction Z_{st} of the diffusion flames. The calculated Z_{st} for D100 is 0.0155, 0.0180±0.0005 for all neat biodiesel. Higher Z_{st} suggests a location of the iso-surface towards the fuel side, thus rendering the flame and sooting zone thinner.

Values for the maximum soot volume fraction $f_{v,m}$ in each flame series are shown in Fig. 5.15. Both experiment and simulation show a decrease in $f_{v,m}$ with increasing

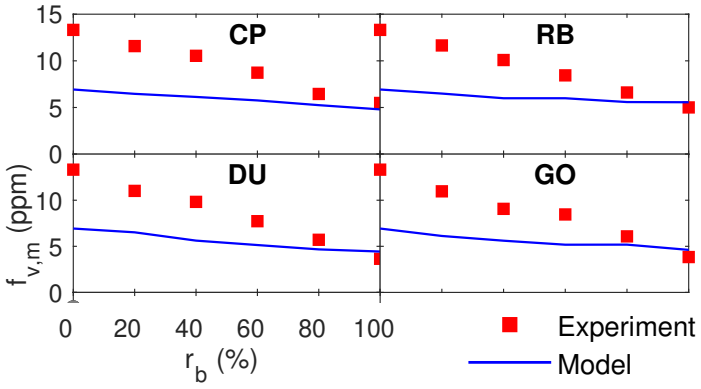

Fig. 5.15 Measured and modelled mean soot volume fraction as a function of biodiesel volume fraction.

r_b. Pure diesel yields the highest $f_{v,m}$ due to the presence of aromatic hydrocarbons and zero bound oxygen.In all neat and blended cases, two biofuels CP and RB, which are derived from plant oil with higher unsaturation degree (UD) yield higher $f_{v,m}$ than DU and GO. Considering that the oxygen mass fraction of the tested biodiesels are almost identical, the result indicates that the UD is a key factor for soot yield, as observed in [217] for other fuels. Although the model correctly predicts a decrease in $f_{v,m}$ with r_b and the minimum soot values for all biodiesels, the rate of change is not well predicted. However, are very well predicted.

A reasonable, if imperfect, measure of the total soot formation propensity can be constructed using An area-based mean soot volume fraction $\bar{f}_v$ in the flames over the detectable region from HAB = 0 to 32 mm,

$$\bar{f}_v = \left(\frac{1}{\pi R^2}\right) \int_0^R 2\pi r f_v(r) dr \tag{5.3}$$

where R is the radius of the fuel tube. The mean soot volume fractions as a function of HAB $\bar{f}_v$ of all neat cases are plotted in Fig. 5.16. For the neat biodiesel cases,the predicted values of $\bar{f}_v$ are commensurate with the measurements, but the extent of the measurements is confined to a much narrower region, as expected from 5.14.

The SEM measured particle size and corresponding lognormal fits for all neat cases are shown in Fig. 5.17. The primary particle size was modelled as a lognormal distribution, with a best fit geometric mean diameter D_m and distribution width σ as shown in the histograms of tested cases.

The results indicate that the cases with higher f_v also yield larger D_m. The modelled values, D_c, are however, somewhat smaller than measured values.

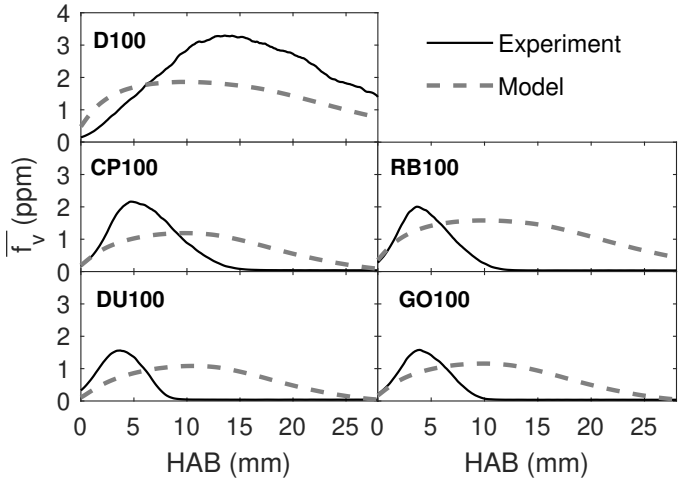

Fig. 5.16 Measured and modelled area-weighted mean soot volume fraction in unblended cases.

Among biofuels, the two most unsaturated fuels (CP and RB) produce larger sizes and number densities of soot particles compared to the two less saturated biofuels (DU and GO) and the two methyl esters (ML and MM).

This results from the fact that unsaturated bonds increase the concentration of both soot inception and growth species such as benzene C_6H_6 and acetylene C_2H_2, which are believed to be the main soot surface growth species according to the HACA mechanism [87]. Similar conclusions were also drawn in [229], in which the fuel was diluted using N_2.

As a whole, the soot model can effectively capture the reduction of soot formation by adding biodiesel fuels. However, several discrepancies between simulations and measurements arise, namely: for the pure diesel case, soot value predictions are lower than those measured, and the soot also disappears later than predicted. For biodiesels, the concentrations are lower and more distributed, and the average primary particle size is smaller.

The differences can be attributed to the following reasons. A primary issue arises through the assumed compositions of the diesel and biodiesel fuels in the simulations (Table 5.3 and 5.4). These are still simplifications compared to the hundreds of hydrocarbons present. Second, the chemical kinetics [218] employed in this simulation is semi-detailed for pyrolysis and combustion of the main substances of diesel and biodiesel fuels. However, many elementary chemical reactions are condensed into model reactions, a fact that affects the concentrations of the precursor species used in soot modelling. Lastly, the empirical parameters therein were calibrated based on ethylene diffusion flames [230] using the gas-phase chemistry by

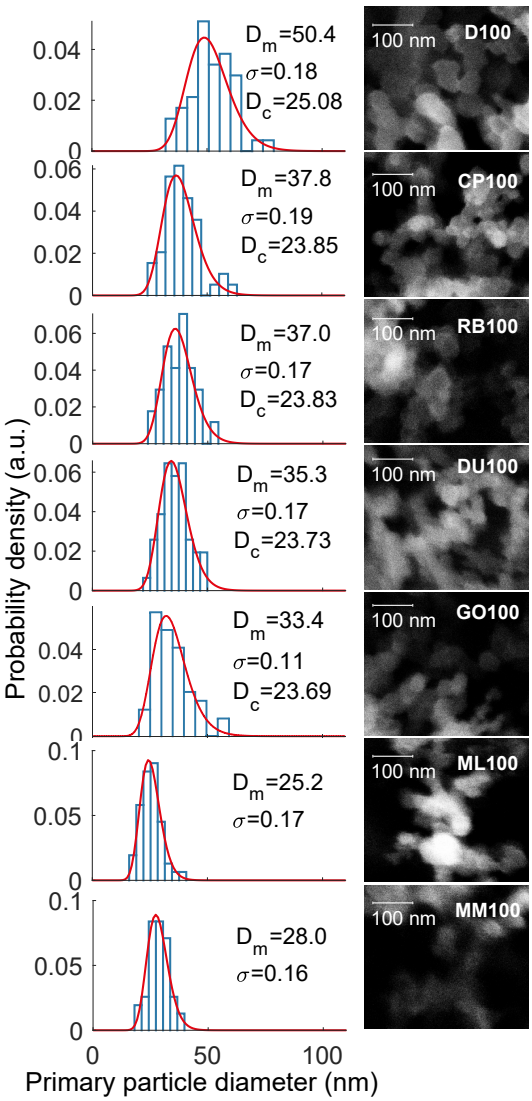

Fig. 5.17 SEM images and corresponding particle size distribution for tested neat fuel cases. Best lognormal fit of the measured diameter distribution shown as red solid line. Best fit values of geometric mean diameter D_{m} and distribution width σ are shown in the histogram for each case. The calculated mean particle diameter D_{c} using the model described in Section 5.3.2 is also listed in the figure.

Blanquart et al. [172]. The soot model applied in this research proves to be reasonable in dealing with sooting flames with different fuels, but is likely to be more accurate by adjusting based on morphological parameters in the diesel and biodiesel fuels individually.

5.4 Conclusions

This article extends the modelling of soot formation to laminar diffusion flames with oxygenated surrogate blends in two different experiments. The discretised population balance modelling of soot formation involves the processes of nucleation (PAH dimerisation), surface growth (HACA and PAH condensation) and coagulation of spherical particles and fractal aggregates. Given that so far there have been very few attempts to model soot formation in biodiesel flames, especially for the blends with all oxygenated fuels, the results are encouraging.

In the first experiment by Gao et al. [39]: the dibutyl ether (DBE) addition to methyl decanoate (MD). Three detailed chemical mechanisms, the MD by Sarathy et al. [212], the DBE by Cai et al. [213] and the PAH sub-mechanism by Blanquart and Pitsch [61] used in Chapter 4, are reduced and combined as the MD-DBE-PAH mechanism with 530 species and 3437 reactions. The same model of soot formation as applied in Santoro flame in Chapter 4 is also utilised to predict the soot formation in the laminar coflow flame with MD-DBE blended surrogates.

In the spatially heterogeneous combustion with fuels of heavy molecular weights, additional diffusion terms (the effect of average molecular weight, thermophoresis and Dufour effect) should be considered in the transport equations of species and energy. Particularly in the energy equation, the effect of the average molecular weight plays an important role around the burner exit, while thermophoresis and Dufour effect account in the region of peak temperature, which even counterbalances the original diffusion term.

The predicted temperature profiles are basically in line with the experiment in terms of the position and absolute value. For the soot formation, the swallow-tail shape of the soot region and the absolute value of soot production are correctly captured by the simulation. The model predicts 33% decrease of soot production as the DBE addition is from 0 to 40%, in contrast to around 55% reduction measured in the experiment. In the PAH-HACA soot mechanism, the predicted PAH concentration drops by around 50% as the DBE addition is up to 40% while the acetylene concentration barely changes.

In the second study, soot volume fractions in undiluted, fully pre-vapourised, co-flow diffusion diffusion flames fuelled with four real biodiesels, and their blends with pure petroleum diesel are modelled using diffusion flame models including population balance and soot kinetics, compared with the LII/extinction measurement by Tian et al. [211].

The results show that the model can capture the reduction of soot formation by addition of biodiesels, but not necessarily the rate of decrease with blending. Further work is required to resolve discrepancies between numerical and experimental results, by improving the certainty of compositions of biodiesel fuels, developing detailed chemical kinetics and adjusting based on morphological parameters in the diesel and biodiesel fuels individually.

Chapter 6

Conclusions and Future Work

6.1 Summary and conclusions

Prediction of soot formation in combustion is complex as the processes contain fluid dynamics, chemical reactions, soot kinetics and dynamics. In this thesis, a discretised population balance equation (PBE) with a model of complete processes of soot formation has been coupled with an in-house code of computational fluid dynamics (CFD), in order to predict the evolution of soot in laminar diffusion flames. Three accomplishments have been achieved.

In terms of methodology, a conservative finite volume method is proposed for the discretisation of the PBE with the coagulation process, in which the discretised source contributions are rigorously derived from the continuous PBE on the finite volume scheme, rather than estimating the source term with traditional algorithms of quadrature or interpolation. The main concepts of the method includes: a) an employment of an auxiliary grid of complementary points that are needed to accurately calculate all coagulation events, b) a geometric approach to evaluate the double integrals resulting from the finite volume integration of the coagulation terms, c) the detailed balance of source and sink terms to conserve the moments. The method thus attains accurate prediction of the distribution with a small number of PBE nodes (or sections) as well as conserves the first moment (or any other single moment). Furthermore, the method is flexible to an arbitrary non-uniform grid due to its "interval-oriented" feature. An Extensive test on the proposed method was carried out, by comparing with analytical solutions, direct numerical solutions by the discrete PBE approach and the 'self-preserved' distribution, with both theoretical and physically realistic kernels. Results showed that the method produces very

accurate solutions that conserve the chosen moment, even on coarse grids and distorted grid.

The proposed discretisation method of the PBE has successfully predicted the coagulation and breakage process of a homogeneous reacting flow: a colloidal suspension of white sulfate polystyrene and the coagulant $Al(NO_3)_3$ solution. The variation of mean radius of gyrations for the particles coincides well with the experimental results. The temporal evolution of the particle size distribution has showed powerful strengths of the discretised populationa balance modelling.

The proposed method was subsequently employed to simulate a laminar co-flow diffusion flame, an inhomogeneous reacting flow, to assess its economic performance and robustness. The PBE solver, augmented with a complete set of processes of nucleation, growth and coagulation, has been coupled with the CFD solver, involving chemical kinetics, transport and radiation models. A good agreement with experimental results is obtained, but furthermore, a coarse grid comprising 60 nodes is sufficient to obtain converged profiles covering the volumeric range of 9 - 10 orders of magnitude. As to computational efforts, only less than 10% the entire cost of the PBE-CFD program is spent on solving the PBE.

In terms of modelling on soot physics, a joint numerical population balance modelling and experimental laser diagnostic investigation is presented for the soot formation in laminar diffusion flames. The simultaneous multiple diagnostics measurements drawn from a single data source provide guidance on soot kinetic models. The physical model integrates the PBE governing the soot particle size distribution into a reactive flow solver for multicomponent ideal gases. Three well-established PAH-based chemical reaction mechanisms, ABF, BBP and KM2, are employed to model the inception of soot precursors and oxidants. With regard to the kinetics of soot formation, our model incorporates a complete set of processes, including the nucleation modelled by the PAH dimerisation, surface growth by the HACA mechanism and PAH condensation, the coagulation of spherical particles and fractal aggregates. The selection of empirical parameters, in coordination with corresponding chemical reaction mechanisms, are adjusted to match the integrated soot volume fraction according to the experimental line-of-sight attenuation (LOSA) profiles. Other experimental signals, involving planar OH laser-induced fluorescence (OH-PLIF) and elastic light scattering (ELS) for soot, are modelled directly, allowing us to circumvent previous physical approximation methods and take account of the polydispersity and morphology of soot.

The comparisons between model predictions and experimental measurements reflect the predictive capability of soot formation in laminar diffusion flames. By combining a single skeleton of soot formation kinetics with three different well-validated gas-phase mechanisms, the flame structure and soot appearance could be captured to a satisfying degree of accuracy. With regard to the localisation of soot in wings and the amount of produced soot, the analysis shows that soot modelling crucially relies on the gas phase chemistry. In particular, it is found that the simulations with the BBP and KM2 mechanisms are able to accurately reproduce the radial distance between the sooty flame wings. However, soot formation on the centreline seems to present a severe challenge: the soot produced here is significantly overestimated by the BBP and KM2 mechanisms and completely absent in the predictions obtained from the ABF mechanism. The sensitivity analysis suggests that soot signals can be tuned by reducing the nucleation rates and adjusting the surface growth rate concomitantly, causing an axial delay in soot proliferation on the centreline.

In order to validate the generality of the soot model, its application has been extended in two studies of laminar diffusion flames with oxygen-containing surrogate blends. Physical processes and empirical parameters utilised in the soot modelling with the BBP chemical kinetics for the ethylene Santoro flames (Chapter 4) remain in the flames with biodiesel fuels.

In the first study for pure compositions of biodiesel fuels: the dibutyl ether (DBE) addition to methyl decanoate (MD). Transport equations of species and energy have been augmented with the effect of molecular weight, thermophrosis and Dufour effect, due to the heavy molecular weight of the biodiesel fuels. Three constituting chemical mechanisms, the MD by Sarathy et al. [212], and the DBE by Cai et al. [213] and the PAH sub-mechanism by Blanquart and Pitsch [61], are reduced, respectively and combined as the MD-DBE-PAH mechanism with 530 species and 3437 reactions. The same model of soot formation which was applied to Santoro flame in Chapter 4 has been justified capable of predicting soot formation in the laminar coflow flame with MD-DBE blended surrogates.

In the spatially heterogeneous combustion issue with fuels of heavy molecular weight, the variation of average molecular weight as well as the thermophoretic effect and Dufour effect serve as additional diffusion terms, which are usually omitted in the transport equations of scalars and energy with simplified convection-diffusion format. Basically, they rarely take effect in the transport equations of species. However, in the energy equation, the effect of average molecular weight

plays an important role around the burner region while thermophoresis and Dufour effect do in the the region of peak temperature, which even counterbalance the original diffusion term. Therefore, these three additional diffusion terms cannot be ignored in the simulations of combustion with fuels of heavy molecular weight.

As a whole, the soot model correctly predicts the temperature and the effect of soot reduction by adding the DBE into the MD. The predicted temperature profiles are basically in line with the experiment in terms of the position and absolute value. For the soot formation, the swallow-tail shape of the soot region and the absolute value of soot production are correctly captured by the simulation. The model predicts 33% decrease of soot production as the DBE addition is from 0 to 40%, in contrast to around 55% reduction measured in the experiment. In the PAH-HACA soot mechanism, the predicted PAH concentration drops by around 50% as the DBE addition is up to 40% while the acetylene concentration barely changes. Given that so far there have been very few attempts to model soot formation in biodiesel flames, especially for the blends with all oxygenated fuels, the results are encouraging for future investigations. Concentrations of PAHs and the species (C_3, C_4) contributing to the formation of aromatic rings are also reduced due to the DBE addition, as the leading cause of soot suppression.

The second study is for practical biodiesel blends: the soot concentration generated from four biodiesels, and their blends with petroleum diesel are modelled in a series of fully pre-vapourised co-flow diffusion flames. Compared with the experiment, the proposed soot model can effectively reproduce the reduction effect on both soot volume fraction and primary particle size by adding biodiesel fuels. Analysis of the discrepancies between numerical and experimental results for diesel and low-blending cases offers an insight for the refinement of soot formation modelling of combustion with large-molecule fuels.

Given that so far there have been very few attempts to model soot formation in biodiesel flames, especially for the blends with all oxygenated fuels, the results are encouraging for future investigations. Therefore, the proposed soot model is able to be universally employed in the co-flow diffusion flames with ethylene and biodiesel fuels.

6.2 Future work

This thesis proposes a novel conservative discretisation method for the population balance equation and implements the coupled CFD-PBE model to laminar diffusion

flames with both fuels of ethylene and biodiesel blends. The future works are expected to list as below.

Turbulent sooting flames

The investigation on turbulent sooting flames is more practical and meaningful since a vast majority of soot emissions origin from combustors with turbulent combustion, such as diesel engines and gas turbines. The coupling of a soot model with turbulent fluid dynamics incurs another level of complexity, as various non-linear interactions between random variables must be accounted for, including the interactions between turbulent and solid-phase soot; turbulence and radiation; turbulence and gas-phase species. Closure models for turbulence-soot interaction are still a challenge although researchers have pioneered to analogise it to the correlation modelling of velocity/velocity (turbulent diffusion closure) and velocity/scalars (micro-mixing closure).

Multidimensional or multi-equation PBE accounting for soot morphology

The PBE model applied in this thesis is one-dimensional and discretised only in the volume space for particles. Therefore, all the geometric or morphological parameters of soot particles are incomplete as they are established on the volume of particles. More than one internal coordinate can be applied in order to consider aggregate structure. Future models should discretise the PBE in multi-property dimension or calculate several transport equations of PBE in terms of various key properties, for the purposes of accurately describing soot aggregates and their structures.

The coordination of gas-phase chemistry and soot kinetics

In this thesis, the moderate-comprehensive model of soot kinetics involves the nucleation by PAH-dimerisation and surface growth by HACA mechanism. However, these models are still relying on proposing empirical parameters and different from the real physics. For example, various active sites are on the edges of the PAH molecules [76] instead of one kind of sites with constant or empirical addition rates. Alternative mechanisms apart from the acetylene addition and PAH dimerisation should be considered, i.e., phenyl addition cyclisation and methyl addition cyclisation mechanisms [22]. In addition, the new findings of long-lived intermediates undermine the steady-state assumption used in HACA mechanism [231, 232]. Another example is the fragmentation and breakage of soot particles at

high temperature, which demonstrates the reversibility of the PAH dimerisation and condensation [233].

It is of more interest to test the robustness of the model by validating it across a range of fuels, pressures and burners. Although adjusting the model parameters is straightforward for its application in different flames, the gas-phase chemical kinetics is still the foundation and bottleneck part for soot formation modellings as many chemical kinetics, specially for complex-molecule fuels which has only been validated in simple reactors rather than real flames.

References

[1] BP PCL. BP statistical review of world energy, 2019.

[2] Department for Environmental Food & Rural Affairs. Defra National Statistics Release: Emissions of air pollutants in the UK, 1970 to 2017, 2017.

[3] World Health Organization. Burden of disease from ambient air pollution 2016, 2016.

[4] F. Correa, M. González, H. Servín, F. Márquez, J. G. Rutiaga, A. A. Lemus, E. Reguera, and V. Alonso. Development of a selective low cost absorbing surface based on soot for solar thermal applications. *Energy Procedia*, 57: 1565–1572, 2014.

[5] H. M. Hulburt and S. Katz. Some problems in particle technology: A statistical mechanical formulation. *Chemical Engineering Science*, 19(8):555–574, 1964.

[6] M. Fairweather, W. P. Jones, H. S. Ledin, and R. P. Lindstedt. Predictions of soot formation in turbulent, non-premixed propane flames. *Symposium (International) on Combustion*, 24(1):1067–1074, 1992.

[7] M. Frenklach and H. Wang. Detailed mechanism and modeling of soot particle formation. In H. Bockhorn, editor, *Soot formation in combustion: mechanisms and models*, pages 165–192. Springer-Verlag, 1994.

[8] F. Liu, H. Guo, G. J. Smallwood, and Ö. L. Gülder. Numerical modelling of soot formation and oxidation in laminar coflow non-smoking and smoking ethylene diffusion flames. *Combustion Theory and Modelling.*, 7:301–315, 2003.

[9] A. Karlsson, I. Magnusson, M. Balthasar, and F. Mauss. Simulation of soot formation under diesel engine conditions using a detailed kinetic soot model. In *SAE*, page 981022, 1998.

[10] A. X. Liu and S. Rigopoulos. A conservative method for solution of the population balance equation, and application to soot formation. *Combustion and Flame*, 205:506–521.

[11] B. E. Wyslouzil and J. Wölk. Overview: Homogeneous nucleation from the vapor phase—the experimental science. *Journal of Chemical Physics*, 145:211702, 2016.

[12] G. Nichols, S. Byard, M. Bloxham, J. Botterill, N. J. Dawson, A. Dennis, V. Diart, N. C. North, and J. D. Sherwood. A review of the terms agglomerate and aggregate with a recommendation for nomenclature used in powder and particle characterization. *Journal of Pharmaceutical Sciences*, 91:2103–2109, 2002.

[13] S. K. Friedlander. *Smoke, Dust and Haze*. Oxford University Press, Oxford, New York, second edition, 2000.

[14] G. Nichols, S. Byard, M. J. Bloxham, J. Botterill, N. J. Dawson, A. Dennis, V. Diart, N. C. North, and J. D. Sherwood. A review of the terms agglomerate and aggregate with a recommendation for nomenclature used in powder and particle characterization. *Journal of Pharmaceutical Science*, 91:2103–2109, 2002.

[15] *Chambers Science and Technology Dictionary*. Chambers Harrap Publishers, New Penderel House, 283-288 High Holborn, London, WC1V 7HZ, UK, 1988, 1988.

[16] *BS 2955:Glossary of Terms Relating to Particle Technology*. British Standards Institution, 389 Chiswick High Road, London, W4 4AL, UK, 1993.

[17] *USP 24: The United States Pharmacopoeia. Monograph 776 (Optical Microscopy)*. States Pharmacopoeia Convention: Rockville, MD., 2000.

[18] A. Van Hook, editor. *Crystallization: Theory and Practice.American Chemical Society Monograph No.152*. Reinhold Publishing Corporation, New York, 1961.

[19] M. Frenklach and H. Wang. Detailed modeling of soot particle nucleation and growth. *Proccedings of the Combustion Institute*, 23:1559–1566, 1991.

[20] M. Celnik, A. Raj, R. West, R. Patterson, and M. Kraft. Aromatic site description of soot particles. *Combustion and Flame*, 91:161–180, 2008.

[21] J. Park, S. Burova, A. S. Rodgers, and M. C. Lin. Experimental and theoretical studies of the C_6H_5 + C_6H_6 reaction. *The Journal of Physical Chemistry A*, 103: 9036–9041, 1999.

[22] K. Ono, Y. Matsukawa, K. Dewa, A. Watanabe, K. Takahashi, Y. Saito, Y. Matsushita, H. Aoki, K. Era, T Aoki, and T. Yamaguchi. Formation mechanisms of soot from high-molecular-weight polycyclic aromatic hydrocarbons. *Combustion and Flame*, 162(6):2670–2678, 2015.

[23] A. Raj, M. Sander, V. Janardhanan, and M. Kraf. A study on the coagulation of polycyclic aromatic hydrocarbon clusters to determine their collision efficiency. *Combustion and Flame*, 157(3):523–534, 2010.

[24] H. Wang. Formation of nascent soot and other condensed-phase materials in flames. *Proceedings of the Combustion Institute*, 33(1):41–67, 2011.

[25] A. A. Lall and M. R. Zachariah. Size resolved soot surface oxidation kinetics. In H. Bockhorn, A.F. Sarofim A. D'Anna, and H. Wang, editors, *Combustion Generated Fine Carbonaceous Particles*, pages 537–568. KIT Scientific Publishing, 2009.

[26] A. A. Hall, M. Seipenbusch, W. Rong, and S.K. Friedlander. On-line measurement of ultrafine aggregate surface area and volume distributions by electrical mobility analysis: II. comparison of measurements and theory. *Journal of Aerosol Science*, 37:9036–9041, 2006.

[27] C. G. Gonzalez. *Characterization of nanoparticles generated in reacting flows*. PhD thesis, Imperial College London, Department of Mechanical Engieering, 2018.

[28] M. R. Kholghy, A. Veshkini, and M. J. Thomson. The core-shell internal nanostructure of soot - a criterion to model soot maturity. *Carbon*, 100:508–536, 2016.

[29] D. P. Chen, S. T. Totton, W. Akroyd, S. Mosbach, and M. Kraft. Size-dependent melting of polycyclic aromatic hydrocarbon nano-clusters: A molecular dynamics study. *Carbon*, 67:79–91, 2014.

[30] M. R. Kholghy, M. Saffaripour, C. Yip, and M. J. Thomson. The evolution of soot morphology in a laminar coflow diffusion flame of a surrogate for jet A-1. *Combustion and Flame*, 160:2119-2130, 2013.

[31] B. S. Haynes and H. G. Wagner. Soot formation. *Progress in Energy and Combustion Science*, 7(4):229–273, 1981.

[32] S. J. Harris and A. M. Weiner. Chemical kinetics of soot particle growth. *Annual Review of Physical Chemistry*, 36:31–52, 1985.

[33] C. J. Dasch. The decay of soot surface growth reactivity and its importance in total soot formation. *Combustion and Flame*, 61(3):219–225, 1985.

[34] I. T. Woods and B. S. Haynes. Soot surface growth at active sites. *Combustion and Flame*, 85(3):523–525, 1991.

[35] R. J. Santoro, H. G. Semerjian, and R. A. Dobbins. Soot particle measurements in diffusion flames. *Combustion and Flame*, 51:203–218, 1983.

[36] M. Y. Choi, G. W. Mulholland, A. Hamins, and T. Kashiwagi. Comparisons of the soot volume fraction using gravimetric and light extinction techniques. *Combustion and Flame*, 102:161-169, 1995.

[37] C. Caumont-Prim, J. Yon, A. Coppalle, F. Ouf, and K. F. Ren. Measurement of aggregates' size distribution by angular light scattering. *Journal of Quantitative Spectroscopy and Radiative Transfer*, 126:140-149, 2013.

[38] C. M. Sorensen. Q-space analysis of scattering by dusts. *Journal of Quantitative Spectroscopy and Radiative Transfer*, 115:93-95, 2013.

[39] Z. Gao, L. Zhu, X. Zou, C. Liu, B. Tian, and Z Huang. Soot reduction effects of dibutyl ether (DBE) addition to a biodiesel surrogate in laminar coflow diffusion flames. *Proceedings of the Combustion Institute*, 37:1265-1272, 2019.

[40] C. R. Shaddix and K. C. Smyth. Laser-induced incandescence measurements of soot production in steady and flickering methane, propane, and ethylene diffusion flames. *Combustion and Flame*, 107:418-452, 1996.

[41] B. Tian, Y. Gao, S. Balusamy, and S. Hochgreb. High spatial resolution laser cavity extinction and laser-induced incandescence in low-soot-producing flames. *Applied Physics B - Lasers and Optics*, 120:469-487, 2015.

[42] S. Einecke, C. Schulz, and V. Sick. Measurement of temperature, fuel concentration and equivalence ratio fields using tracer LIF in IC engine combustion. *Applied Physics B Lasers and Optics*, 71(5):717–723, 2000.

[43] R. K. Hanson, R. M. Spearrin, and C. S. Goldenstein. *Spectroscopy and Optical Diagnostics for Gases*. Springer-Verlag, 2016.

[44] R. L. Vander Wal and A. J. Tomasek. Soot oxidation: dependence upon initial nanostructure. *Combustion and Flame*, 134:1–9, 2003.

[45] W. J. Grieco, J. B. Howard, L. C. Rainey, and J. B. Vander Sander. Fullerenic carbon in combustion-generated soot. *Carbon*, 38(4):597–614, 2000.

[46] M. Schenk, S. Lieb, H. Vieker, A. Beyer, A. G ölzh äuser, H. Wang, and K. Kohse-H öinghaus. Imaging nanocarbon materials: soot particles in flames are not structurally homogeneous. chemphyschem. *ChemPhysChem*, 14:3248–3254, 2013.

[47] R. A. Dobbins, R. A. Fletcher, and W. Lu. Laser microprobe analysis of soot precursor particles and carbonaceous soot. *Combustion and Flame*, 100:301–309, 1995.

[48] B. öktem, M. P. Tolocka, B. Zhao, H. Wang, and M. V. Johnston. Chemical species associated with the early stage of soot growth in a laminar premixed ethylene–oxygen–argon flame. *Combustion and Flame*, 142:364–373, 2005.

[49] B. Zhao, Z. Yang, M. V. Johnston, H. Wang, A. S. Wexler, M. Balthasar, and M. Kraft. Measurement and numerical simulation of soot particle size distribution functions in a laminar premixed ethylene-oxygen-argon flame. *Combustion and Flame*, 133:173–188, 2003.

[50] B. Zhao, Z. Yang, J. Wang, M. V. Johnston, and H. Wang. Analysis of soot nanoparticles in a laminar premixed ethylene flame by scanning mobility particle sizer. *Aerosol Science and Technology*, 37:611–620, 2010.

[51] B. Zhao, Z. Yang, Z. Li, M. V. Johnston, and H. Wang. Particle size distribution function of incipient soot in laminar premixed ethylene flames: effect of flame temperature. *Proceeding of the Combustion Institute*, 30:1441–1448, 2005.

[52] L. A. Sgro, A. De Filippo, G. Lanzuolo, and A. D'Alessio. Characterization of nanoparticles of organic carbon (NOC) produced in rich premixed flames by differential mobility analysis. *Proceeding of the Combustion Institute*, 31:631–638, 2007.

[53] I. M. Kennedy. Models of soot formation and oxidation. *Progress in Energy and Combustion Science*, 23(2), 1997.

[54] S. Rigopoulos. Modelling of soot aerosol dynamics in turbulent flow. *Flow, Turbulence and Combustion*, 103:565–604, 2019.

[55] P. A. Tesner, T. D. Smegiriova, and V. G. Knorre. Kinetics of dispersed carbon formation. *Combustion and Flame*, 17(2):253–260, 1971.

[56] B. F. Magnussen and B. H. Hjertager. On mathematical modeling of turbulent combustion with special emphasis on soot formation and combustion. *Symposium (International) of Combustion*, 16(1):719–729, 1977.

[57] B. F. Magnussen, B. H. Hjertager, J. G. Olsen, and D. Bhaduri. Effects of turbulent structure and local concentrations on soot formation and combustion in C_2H_2 diffusion flames. *Symposium (International) of Combustion*, 17(1):1383–1393, 1979.

[58] J. B. Moss, C. D. Stewart, and K. J. Syed. Flow field modelling of soot formation at elevated pressure. *Symposium (International) of Combustion*, 22(1):413–423, 1989.

[59] I .M. Kennedy, W. Kollmann, and J.-Y Chen. A model for soot formation in a laminar diffusion flame. *Combustion and Flame*, 81(1):73–85, 1990.

[60] J. Appel, H. Bockhorn, and M. Frenklach. Kinetic modeling of soot formation with detailed chemistry and physics: laminar premixed flames of C2 hydrocarbons. *Combustion and Flame*, 121:122–136, 2000.

[61] G. Blanquart and H. Pitsch. A joint volume-surface-hydrogen multi-variate model for soot formation. In H. Bockhorn, A. D'Anna, A. F. Sarofim, and H. Wang, editors, *Combustion Generated Fine Carbonaceous Particles*, pages 437–463. KIT Scientific Publishing, Karlsruhe, 2009.

[62] Y. Wang, A. Raj, and S. H. Chung. Soot modeling of counterflow diffusion flames of ethylene-based binary mixture fuels. *Combustion and Flame*, 162(3): 586–596, 2015.

[63] R. P. Lindstedt and S. A. Louloudi. Joint-scalar transported PDF modeling of soot formation and oxdiation. *Proceeding of the Combustion Institute*, 30:775–783, 2005.

[64] Y. Yunardi, D. Darmadi, H. Hisbullah, and M. Fairweather. Investigation of detailed kinetic scheme performance on modelling of turbulent non-premixed sooting flames. *Journal of Thermal Science*, 20(6):548–555, 2011.

[65] A. Kazakov, H. Wang, and M. Frenklach. Detailed modeling of soot formation in laminar premixed ethylene flames at a pressure of 10 bar. *Combustion and Flame*, 100:111–120, 1995.

[66] S. B. Dworkin, Q. Zhang, M. J. Thomoson, N. A. Slavinskaya, and U. Riedel. Application of an enhanced PAH growth model to soot formation in a laminar coflow ethylene/air diffusion flame. *Combustion and Flame*, 158:1682–1695, 2011.

[67] K. M. Leung, R.P. Lindstedt, and W.P. Jones. A simplified reaction mechanism for soot formation in nonpremixed flames. *Combustion and Flame*, 87:289–305, 1991.

[68] R. P. Lindstedt. Simplified soot nucleation and surface growth steps for non-premixed flames. In H. Bockhorn, editor, *Soot formation in combustion: mechanisms and models*, pages 417–441. Springer-Verlag, 1994.

[69] J. Nagle and R. F. Strickland-Constable. Oxidation of carbon between 1000-2000^{o}C. In *Proceedings of the Fifth Carbon Conference*, volume 1, pages 154–164, 1962.

[70] K. B. Lee, M. W. Thring, and J. M. Beer. On the rate of combustion of soot in a laminar soot flame. *Combustion and Flame*, 6:137–145, 1962.

[71] K. G. Neoh, J. B. Howard, and A. F. Sarofim. Effect of oxidation on the physical structure of soot. *Symposium (International) of Combustion*, 20(1):951–957, 1985.

[72] H. Wang and M. Frenklach. A detailed kinetic modeling study of aromatics formation in laminar premixed acetylene and ethylene flames. *Combustion and Flame*, 110:173–221, 1997.

[73] P. Rodrigues, B. Franzelli, R. Vicquelin, O. Gicquel, and N. Darabiha. Coupling an LES approach and a soot sectional model for the study of sooting turbulent non-premixed flames. *Combustion and Flame*, 190:477–499, 2018.

[74] A. M. El-Leathy, C. H. Kim, G. M. Faeth, and F. Xu. Soot surface reactions in high-temperature laminar diffusion flames. *AIAA Journal*, 42(5):988–996, 2004.

[75] H. Guo, F. Liu, G. J. Smallwood, and Ö. L. Gülder. Numerical study on the influence of hydrogen addition on soot formation in a laminar ethylene–air diffusion flame. *Combustion and Flame*, 145(1):324–338, 2006.

[76] E. K. Y. Yapp, C. G. Wells, J. Akroyd, S. Mosbach, R. Xu, and M. Kraft. Modelling PAH curvature in laminar premixed flames using a detailed population balance model. *Combustion and Flame*, 176:172–180, 2017.

[77] R. L. Drake. A general mathematical survey of the coagulation equation. In G.M. Hidy and J.R. Brock, editors, *Topics in Current Aerosol Research*. Pergamon Press, New York, 1972.

[78] M. Williams and S. Loyalka. *Aerosol Science - Theory and Practice: With Special Applications to the Nuclear Industry*. Pergamon Press, Oxford, 1991.

[79] S. K. Friedlander. *Smoke, Dust and Haze*. Oxford University Press, Oxford, New York, second edition, 2000.

[80] D. Ramkrishna. *Population Balances - Theory and Applications to Particulate Systems in Engineering*. Academic Press, San Diego, 1st edition, 2000.

[81] S. Rigopoulos. Population balance modelling of polydispersed particles in reactive flows. *Progress in Energy and Combustion Science*, 36:412–443, 2010.

[82] M. V. Smoluchowski. Mathematical theory of the kinetics of the coagulation of colloidal solutions. *Zeitschrift für Physikalische Chemie*, 19:129–135, 1917.

[83] Yunardi, R. M. Woolley, and M. Fairweather. Conditional moment closure prediction of soot formation in turbulent, nonpremixed ethylene flames. *Combustion and Flame*, 152(3):360–376, 2008.

[84] H. M. Hulburt and T. Akiyama. Liouville equations for agglomeration and dispersion processes. *Industrial Engineering Chemistry Fundamentals*, 8(2):319–324, 1969.

[85] M. M. R. Williams. Some topics in nuclear aerosol dynamics. *Progress in Nuclear Energy*, 17(1):1–52, 1986.

[86] E. R. Whitby and P. H. McMurry. Modal aerosol dynamics modeling. *Aerosol Science Technology*, 27(6):673–688, 1997.

[87] M. Frenklach. Method of moments with interpolative closure. *Chemical Engineering Science*, 57(12):2229–2239, 2002.

[88] R. McGraw. Description of aerosol dynamics by the quadrature method of moments. *Aerosol Science and Technology*, 27(2):255–265, 1997.

[89] D. L. Marchisio and R. O. Fox. Solution of population balance equations using the direct quadrature method of moments. *Journal of Aerosol Science*, 36(1): 43–73, 2005.

[90] D. L. Wright Jr. Numerical advection of moments of the particle size distribution in Eulerian models. *Journal of Aerosol Science*, 38(3):352–369, 2007.

[91] T. T. Nguyen, F. Laurent, R. O. Fox, and M. Massot. Solution of population balance equations in applications with fine particles: Mathematical modeling and numerical schemes. *Journal of Computational Physics*, 325:129–156, 2016.

[92] M. Balthasar, F. Mauss, M. Pfitzner, and A. Mack. Implementation and validation of a new soot model and application to aeroengine combustors. In *ASME*, 2000.

[93] P. Mitchell and M. Frenklach. Monte carlo simulation of soot aggregation with simultaneous surface growth-why primary particles appear spherical. *Symposium (International) on Combustion*, 27(1):1057–1514, 1998.

[94] J. Singh, M. Balthasar, M. Kraft, and W. Wagner. Stochastic modeling of soot particle size and age distributions in laminar premixed flames. *Proceedings of the Combustion Institute*, 30(1):1457–1465, 2005.

[95] S. Shekar, W. J. Menz, A. J. Smith, M. Kraft, and W. Wagner. On a multivariate population balance model to describe the structure and composition of silica nanoparticles. *Computers & Chemical Engineering*, 43(10):130–147, 2012.

[96] E. Y. K Yee. *Numerical Simulation of Soot in Laminar Flames*. PhD thesis, University of Cambridge, UK, 2016.

[97] M. Balthasar and M. Kraft. A stochastic approach to calculate the particle size distribution function of soot particles in laminar premixed flames. *Combustion and Flame*, 133(3):289–298, 2003.

[98] F. Gelbard and J. H. Seinfeld. Simulation of multicomponent aerosol dynamics. *Journal of Colloid and Interface Science*, 78(2):485–501, 1980.

[99] S. Rigopoulos and A. G. Jones. Finite-element scheme for solution of the dynamic population balance equation. *AIChE Journal*, 49(5):1127–1139, 2003.

[100] S. Qamar, M. P. Elsner, I. A. Angelov, G. Warnecke, and A. Seidel-Morgenstern. A comparative study of high resolution schemes for solving population balances in crystallization. *Computers and Chemical Engineering*, 30(6):1119–1131, 2006.

[101] Y. I. Lim, J. M. Le Lann, X. M. Meyer, and X. Joulia. Dynamic simulation of batch crystallization process by using moving finite difference method. In R. Gani and S. B. Jørgensen, editors, *Eleventh European Symposium on Computer Aided Process Engineering*, volume 9, pages 201–206. Elsevier, 2001.

[102] F. Sewerin and S. Rigopoulos. An explicit adaptive grid approach for the numerical solution of the population balance equation. *Chemical Engineering Science*, 168:250–270, 2017.

[103] F. Sewerin and S. Rigopoulos. An LES-PBE-PDF approach for predicting the soot particle size distribution in turbulent flames. *Combustion and Flame*, 189: 62–76, 2018.

[104] M. D. Smooke, M. B. Long, B. C. Connelly, M. B. Colket, and R. J. Hall. Soot formation in laminar diffusion flames. *Combustion and Flame*, 143(4):613–628, 2005.

[105] J. D. Herdman, B. C. Connelly, M. D. Smooke, M. B. Long, and J. H. Miller. A comparison of raman signatures and laser-induced incandescence with direct numerical simulation of soot growth in non-premixed ethylene/air flames. *Carbon*, 45(15):5298–5311, 2011.

[106] P. Akridis and S. Rigopoulos. Modelling of soot formation in a laminar coflow non-premixed flame with a detailed CFD-population balance model. *Procedia Engineering*, 102:1274–1283, 2015.

[107] P. Akridis and S. Rigopoulos. Modelling of soot formation in laminar diffusion flames using a comprehensive CFD-PBE model with detailed gas-phase chemistry. *Combustion Theory and Modelling*, 21(1):35–48, 2017.

[108] B. Koren. A robust upwind discretization method for advection, diffusion and source terms. In B. Koren C.B. Vreugdenhil, editor, *Numerical Methods for Advection-Diffusion Problems: Notes on Numerical Fluid Mechanics and Multidisciplinary Design*, volume 45, pages 117–138. Vieweg Verlag, 1993.

[109] F. A. Williams. Elementary derivation of the multicomponent diffusion equation. *American Journal of Physics*, 26:467–469, 1958.

[110] A. Kronenburg, R. W. Bilger, and J. H. Kent. Modeling soot formation in turbulent methane–air jet diffusion flames. *Combustion and Flame*, (121):24–40, 2000.

[111] L. Monchick and E. A. Mason. Transport properties of polar gases. *Journal of Chemical physics*, 35:1676–1696, 1961.

[112] C. R. Wilke. A viscosity equation for gas mixtures. *Journal of Chemical Physics*, 18:517–519, 1950.

[113] *Theory Manual: Chemkin-Pro for Reaction Design*. San Diego, 2008.

[114] N. Peters and J. Warnatz, editors. *Numerical methods in laminar flame propogation: A GAMM-Workshop*. Vieweg; Teubner Verlag, Wiesbaden, 1982.

[115] J. G. Parker. Rotational and vibrational relaxation in diatomic gases. *Physics of Fluids*, 2:449–462, 1959.

[116] S. Mathur, P. K. Tondon, and S. C. Saxena. Thermal conductivity of binary, ternary and quaternary mixtures of rare gases. *Molecular Physics*, 12:569–579, 1967.

[117] J. D. Landgrebe and S. E. Pratsinis. A discrete-sectional model for particulate production by gas-phase chemical reaction and aerosol coagulation in the free-molecular regime. *Journal of Colloid and Interface Science*, 139(1):63–86, 1990.

[118] R. Bleck. A fast approximative method for integrating the stochastic coalescence equation. *Journal of Geophysical Research*, 75(27):5165–5171, 1970.

[119] P. Marchal, R. David, J. P. Klein, and J. Villermaux. Crystallization and precipitation engineering - I. An efficient method for solving population balance in crystallization with agglomeration. *Chemical Engineering Science*, 43(1):59–67, 1988.

[120] M. J. Hounslow, R. L. Ryall, and V. R. Marshall. A discretized population balance for nucleation, growth, and aggregation. *AIChE Journal*, 34(11):1821–1832, 1988.

[121] S. Kumar and D. Ramkrishna. On the solution of population balance equations by discretization - I. A fixed pivot technique. *Chemical Engineering Science*, 51 (8):1311–1332, 1996.

[122] S. Kumar and D. Ramkrishna. On the solution of population balance equations by discretization - II. A moving pivot technique. *Chemical Engineering Science*, 51(8):1333–1342, 1996.

[123] F. Laurent, A. Sibra, and F. Doisneau. Two-size moment multi-fluid model: A robust and high-fidelity description of polydisperse moderately dense evaporating sprays. *Communications in Computational Physics*, 20(4):902–943, 2016.

[124] S. Yang and M. E. Mueller. A multi-moment sectional method (MMSM) for tracking the soot number density function. *Proceedings of the Combustion Institute*, 2018.

[125] C. J. Pope and J. B. Howard. Simultaneous particle and molecule modeling (SPAMM): An approach for combining sectional aerosol equations and elementary gas-phase reactions. *Aerosol Science and Technology*, 27(1):73–94, 1997.

[126] H. Richter, S. Granata, W. H. Green, and J. B. Howard. Detailed modeling of PAH and soot formation in a laminar premixed benzene/oxygen/argon low-pressure flame. *Proceedings of the Combustion Institute*, 30(1):1397–1405, 2005.

[127] F. Gelbard and J. H. Seinfeld. Numerical solution of the dynamic equation for particulate systems. *Journal of Computational Physics*, 28(3):357–375, 1978.

[128] F. Gelbard, Y. Tambour, and J. H. Seinfeld. Sectional representations for simulating aerosol dynamics. *Journal of Colloid and Interface Science*, 76(2): 541–556, 1980.

[129] M. B. Colket and R. J. Hall. Successes and uncertainties in modelling soot formation in laminar, premixed flames. In H. Bockhorn, editor, *Soot Formation in Combustion, Springer Series in Chemical Physics 59*, pages 442–470. Springer-Verlag, 1994.

[130] R. J. Hall, M. D. Smooke, and M.B. Colket. Predictions of soot dynamics in opposed jet diffusion flames. In R. F. Sawyer, editor, *Physical and Chemical Aspects of Combustion: A Tribute to Irvin Glassman*, pages 189–230. Overseas Publishers Association, Netherland, 1997.

[131] M. Nicmanis and M. J. Hounslow. Finite-element methods for steady-state population balance equations. *AIChE Journal*, 44(10):2258–2272, 1998.

[132] A. I. Roussos, A. H. Alexopoulos, and C. Kiparissides. Part III: Dynamic evolution of the particle size distribution in batch and continuous particulate processes: A Galerkin on finite elements approach. *Chemical Engineering Science*, 60(24):6998–7010, 2005.

[133] K. Netzell, H. Lehtiniemi, and F. Mauss. Calculating the soot particle size distribution function in turbulent diffusion flames using a sectional method. *Proceedings of the Combustion Institute*, 31(1):667–674, 2007.

[134] P. Rodrigues, B. Franzelli, R. Vicquelin, O. Gicquel, and N. Darabiha. Unsteady dynamics of PAH and soot particles in laminar counterflow diffusion flames. *Proceedings of the Combustion Institute*, 36(1):927–934, 2017.

[135] D. Aubagnac-Karkar, A. El Bakali, and P. Desgroux. Soot particles inception and PAH condensation modelling applied in a soot model utilizing a sectional method. *Combustion and Flame*, 189:190–206, 2018.

[136] D. Aubagnac-Karkar, J.-B. Michel, O. Colin, P. E. Vervisch-Kljakic, and N. Darabiha. Sectional soot model coupled to tabulated chemistry for diesel RANS simulations. *Combustion and Flame*, 162(8):3081–3099, 2015.

[137] F. Filbet and P. Laurençot. Numerical simulation of the smoluchowski coagulation equation. *SIAM Journal on Scientific Computing*, 25(6):2004–2028, 2004.

[138] S. Qamar and G. Warnecke. Solving population balance equations for two-component aggregation by a finite volume scheme. *Chemical Engineering Science*, 62(3):679–693, 2007.

[139] Z. A. Melazak. The effect of coalescence in certain collision process. *Quarterly of Applied Mathematics*, 11:231–234, 1953.

[140] W. T. Scott. Analytical studies of cloud droplet coalescence I. *Journal of the Atomspheric Sciences*, 25:613–628, 1968.

[141] T. E. Ramabhadran, T. W. Peterson, and J. H. Seinfeld. Dynamics of aerosol coagulation and condensation. *AIChE journal*, 22(5):840–851, 1976.

[142] R. Bandyopadhyaya, R. Kumar, K. S. Gandhi, and D. Ramkrishna. Modeling of precipitation in reverse micellar systems. *Langmuir*, 13:3610–3620, 1997.

[143] J. S. Bhatt and R. P. Lindstedt. Analysis of the impact of agglomeration and surface chemistry models on soot formation and oxidation. *Proceedings of the Combustion Institute*, 32(1):713–720, 2009.

[144] S. K. Friedlander and C. S. Wang. The self-preserving particle size distribution for coagulation by brownian motion. *Journal of Colloid and Interface Science*, 22 (2):126–132, 1966.

[145] J. D. Landgrebe and S. E. Pratsinis. Gas-phase manufacture of particulates: Interplay of chemical reaction and aerosol coagulation in the free-molecular regime. *Industrial & Engineering Chemistry Research*, 28:1474–1481, 1989.

[146] S. Vemury, K. A. Kusters, and S. E. Pratsinis. Time-lag for attainment of the self-preserving particle size distribution by coagulation. *Journal of Colloid and Interface science*, 165:53–59, 1994.

[147] S. Vemury and S. E. Pratsinis. Self-preserving size distributions of agglomerates. *Journal of Aerosol Science*, 26(2):175–185, 1995.

[148] M.U. Bäbler and M. Morbidelli. Analysis of the aggregation–fragmentation population balance equation with application to coagulation. *Journal of Colloid and Interface Science*, 316:428–441, 2007.

[149] P.G. Saffman and J.S. Turner. On the collision of drops in turbulent clouds. *Journal of Fluid mechanics*, 1:16–30, 1956.

[150] M.H. Waldner, J. Sefcik, M. Soos, and M. Morbidelli. Initial growth kinetics and structure of colloidal aggregates in turbulent coagulator. *Power Technology*, 156(2):226–234, 2005.

[151] I. Nopen, T. Koegst, K. Mahieu, and P. A. Vanrolleghem. PBM and activated sludge flocculation: From experimental data to a calibrated model. *AIChE Journal*, 51:1548–1557, 2005.

[152] P. Sandkühler, J. Sefcik, and M. Morbidelli. Kinetics of aggregation and gel formation in concentrated polystyrene colloids. *Journal of Physical Chemistry*, 108:20105–20121, 2004.

[153] J.D. Pandya and L.A. Spielman. Floc breakage in agitated suspensions: theory and data processing strategy. *Journal of Colloid and Interface Science*, 90(2): 517–531, 1982.

[154] M. Kostoglou and A. J. Karabelas. On the self-similarity of the aggregation–fragmentation equilibrium particle size distribution. *Journal of Aerosol Science*, 30:157–162, 1999.

[155] R. J. Santoro, T. T. Yeh, J. J. Horvath, and H. G. Semerjian. The transport and growth of soot particles in laminar diffusion flames. *Combustion Science and Technology*, 53:89–115, 1987.

[156] R. Kosfeld. The physics of polymers, concepts for understanding their structures and behavior. *International Journal Review of Physical Chemistry and Chemical Physics*, 206(1):274–276, 1998.

[157] S. Suzuki, K. Kuwana, and R. Dobashi. Effect of particle morphology on thermophoretic velocity of aggregated soot particles. *International Journal of Heat and Mass Transfer*, 52(21):4695–4700, 2009.

[158] L. Waldmann. *Rarefield Gas Dynamics*. Academic Press, New York, 1961.

[159] J. R. Brock. On the theory of thermal forces acting on aerosol particles. *Journal of Colloid Science*, 17(8):768–780, 1962.

[160] M. K. Akbar and S. M. Ghiaasiaan. Radiation heat transfer and soot thermophoresis in laminar turbe flow. *Numerical. Heat Transfer, Part A: Application*, 47(7):635–670, 2005.

[161] A. Toda, Y. Ohi, R. Dobashi, T. Hirano, and T. Sakuraya. Accurate measurement of thermophoretic effect in microgravity. *Journal of Chemical Physics.*, 105(16): 7083–7087, 1996.

[162] S. B. Pope. PDF methods for turbulent reactive flows. *Progress in Energy and Combustion Science*, 11(2):119–192, 1985.

[163] S. V. Patankar. *Numerical Heat Transfer and Fluid Flow*. Hemisphere Publishing Corporation, New York, 1980.

[164] W. P. Jones, F. di Mare, and A. J. Marquis. *LES-BOFFIN: User's Guide*. Imperial College London, Department of Mechanical Engineering, London, July 2002.

[165] E. Hairer, S. P. Nørsett, and G. Wanner. *Solving Ordinary Differential Equations I: Nonstiff Problems*. Springer-Verlag, Berlin, Heidelberg, 1993.

[166] R. A. Dobbins and C. M. Megaridis. Morphology of flame-generated soot as determined by thermophoretic sampling. *Langmuir*, 3(2):254–259, 1987.

[167] B. C. Connelly, B. A. V. Bennett, M. D. Smooke, and M. B. Long. A paradigm shift in the interaction of experiments and computations in combustion research. *Proceeding of the Combustion Institute*, 32(1):879–886, 2009.

[168] B. Duarte and C. Baptista. Moving finite elements method applied to dynamic population balance equations. *AIChE Journal*, 54(3):673–692, 2008.

[169] F. Sewerin and S. Rigopoulos. An LES-PBE-PDF approach for modelling particle formation in turbulent reacting flows. *Physics of Fluids*, 29(10):105105, 2017.

[170] J. M. Seitzman and R. K. Hanson. Comparison of excitation techniques for quantitative fluorescence imaging of reacting flows. *AIAA Journal*, 31(3):513–519, 1993.

[171] Y. Wang, A. Raj, and S. H. Chung. A PAH growth mechanism and synergistic effect on PAH formation in counterflow diffusion flames. *Combustion and Flame*, 160:1667–1676, 2013.

[172] G. Blanquart, P. Pepiot-Desjardins, and H. Pitsch. Chemical mechanism for high temperature combustion of engine relevant fuels with emphasis on soot precursors. *Combustion and Flame*, 156(3):588–607, 2009.

[173] B. Eiteneer and M. Frenklach. Experimental and modeling study of shock-tube oxidation of acetylene. *International Journal of Chemical Kinetics*, 35(9):391–414, 2003.

[174] S. M. Lee, S. S. Yoon, and S. H. Chung. Synergistic effect on soot formation in counterflow diffusion flames of ethylene–propane mixtures with benzene addition. *Combustion and Flame*, 136(4):493–500, 2004.

[175] http://www.sandia.gov/tnf/radiation.html, 2003.

[176] J. Y. Hwang and S. H. Chung. Growth of soot particles in counterflow diffusion flames of ethylene. *Combustion and Flame*, 125(1):752–762, 2001.

[177] A. Veshkini, S. B. Dworkin, and M. J. Thomson. A soot particle surface reactivity model applied to a wide range of laminar ethylene/air flames. *Combustion and Flame*, 161(12):3191–3200, 2014.

[178] S. E. Pratsinis. Simultaneous nucleation, condensation, and coagulation in aerosol reactors. *Journal of Colloid and Interface Science*, 124(2):416–427, 1988.

[179] K. Tian, K. A. Thomson, F. Liu, and D. R. Snelling. Determination of the morphology of soot aggregates using the relative optical density method for the analysis of TEM images. *Combustion and Flame*, 144(4):782–791, 2006.

[180] H. Bladh, J. Johnsson, and P. E. Bengtsson. Influence of spatial laser energy distribution on evaluated soot particle sizes using two-colour laser-induced incandescence in a flat premixed ethylene/air flame. *Applied Physics B - Lasers and Optics*, 96(4):645–656, 2009.

[181] O. Link, D. R. Snelling, K. A. Thomson, and G. J. Smallwood. Development of absolute intensity multi-angle light scattering for the determination of polydisperse soot aggregate properties. *Proceeding of the Combustion Institute*, 33(1):847–854, 2011.

[182] Ü. Ö. Köylü, Y. C. Xing, and D. E. Rosner. Fractal morphology analysis of combustion-generated aggregates using angular light scattering and electron microscope images. *Langmuir*, 11(12):4848–4854, 1995.

[183] A. M. Brasil, T. L. Farias, and M. G. Carvalho. A recipe for image characterization of fractal-like aggregates. *Journal of Aerosol Science*, 30(10):1379–1389, 1999.

[184] O. Leszczyszyn. https://www.materials-talks.com/blog/2012/11/15/size-matters-rh-versus-rg/. 2012.

[185] S. Einecke, C. Schulz, and V. Sick. Measurement of temperature, fuel concentration and equivalence ratio fields using tracer lif in ic engine combustion. *Appl. Phys. B-Lasers O*, 71(5):717–723, 2000.

[186] M. Tamura, P. A. Berg, J. E. Harrington, J. Luque, J. B. Jeffries, and G. P. Smith. Collisional quenching of ch(a), oh(a), and no(a) in low pressure hydrocarbon flames. *Combustion and Flame*, 114(3):502–514, 1998.

[187] https://www.sri.com/engage/products-solutions/lifbase, 2016.

[188] W. H. Dalzell and A. F. Sarofim. Optical constants of soot and their application to heat-flux calculations. *Journal of Heat Transfer*, 91(1):100–104, 1969.

[189] J. A. Koziriski and R. Saade. Effect of biomass burning on the formation of soot particles and heavy hydrocarbons: An experimental study. *Fuel*, 77(4): 225–237, 1998.

[190] B. Damstedt, J. M. Pederson, D. Hansen, T. Knighton, J. Jones, C. Christensen, L. Baxter, and D. Tree. Biomass cofiring impacts on flame structure and emissions. *Proceedings of the Combustion Institute*, 31(2):2813–2820, 2007.

[191] M. M. Roy and K. W. Corscadden. An experimental study of combustion and emissions of biomass briquettes in a domestic wood stove. *Applied Energy*, 99: 206–212, 2012.

[192] O. Herbinet, W. J. Pitz, and C. K. Westbrook. Detailed chemical kinetic oxidation mechanism for a biodiesel surrogate. *Combustion and Flame*, 154(3): 507–528, 2008.

[193] M. Lapuerta, O. Armas, and J. Rodríguez-Fernández. Effect of biodiesel fuels on diesel engine emissions. *Progress in Energy and Combustion Science*, 34(2): 198–223, 2008.

[194] W. Merchan, S. G. Sanmiguel, and S. McCollam. Analysis of soot particles derived from biodiesels and diesel fuel air-flames. *Fuel*, 102:525–535, 2012.

[195] W. Jing, Z. Wu, W. Zhang, and T. Fang. Measurement of soot temperature and KL factor for spray combustion of biomass derived renewable fuels. *Energy*, 91:758–771, 2015.

[196] J. Kasumba and B. A. Holmén. Nonpolar organic compound emission rates for light-duty diesel engine soybean and waste vegetable oil biodiesel fuel combustion. 102:9783–9792, 2016.

[197] J. Brakora, Y. Ra, R. D. Reita, J. Mcfarlane, and C. S. Daw. Development and validation of a reduced reaction mechanism for biodiesel fueled engine simulations. In *SAE*, pages 675–702, 2008.

[198] J. Yu, Y. Ju, and X. Gou. Surrogate fuel formulation for oxygenerated and hydrocarbon fuels by using the molecular structures and functional groups. *Fuel*, 166:211–218, 2016.

[199] A. Li, L. Zhu, Y. Mao, J. Zhai, D. Han, X. Lu, and Z. Huang. Surrogate formulation methodology for biodiesel based on chemical deconstruction in consideration of molecular structure and engine combustion factors. *Combustion and Flame*, 199:152–167, 2019.

[200] X. Jiang, K. Zhou, M. Xiao, K. Sun, and Wang Y. Stochastic simulation of soot formation evolution in counterflow diffusion flames. *Journal of Nanotechnology*, page 9479582, 2018.

[201] N. A. Slavinskaya and P. Frank. A modelling study of aromatic soot precursors formation in laminar methane and ethene flames. *Combustion and Flame*, 156 (9):1705–1722, 2009.

[202] R. M. Woolley, M. Fairweather, and Yunardi. Conditional moment closure modelling of soot formation in turbulent, non-premixed methane and propane flames. 88(3):393–407, 2009.

[203] J. P. Soussi, R. Demarco, J. L. Consalvi, F. Liu, and A. Fuentes. Influence of soot aging on soot production for laminar propane diffusion flames. *Fuel*, 210: 472–481, 2017.

[204] Z. Wen, S. Yun, M. J. Thomson, and M. F. Lightstone. Modeling soot formation in turbulent kerosene/air jet diffusion flames. *Combustion and Flame*, 135(3): 323–340, 2003.

[205] M. Bolla, D. Farrace, Y. M. Wright, and K. Boulouchos. Modelling of soot formation in a heavy-duty diesel engine with conditional moment closure. *Fuel*, 117:309–325, 2014.

[206] Z. Wang, L. Li, J. Wang, and R. D. Reitz. Effect of biodiesel saturation on soot formation in diesel engine. *Fuel*, 175:240–248, 2016.

[207] Z. Petranović, T. Besenić, M. Vujanović, and N. Duić. Modelling pollutant emissions in diesel engines, influence of biofuel on pollutant formation. *Journal of Environment Management*, 203:1038–1046, 2017.

[208] F. Liu, X. He, X. Ma, Q. Zhang, M. J. Thomson, H. Guo, G. J. Smallwood, S. Shuai, and J. Wang. An experimental and numerical study of the effects of dimethyl ether addition to fuel on polycyclic aromatic hydrocarbon and soot formation in laminar coflow ethylene/air diffusion flames. *Combustion and Flame*, 158:547–563, 2011.

[209] H. Jin, A. Cuoci, A. Frassoldati, T. Faravelli, Y. Wang, Y. Li, and F. Qi. Experimental and kinetic modeling study of PAH formation in methane coflow diffusion flames doped with n-butanol. *Combustion and Flame*, 161:657–670, 2014.

[210] A. Khosousi, F. Liu, S. B. Dworkin, N. A. Eaves, M. J. Thomson, X. He, Y. Dai, Y. Gao, F. Liu, S. Shuai, and J. Wang. Experimental and numerical study of soot formation in laminar coflow diffusion flames of gasoline/ethanol blends. *Combustion and Flame*, 162(10):3925–3933, 2015.

[211] Liu A. X. Tian, B., C.T. Chong, L. Fan, S. Ni, J-H. Ng, S. Rigopoulos, K. H. Luo, and S. Hochgre. Experimental and numerical study on soot formation in laminar diffusion flamesof biodiesels and methyl esters. *submitted to Proceedings of the Combustion Institute*, 2019.

[212] S.M. Sarathy, M.J. Thomson, W.J. Pitz, and et al. An experimental and kinetic modeling study of methyl decanoate combustion. *Proceeding of the Combustion Institute*, 33:399–405, 2011.

[213] L. Cai, A. Sudholt, D. J. Lee, and et al. Chemical kinetic study of a novel lignocellulosic biofuel: Di-n-butyl ether oxidation in a laminar flow reactor and flames. *Combustion and Flame*, 161:798–809, 2014.

[214] O. Herbinet, W. J. Pitz, and C. K. Westbrook. Detailed chemical kinetic mechanism for the oxidation of biodiesel fuels blend surrogate. *Combustion and Flame*, 157:893–908, 2010.

[215] S. Thion, C. Togbé, Z. Serinyel, G. Dayma, and P. Dagaut. A chemical kinetic study of the oxidation of dibutyl-ether in a jet-stirred reactor. *Combustion and Flame*, 185:4–15, 2017.

[216] B. Tian, Y. Gao, S. Balusamy, and S. Hochgreb. High Spatial Resolution Laser Cavity Extinction and Laser Induced Incandescence in Low Soot Producing Flames. *Applied Physics B*, 120(3):469–487, 2015. doi: 10.1007/s00340-015-6156-3.

[217] B. Tian, C.T. Chong, L. Fan, J.-H. Ng, C. Zhang, and S. Hochgreb. Soot volume fraction measurements over laminar pool flames of biofuels, diesel and blends. *Proceedings of the Combustion Institute*, 37(1):877–884, 2018. ISSN 15407489. doi: 10.1016/j.proci.2018.05.094.

[218] E. Ranzi, A. Frassoldati, R. Grana, A. Cuoci, T. Faravelli, A. P. Kelley, and C. K. Law. Hierarchical and comparative kinetic modeling of laminar flame speeds of hydrocarbon and oxygenated fuels. *Progress in Energy and Combustion Science*, 38(4):468–501, 2012. ISSN 03601285. doi: 10.1016/j.pecs.2012.03.004. URL http://dx.doi.org/10.1016/j.pecs.2012.03.004.

[219] S. K. Hoekman, A. Broch, C. Robbins, E. Ceniceros, and M. Natarajan. Review of biodiesel composition, properties, and specifications. *Renewable and Sustainable Energy Reviews*, 16(1):143 – 169, 2012. ISSN 1364-0321. doi: https://doi.org/10.1016/j.rser.2011.07.143. URL http://www.sciencedirect.com/science/article/pii/S136403211100390X.

[220] W. Merchan-Merchan, A. Abdihamzehkolaei, and D. A. Merchan-Breuer. Formation and evolution of carbon particles in coflow diffusion air flames of vaporized biodiesel, diesel and biodiesel-diesel blends. *Fuel*, 226:263–277, 2018.

[221] P. K. Sahoo, L. M. Das, M. K.G. Babu, P. Arora, V. P. Singh, N. R. Kumar, and T. S. Varyani. Comparative evaluation of performance and emission characteristics of jatropha, karanja and polanga based biodiesel as fuel in a tractor engine. *Fuel*, 88(9):1698–1707, 2009.

[222] M. Chhabra, A. Sharma, and G. Dwivedi. Performance evaluation of diesel engine using rice bran biodiesel. *Egyptian Journal of Petroleum*, 26(2):511–518, 2017.

[223] A. Probudha Hasan, A. Wakil, and A. Kafy. Prospect of rice bran for biodiesel production in Bangladesh. *Procedia Engineering*, 90:746–752, 2014.

[224] NIST. Chemistry webbook, srd 69, dodecanoic acid, methyl ester. https://webbook.nist.gov/cgi/cbook.cgi?ID=111-82-0, 2018. Accessed: 2019-03-10.

[225] NIST. Chemistry webbook, srd 69, methyl tetradecanoate n.d. https://webbook.nist.gov/cgi/cbook.cgi?ID=C124107&Mask=4, 2018. Accessed: 2019-03-10.

[226] A. Frassoldati, A. Cuoci, A. Stagni, T. Faravelli, and E. Ranzi. Skeletal kinetic mechanism for diesel combustion. *Combustion Theory and Modelling*, 21(1): 79–92, 2017. ISSN 17413559. doi: 10.1080/13647830.2016.1222082. URL https://doi.org/10.1080/13647830.2016.1222082.

[227] Y. Ra and R. D. Reitz. A combustion model for IC engine combustion simulations with multi-component fuels. *Combustion and Flame*, 158(1):69–90, 2011. ISSN 00102180. doi: 10.1016/j.combustflame.2010.07.019. URL http://dx.doi.org/10.1016/j.combustflame.2010.07.019.

[228] A. Li, L. Zhu, Y. Mao, J. Zhai, D. Han, X. Lu, and Z. Huang. Surrogate formulation methodology for biodiesel based on chemical deconstruction in consideration of molecular structure and engine combustion factors. *Combustion and Flame*, 199:152–167, 2019. ISSN 15562921. doi: 10.1016/j.combustflame.2018.10.026. URL https://doi.org/10.1016/j.combustflame.2018.10.026.

[229] M. R. Kholghy, J. Weingarten, A. D. Sediako, J. Barba, M. Lapuerta, and M. J. Thomson. Structural effects of biodiesel on soot formation in a laminar coflow diffusion flame. *Proceedings of the Combustion Institute*, 36(1):1321–1328, 2017. ISSN 15407489. doi: 10.1016/j.proci.2016.06.119. URL http://dx.doi.org/10.1016/j.proci.2016.06.119.

[230] A. X. Liu, C. E. Garcia, F. Sewerin, and et al. Population balance modelling and laser diagnostic validation of soot particleevolution in laminar ethylene diffusion flames. *Combust. Flame*, 2019submitted.

[231] R. Whitesides, A. C. Kollias, D. Domin, W. A Lester Jr., and M. Frenklach. Graphene layer growth: collision of migrating five-member rings. *Proceeding of the Combustion Institute*, 31:539–546, 2008.

[232] R. Whitesides, D. Domin, R. Salomón-Ferrer, Jr. W. A. Lester, and M. Frenklach. Graphene layer growth chemistry: five- and six-member ring flip reaction. *Journal of physical chemistry: A*, 112:2125–2130, 2008.

[233] N. A. Eaves, S. B. Dworkin, and M. J. Thomson. The importance of reversibility in modeling soot nucleation and condensation processes. *Proceeding of the Combustion Institute*, 35(2):1787–1794, 2015.